Z^0 boson measurement in the dimuon channel in PbPb collisions with the CMS experiment

By

JORGE A. ROBLES
M.S (University of California at Davis)

DISSERTATION

Submitted in partial satisfaction of the requirements for the degree of

DOCTOR OF PHILOSOPHY

in

Physics

in the

OFFICE OF GRADUATE STUDIES

of the

UNIVERSITY OF CALIFORNIA

DAVIS

Approved:

Prof. Manuel Calderón de la Barca Sánchez

Prof. Daniel Cebra

Prof. Ramona Vogt

2011

A mis padres, a mis hermanos y a mi familia.

Y a mi incansable compañera, Edith.

Acknowledgments

I am extremely grateful Manuel Calderón for the guidance, support and patience during these years, *especially* for the interest and time dedicated to explain and question almost every aspect of what I presented to him. I appreciate the the 'relaxed' attitude to enjoy life while keeping a hard working mentality when it came to research. I am thankful to Daniel Cebra, for the encouragement and advice given. Also, for the many discussions that fed my scientific curiosity.

I want to thank Catherine, Camelia and Raphael for the time and work shared during my stay at CERN, I learned a lot from you guys. I would also like to extend my gratitude for everybody who helped towards the completion of this work. This includes the rest of my physics class with whom I shared many stressful times but also enjoyed many good celebrations.

I want to specially thank my parents, Jorge & Maria, for their everlasting love and support. They have taught me, by example, that good things derive from hard work. *Grácias pa, Grácias ma.*

Last, but certainly not least, my most sincere thanks to the person that pushed me to keep going during hard times, that moved with me half-way around the world, and has been there for me day-in and day-out, my wife Edith.

Contents

List of Figures

List of Tables

Abstract

The unprecedented center of mass energy available at the LHC offers unique opportunities for studying the properties of the strongly-interacting QCD matter created in $PbPb$ collisions. This QCD matter is created at extreme temperatures, intermediate momentum fractions and large Q^2 values. With its high precision, large acceptance for tracking, and a trigger scheme that allows analysis of each minimum-bias $PbPb$ events, CMS is especially suited to measure high-p_T dimuons, even in the high multiplicity environment of heavy-ion collisions. Electroweak probes are accessible for the first time in heavy-ion collisions. The Z^0 boson is cleanly reconstructed in the dimuon channel with the CMS detector. Precise measurements of Z^0 production in heavy-ion collisions can help to constrain the nuclear parton distribution functions (PDF) as well as serve as a standard candle of the initial state in $PbPb$ collisions at the LHC energies. From the $PbPb$ run at $\sqrt{s_{NN}} = 2.76$ TeV, the inclusive and differential measurements of the Z^0 boson yield in the muon decay channel are presented. Making use of the pp reference run at the same center-of-mass energy, the nuclear modification factor, R_{AA}, is calculated. The value of the $R_{AA} = 1.03 \pm 25(stat)[+4.0, -5.0](syst)$ is found to be consistent with the expectation that no modification is observed with respect to next-to-leading order pQCD calculations, scaled by the number of incoherent nucleon-nucleon collisions

Chapter 1

Introduction

Heavy-ion collisions are the most promising way to study the quark-gluon plasma (QGP). Some of the most important measurements in heavy-ion collisions document the modifications of probes that traverse the QGP relative to their vacuum counterparts. From the modifications suffered by these probes, qualities of the QGP can be inferred. The hot-dense-colored plasma created in heavy-ion collisions is not present in *pp* collisions. Thus, a comparison of the observables in these two systems, using *pp* as a baseline, provides with information about the QGP. From the relative modifications observed qualitative and quantitative statements about the hot medium can be made. Such effects can be the observed 'jet-quenching' in central heavy-ion collisions or quarkonium dissociation in heavy-ion collisions. These measurements are done using a statistical approach. A sample of events in heavy-ion collisions is compared to an equivalent sample of events in *pp* collisions. From the statistical differences a physical observable is deduced. A better approach would be to study the effects in the same event as a 'control' probe is observed. In order to study the effects of the hot-dense-colored medium created in heavy-ion collisions, the control probe would need to be insensitive to it. Before the start of the heavy-ion program at the Large Hadron Collider (LHC), direct photons played that role. Photons traverse the medium unaffected by the QGP. However, it is very challenging to extract a clean direct photon signal from a high-multiplicity environment. A γ-tagged jet approach is also promising, but must faces some of the same issues as the direct photons.

With the large increase in center-of-mass in energy with respect to that of the Relativistic Heavy Ion Collider (RHIC), the LHC can provide enough energy to reach the electroweak scale in heavy-ion collisions. With this, a new set of probes are at hand. The Z^0 emerges as the obvious candidate to act as a control probe. Since the Z^0 is an electroweak gauge boson, it does not interact with the QGP. The Compact Muon Solenoid (CMS), is an experiment designed to reconstruct high-p_T probes is especially suited for muons, making the $Z^0 \rightarrow \mu^+\mu^-$ decay channel an easy choice to be used as a control probe. It is expected that neither the Z^0 boson, nor its decay muons, interact with the hot medium. However, cold nuclear matter (CNM) effects are expected to account for small deviations. It is the purpose of this thesis to measure the yields of the $Z^0 \rightarrow \mu^+\mu^-$ channel in $PbPb$ collisions at $\sqrt{s_{NN}} = 2.76$ TeV and compare them to the yields obtained from a pp reference sample at the same center-of mass energy.

The outline of this thesis is as follows. Chapter two describes the theoretical background relevant to this thesis topic. A brief overview of the Standard Model, signatures of the QGP and electroweak probes in heavy-ion collisions are discussed. Chapter three briefly describes the the LHC apparatus and outlines the relevant geometry of the CMS detector. Specific sub-detectors, relevant to this measurement, are described. In chapter four, a description of the simulation and a Monte Carlo (MC) sample used is given. A description of the heavy-ion reconstruction algorithms is included. An overview of the MC matching and data-driven methods to calculate efficiencies is also included. Chapter five describes the details of the heavy-ion setup adopted by CMS and the selections (online and offline) used to select the data sample used for this analysis. Chapter six includes the results from the $PbPb$ run as well as the pp from the reference run. The final systematic uncertainties are discussed, along with the measured yields, and compared to the relevant theoretical models. Using the pp reference run, the nuclear modification factor, R_{AA} was calculated. The result is compared to the available models.

Chapter 2

Theory Overview

2.1 Standard model

The current understanding of the forces that describe the interactions of particles and fields is known as the Standard Model (SM). The strong, weak and electromagnetic interactions are understood as arising due to the exchange of various spin-one bosons amongst the spin-half particles that make up the matter. In other words, the SM is composed of particles that arise from excitations of the different fields and force carriers that mediate the interaction between particles. Gravity is not yet included in this model. Efforts are geared towards achieving a Theory of Everything (ToE) that would include all known forces at the moment. Figure 2.1 shows a schematic of the elementary particles described within the standard model. Elementary particles can be identified by a set of quantum numbers such as mass, charge, color, flavor. Spin is an intrinsic property that adds an extra degree of freedom to the set of quantum numbers that define a particle. Spin-1/2 particles are known as fermions. In the SM, these fermions can be either leptons or quarks. Leptons and quarks come in three generations. A total of six different quarks are currently known. The six different species are known as 'flavors'. These are: up (u), down (d), charm (c), strange (s), top (t) and bottom (b). Their antiparticles also exist. The leptons are: electron (e), muon (μ), tau (τ) as well as the electron neutrino (ν_e), muon neutrino (ν_μ) and tau neutrino (ν_τ), all these with the antiparticle counterpart. The spin-1 particles that compose the SM are force mediators. The photon (γ) mediates the electromagnetic force; the $W^{\pm}$ and Z^0

bosons mediate the weak force; while the gluon (g) mediates the strong force. Not listed, but predicted and sought after, is the Higgs boson (H^0) which would complete the picture of the SM. Interactions with the Higgs field generates the particle masses. The standard model is one of the most significant achievements of the physics community. Since 1978 it has met every experimental test.

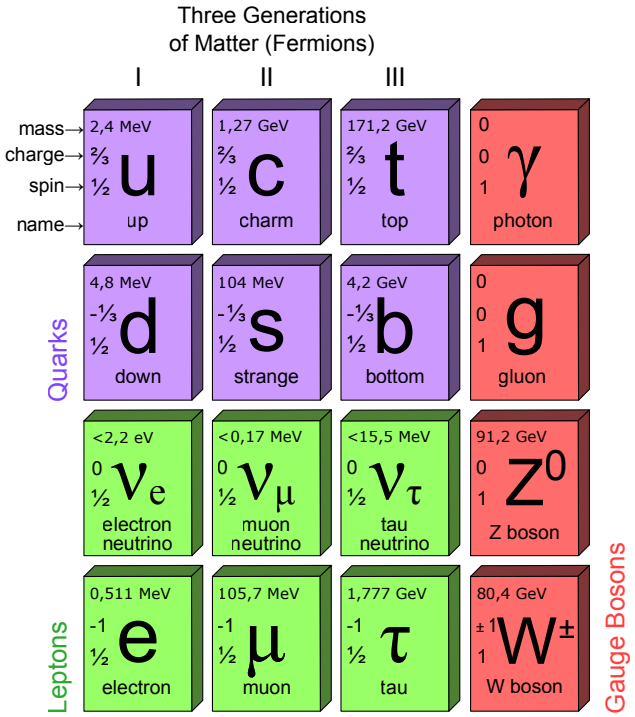

Figure 2.1: Elementary particles of the standard model [1, 2].

2.2 Electroweak theory

The description of electromagnetism as a quantum field theory is known as Quantum Electrodynamics (QED). QED describes how light and matter interact. It describes all phenomena involving interactions of the electrically-charged particles by photon exchange. The strength of the electromagnetic interactions is given by the fine structure constant, $\alpha = e^2/4\pi\epsilon_0\hbar c$. The main characteristic of this interaction is that the force decreases as $1/r^2$, where r is the distance between charged particles.

The weak interaction is the 'weakest' force described in the SM. It is mediated by the exchange of massive $W^{\pm}$ and Z^0 bosons, the large masses of these gauge bosons accounts for the short range of the interaction. This force is responsible for the beta decay of subatomic particles, through $n \rightarrow p + e^- + \bar{\nu}^e$. Its unique property is that it induces flavor changing currents through $W^{\pm}$ exchange. This allows quarks to swap their *flavors*. The weak interaction is the only one that violates parity symmetry and charge-parity symmetry. Parity symmetry refers to the property of particles to remain the same after a sign flip in the spatial dimensions.

The idea of a unified description of the electromagnetic and weak forces was first suggested by Glashow in 1961. The first evidence supporting the existence of these processes came in 1973 from the Gargamelle [6] bubble chamber experiment at CERN, culminating with the discovery of the $W^{\pm}$ and Z^0 bosons in 1983 [7, 8] at the Super Proton-Antiproton Synchrotron (S$p\bar{p}$S). These massive bosons are described by a SU(2) gauge theory. However, they should be massless under a gauge theory, as is the case of the photon which is described by a U(1) gauge theory.

The unification of the weak and electromagnetic force under $\mathrm{SU}(2)_L \otimes \mathrm{U}(1)_Y$ gauge group, where Y denotes the hypercharge. In general, the SU(2) denotes a group of unitary 2×2 matrices with determinant 1. In general a SU(n) group has n^2 -1 free parameters with n^2 -1 generators. The SU(2) symmetry is connected to the conservation of weak-isospin charge (analogous to isospin but applies to quarks, leptons and electroweak bosons instead of hadrons). There are 3 spin-one bosons associated with this group, and one with a factor $U(1)_Y$. The four bosons associated with $\mathrm{SU}(2)_L \otimes \mathrm{U}(1)_Y$ are related to the $W^{\pm}$ and Z^0 (after spontaneous symmetry breaking), and the photon from QED. The $\mathrm{U}(1)_Y$ is the group of unitary 1-dimensional matrices. It stands for the space-time dependent rotations in the complex plane so that the multiplication of the wave-function of a particle by a member of this group produces a phase change. The invariance under phase changes leads to the conservation of weak hypercharge Y. Y is the generator of the U(1) group.

In the 90's, experiments at the LEP and SLC colliders based their programs around the exploration of the Z^0 boson. Precision studies were carried out at the 0.1% level of the Z^0 mass, M_Z, its line-shape and its branching ratios [9]. The second phase of the LEP

program moved towards exploration of the $W^{\pm}$ bosons. Given the the energy regime and the performance of the accelerator, the LEP apparatus was able to deliver thousands of Z^0 events to each of the four experiments, which earned it the name: "Z factory" [10]. The center-of-mass milestone reached with the available technology at the time opened the door towards precision measurements of electroweak processes.

The production of electroweak probes in hadron colliders comes mainly from $q\bar{q} \rightarrow Z^0$ and $q\bar{q}' \rightarrow$ W at leading order (LO). While at next-to-leading order (NLO), the Z^0 boson is produced via $q\bar{q} \rightarrow Z^0 g$ and $q(\bar{q})g \rightarrow Z^0 q(\bar{q})$. These processes are sensitive to the quarks and antiquark distribution functions (PDF) in the colliding hadrons. Studies of the PDFs were pursued at the Tevatron, and currently carried out at the LHC.

2.3 Quantum chromodynamics

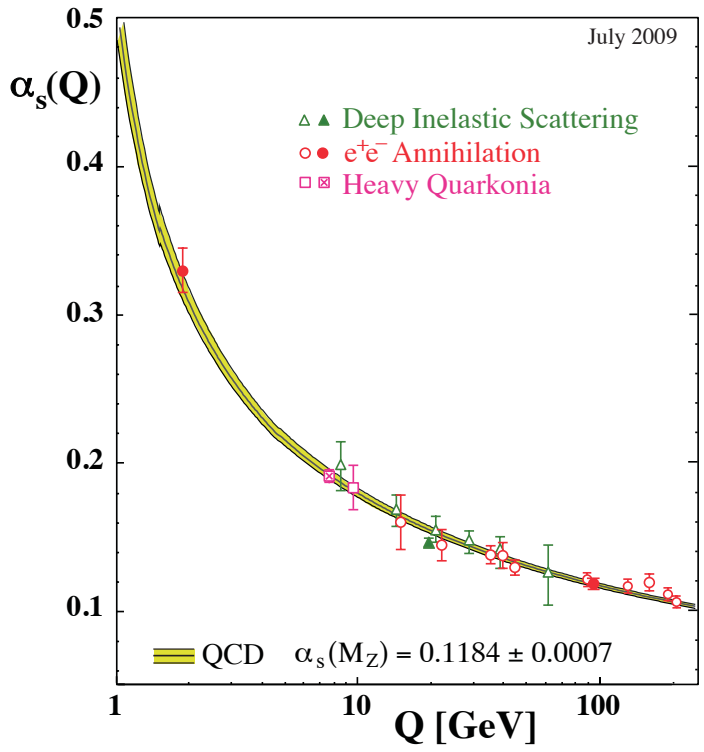

Figure 2.2: Measurements of the QCD coupling constant as a function of energy.

The theory of Quantum Chromodynamics (QCD) was first formulated in 1972-73

by Murray Gell-Mann [11] and Steven Weinberg. It is described by an SU(3) gauge theory, more specifically a non-Abelian gauge theory. A unique feature of non-Abelian theories is the correlation between the strength of interaction and distance scales. In QCD these characteristics lead to confinement and asymptotic freedom. Confinement of color charges is due to the fact that the force between quarks increases as the distance between them gets larger. This suggests that it would take an infinite amount of energy to isolate a single quark, keeping the quarks bound 'inside' hadrons. At short range the color force decreases. This allows the quarks and gluons to behave as if they were essentially free, inside a hadron. In order to probe distances $\sim$ 1 fm or less, a very-high momentum particle is required. At asymptotically high energies the quarks can be probed as if they were free. The prediction of such behavior in 1970 resulted in a Nobel Prize for Politzer, Wilczek and Gross [12]. The strong interaction is regulated by a scale-dependent constant, α_s, shown at LO in Eq. 2.1 [13]. Where Λ is the minimum scale, n_f is the number of flavors, and Q^2 is the absolute value of the momentum transfer in a 2-2 process. Figure 2.2 shows the behavior of α_s as a function of momentum transfer. The coupling decreases at high scales, but diverges as $Q^2 \rightarrow \Lambda$. Extractions of α_s from deep inelastic scattering (DIS) experiments, e^+e^- collisions, and heavy quarkonia decays in a wide range of scales are shown. The value of α_s at the Z^0 pole, $\alpha_s(m_Z)$ is found to be 0.1184 $\pm$0.0007 [2].

$$\alpha_s(Q^2) = \frac{12\pi}{(33 - 2n_f)\ln(\frac{Q^2}{\Lambda^2})} \tag{2.1}$$

The strong force is mediated by the internal degree of freedom known as *color*. Colored gluons are the mediator bosons that act between quarks. In a quark-antiquark interaction, a particle with three possible types of color charges interacts with another one with three possible color charges. There can be in principle nine types of gluons belonging to a color singlet state in the U(1) group and a color octate state in a SU(3) group. The color singlet state does not carry a color charge and is therefore colorless. A colorless, massless gluon would lead to a long range interaction between color singlet hadrons. Since this interaction is not observed in nature, the color singlet gluon state is forbidden. There are, thus, only eight gluons, members of the color octet, all of which carry color charges. In

contrast to QED, where there are no interaction vertices with only photons (photon-photon interactions) in QCD gluons can interact with other gluons as well as quarks. Thus there exist 3 and 4 gluon vertices. The observation of three-jet events in e^+e^- collisions [14] provided the first experimental observation of the gluon.

QCD describes the interactions of matter at the subatomic scale and describes the physics of the strong interaction. Quarks and gluons make up hadrons, which are color-singlet states. Deep Inelastic Scattering is one direct way to obtain evidence of the existence of quarks. A high energy electron can probe deep inside the proton. The scattering pattern from the collisions suggests a point-like structure within the nucleus, thus suggesting an interaction with an elementary particle. The top quark, the last piece of the SM to be found, was discovered at Fermilab in 1995 by the CDF and D0 collaborations [15, 16].

2.4 Physics of the QGP

QCD is the only sector of the SM whose full *collective* behavior is accessible to study in the laboratory. At high densities, in the non-perturbative region of QCD, strongly-interacting matter in thermal equilibrium at a finite temperature is created [17]. Heavy-ion collisions are expected to produce hot and dense medium, consisting of deconfined quarks and gluons, known as the quark-gluon plasma (QGP). The study of the many-body dynamics of high-density QCD covers a vast range of fundamental physics problems, described below [18]:

- Deconfinement and chiral symmetry restoration: Lattice QCD calculations [18] predict a new form of matter at energy densities well above the critical density, $\epsilon_c \approx 1$ GeV/fm^3 consisting of an extended volume of deconfined and massless quarks and gluons, the QGP [19]. The exploration of this phase of matter (equation of state, order of the phase transition, transport properties) promises to shed light on basic aspects of the strong interaction.

- Early universe cosmology: The quark-hadron phase transition took place some 10 μs after the Big Bang, and is believed to be the most important event between the elec-

troweak transition and Big Bang nucleosynthesis. Several cosmological implications follow, such as formation of strangelets, cold dark matter or baryon fluctuations. For a review see Ref. [20] .

- Proton structure and evolution at small-x: At high energies, hadrons consist of a very dense system of gluons with small (Bjorken) momentum fraction $x = p_{\text{parton}}/p_{\text{hadron}}$. At low x, the probability to emit an extra gluon is large, and gg fusion processes play an increasing role. At $x < 10^{-2}$ hadrons are more appropriately described in the context of the Color Glass Condensate (CGC) [18, 21].

- Gauge-string duality: Theoretical applications of the Anti-de Sitter/Conformal-Field-Theory (AdS/CFT) duality provide results in strongly coupled gauge theories [18, 22]. Applications of this formalism for QCD-like theories have led to the determination of transport properties, such as QGP viscosity [23], the 'jet quenching' parameter $\langle \hat{q} \rangle$ [24], or the heavy quark diffusion coefficient [25].

- Compact object astrophysics: At high baryon densities, the attractive force between quarks can lead to the formation of Cooper pairs. Cold dense matter is expected to behave as a color superconductor [26]. This may be realized in the core of neutron stars and be open to astronomical observation.

2.4.1 Experimental probes of hot QCD matter

The only experimental way to reproduce a hot and dense colored medium is via collisions of heavy-ions at ultra-relativistic energies. Information about the properties of the strongly-interacting medium created in heavy-ion collision is commonly inferred from comparison to a baseline system. The baseline can be established with measurements in pp or pA collisions. The comparison of pA with pp collisions allows to identify cold nuclear matter effects; while the comparison to AA with pp collisions can shed light on hot QCD processes. The observation is presented in the form of ratios. The suppression or enhancement of yields and/or spectra are linked to properties of the medium. For the QGP to be formed in ultra-relativistic heavy-ion collisions, the initial temperatures and energy densities must be larger than the critical temperature ($T_c \approx 170$ MeV) [27] and the critical

density ϵ_c. An estimation of the formation time of the plasma, τ_0, by Bjorken is found to be 1 fm/c [28]. Various estimates place the particle production time at about the same range $\tau_{\rm pro}$ = 0.4-1.2 fm/c [13]. There are several signatures of the QGP that look different from a simple superposition of hadronic interactions and can reveal some of its high density or high temeperature properties.

2.4.2 Signatures of the quark-gluon plasma

After a QGP has been formed a subsequent cooling phase allows to reconstitute itself as hadrons. Particles that arise from the interactions between constituents of the plasma will provide information about the state of the QGP. There is no single unequivocal way to identify the creation of a QGP state. It is the combination of data from measurements of different observables that may indicate the presence of a deconfined state.

Dilepton production

In the QGP, a quark can interact with an antiquark to form a virtual photon that will decay into a di-lepton. Leptons interact with the particles in the interaction region only via the electromagnetic force, not via the strong force. Therefore, the production rate and momentum distributions of the produced l^+l^- pairs carry information of the thermodynamical state of the medium at the moment of their production [13]. Their invariant mass spectra thus provides information about the temperature of the system. For these measurements, the dynamical evolution of the system, radial flow and others sources of di-lepton background must be properly taken into account. The dominant non-QGP production of di-leptons comes from the Drell-Yan ($q\bar{q} \rightarrow \gamma \rightarrow l^-l^+$) process. In the region below and invariant mass of 1 GeV/c^2, the decay from ρ, ω and ϕ dominate the production of l^+l^-pairs arising from a possible formation of the QGP [29]. The di-electron mass spectra from the CERES collaboration at the CERN SPS [30], show an invariant mass spectra from Pb+Au collisions that does not match the 'hadronic cocktail' used to describe p+Be data. This is confirmed in the di-muon channel in In+In collisions in the same mass range by the NA60 collaboration [31] and more recently by the PHENIX collaboration [32]. A similar excess below the mass of the ρ is observed. Some modifications to the low mass vector boson are

expected from the QGP formation, but a full quantitative understanding is still out of our grasp at the moment.

Quarkonium suppression

One of the most striking signatures of the presence of a state of deconfinement and at high temperatures, is the suppression of the quarkonium states [33]. The force tying together the $Q\overline{Q}$ pair, is screened by the quarks and gluons around them. The suppression is predicted to occur above a critical temperature, T_c, With a pattern dependent on the binding energy of the quarkonium state. The Υ(1S) is the most strongly bound quarkonium state and is expected to melt last. Some models associate dissociation of states with temperatures ranges with respect to T_c. The melting of the upsilon states is taken as an indicative of temperatures in the range of 1-3 T_c. Similarly, the melting of charmonium states indicate temperatures in the range of 1-1.2 T_c [34]. Other mechanisms that affect the measured yields may be at play. These include cold nuclear matter effects that can reduce the production without the presence of a QGP [35, 36] or recombination mechanisms that enhance the production via statistical recombination [37, 38, 39], mainly for the J/ψ.

Jet quenching

The study of jets in heavy-ion collisions is of great interest given that jets are showers of hadrons and initialized by quark and gluons, thus, carrying information about the QGP. The definition of a jet is algorithm-dependent, but can be loosely defined as a an attempt to recover the kinematics of scattered partons. The general approach is to attempt to group together particles that are close in phase-space around a 'leading particle'. Ideally, jets are a collection of hadrons, therefore sensitive the the strongly interacting field. It has been found that jets in the opposite side in azimuth (ϕ), to that of a leading hadron, show a different a pattern in AuAu collisions than in dAu and *pp* collisions [40]. In the most central events, the jet in the away side disappears. The observed absorption of jets as a function of the geometry of the collision suggests the possibility of the use of *jet tomography* as a tool to investigate the densities within the plasma. This can be done with a 'control' probe in place, such as the photon or the Z^0. Where the Z^0 or photon can be used to infer

the original p_T of a jet that will be go through the medium.

Flow

In the hydrodynamic expansion following a heavy-ion collision, the matter develops a correlated emission pattern known as *flow*. This is a collective phenomenon already observed at low energies. The flow pattern is related to the equation of state of the system through the dependence of the pressure on temperature and energy density [41]. The experimental observations show correlated particle emission, that develops an anisotropic pattern in the azimuthal direction. Given the periodic nature of the correlation, a Fourier expansion is used decompose the observation into modes. The second mode, v_2, is closely related to the amount of energy that flows out-of-plane with respect to the collision geometry. The v_2 coefficient, also known as elliptic flow, reflects the initial spatial anisotropy, which can directly be translated into observed momentum distribution of identified particles [42]. Since spatial anisotropy is largest at early in the QGP stage, elliptic flow is sensitive to the early stages of the evolution [43].

2.5 Heavy-ion collisions at the LHC

The study of $PbPb$ collisions at the LHC opens a previously inaccessible regime for heavy-ion physics. The factor of 14 increase in center-of-mass energy, compared to previous ion collisions, accesses a new set of probes for study of the hot, dense medium at unprecedented values of energy density. The capabilities of the CMS detector allow for very clean measurements even in the busy environment of heavy-ion collisions. The production rates for hard probes are high enough to carry out high statistics measurement of high-Q^2 processes. Hard probes include jets, high-p_T hadrons, heavy quarks, quarkonia and weak bosons. These are of crucial importance because they originate from initial hard scattering and are directly coupled to the fundamental QCD degrees of freedom. Their production timescale is short, $\tau \approx 1/p_T \leq 0.1$ fm/c allowing them to propagate through and potentially be affected by the medium. Also, their cross sections can be theoretically predicted using the perturbative QCD (pQCD) framework [44]. In light of this, hard probes can provide precise

tomographic information about the hottest and densest phase of the reaction. Perturbative probes that do not couple to the colored partons, such as direct photons, di-leptons, Z^0 and $W^{\pm}$ bosons, are not affected by final-state interactions. They can provide direct information about the parton distribution functions of the colliding ions. Furthermore, these weakly interacting probes can be used as undistorted references when produced with a recoil jets. Fig 2.3 [3] shows the $PbPb$ cross sections for hard processes as a function of the center-of-mass energy of the colliding system. The $PbPb$ cross-section, σ_{PbPb}, is obtained by scaling the cross section of a given process at NLO in pp collisions by a factor of A^2 to account for the scaling of the nuclear geometry. This is knows as 'binary collision scaling', and it assumes that each possible nucleon-nucleon collisions can contribute equally to the production cross section, i.e. the $PbPb$ yields are given by an incoherent superposition of the total number of possible nucleon-nucleon collisions. It can be observed that Υ, Z^0, $W^{\pm}$ and jet production rates are small (Υ) or out in AA collisions at RHIC energies.

2.5.1 High transverse momenta

Particles emitted with high transverse momenta (p_T) are believed to come from hard scattering processes. The yield of high-p_T particles is expected to scale with the number of binary collisions, $N_{\rm coll}$. Medium effects can modify this scaling. These deviations are quantified by the nuclear modification factor, R_{AA}. The R_{AA} is calculated as a ratio of the yield obtained in $PbPb$ collisions normalized by the yield measured in pp collisions. In the soft part of the spectra, $p_T \leq$ 2-3 GeV/c an enhancement is seen. This is due to the fact that in this regime particle yields scale with the number of participants, $N_{\rm part}$. Measurements comparing the nuclear modification factor for direct photons with π^0 and η show opposite effects: a suppression of the π^0 and η as a function of p_T, while the R_{AA} of the direct photons is found to be 1 at $p_T \geq$ 2 GeV/c [45, 46]. The high-p_T photons play the role of a "control" probe, since they traverse the medium unmodified. Photons do not interact with the colored medium. Given the high multiplicity nature of heavy-ion collisions the measurement of direct photons poses a great challenge. The large background for this type of measurement comes from: the decay of π^0's and other mesons. It requires careful identification and rejection of photons from other sources in order to extract a proper

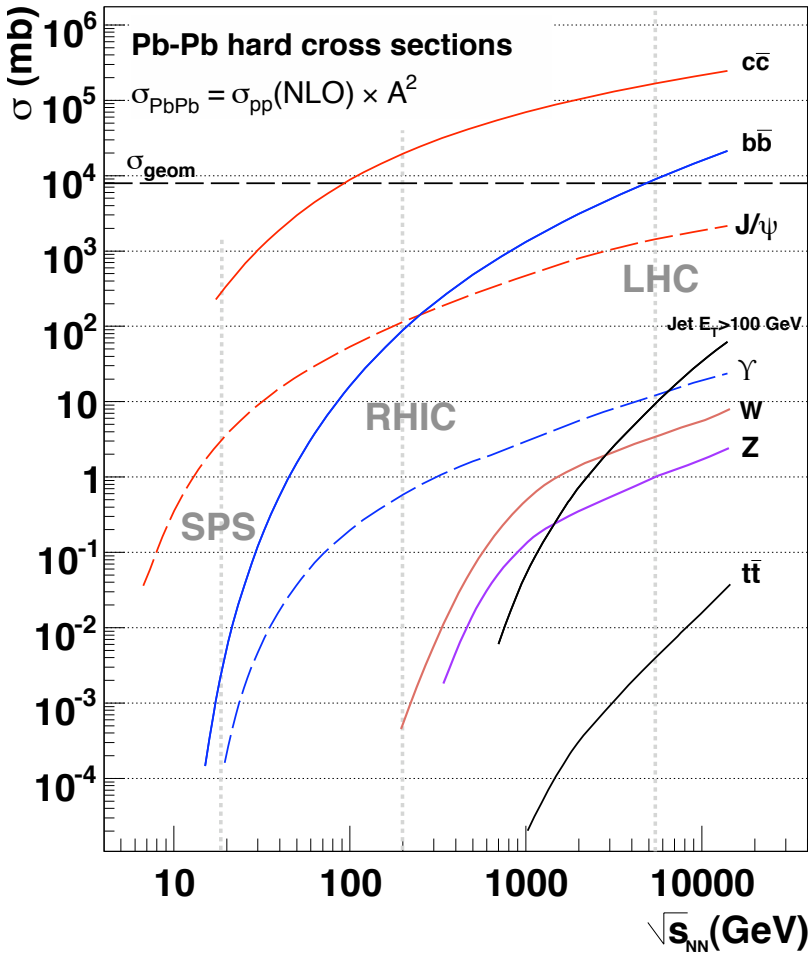

Figure 2.3: Hard cross sections in $PbPb$ collisions as a function of $\sqrt{s_{NN}}$ for high-Q^2 processes [3].

nuclear modification factor. A better approach would be to use a non-interacting probe that can be cleanly identified. This is the case of the Z^0 in the dimuon channel, as we discuss in the next section.

2.6 Electroweak probes of heavy-ion collisions

At the LHC, the center-of mass energy allows access to electroweak probes (EWK) for the first time in heavy-ion collisions. The Z^0 and $W^{\pm}$ are massive gauge bosons that can traverse the hot QCD medium unaffected. The $W^{\pm}$ and Z^0 decay quickly after the collision.

Reconstruction of these particles can be carried out in their lepton (plus missing transverse energy) and di-lepton channels respectively. The decay lepton also traverses the plasma unaffected by the strong interactions. The CMS detector is especially suited for analyses of high-p_T muon channels. Given that a pair of high-p_T muons can be efficiently and cleanly reconstructed, we consider using the $Z^0 \rightarrow \mu^+\mu^-$ channel as a benchmark for hot matter effects. In order to employ the Z^0 as a benchmark probe, a few effects need to be taken into account. The energy loss suffered by the muons have been estimated in Ref. [47] to have 2% effect. Due to multiple scattering of the muons with electrically-charged particles in the hot medium. Cold nuclear matter effects can also affect the yields. At the LHC, the x region, ~ 0.02, probed is sensitive to isospin effects that arise from the change of quark composition of the colliding systems. Different quark compositions that make up Pb ions, (protons and neutrons) compared to only protons, give way to the sampling of different PDFs. The isospin effects are estimated to be on the order of 3% [48]. The phenomenon that is expected to have the largest effect is the modification of the PDFs in nuclei as a function of x, known as shadowing [49]. This effect is expected to modify the expected cross sections by 10-20% [48]. It is important to first understand cold nuclear effects such as shadowing before studying other medium effects by comparing leptonic and hadronic decay channels [49]. The branching ratio to hadronic decays is $\approx$ 70%, while the total leptonic decay is estimated to be $\approx$10%.

A perhaps more powerful approach can be taken by studying a Z^0-tagged jets, produced by $q\bar{q} \rightarrow Z^0 g$ and $qg \rightarrow Z^0 q$, subsequently decaying to a di-lepton and a jet. Thus providing with an *in-situ* probe to quantify the energy loss suffered by the jets. However, Ref. [50] indicates that NLO effects on Z^0-tagged jets can cause a 25% p_T smearing that will have an effect on 'jet-balancing'.

By making use of a beautifully designed detector, optimized for detection of high-p_T muons (among other things) it is possible to measure processes, such as $Z^0 \rightarrow \mu^+\mu^-$, that can act as a 'baseline' to study heavy-ion collsions. The $Z^0 \rightarrow \mu^+\mu^-$ channel can be used to quantify hot nuclear effects when compared to the $Z^0 \rightarrow q\bar{q}$ decays. Since the only difference between (modulo the branching ratios) the measured yields would come from interaction of the quarks with the medium. The Z^0 can also be use as an '*in-situ*' probe to

quantify effects that an 'opposite-side' jet might suffer. Both of these measurements rely on the assumption that the Z^0 does not interact with the medium. Thus we must confirm that the $Z^0 \rightarrow \mu^+\mu^-$ decay is unmodified. The dimuon channel in CMS allows for very clean Z^0 extraction that aids the measurement. By corroborating the expectations that prescribe no interaction between the QGP and an electroweak probe reconstructed in the dimuon channel, we can establish $Z^0 \rightarrow \mu^+\mu^-$ as a 'standard candle' in heavy-ion collisions.

Chapter 3

The LHC and the CMS Detector

3.1 LHC

3.1.1 LHC layout

The Large Hadron Collider (LHC) is a particle accelerator complex at the European Center for Nuclear Research (CERN). The accelerator has a 26 659 meter circumference that crosses the French-Swiss border at four different points and is, on average, 100 meters underground. The 3.8 m diameter accelerator tunnel was the once occupied by the Large Electron-Positron Collider (LEP). The LHC is made out of two coupled synchrotrons designed to collide opposing beams. The accelerator complex is made up of 9300 magnets. The two counter-rotating beams cross at four different points. A detector is built around each of the points. The experiments, shown in Fig 3.1, built around the interaction points are: A Toroidal Large LHC AparatuS (ATLAS, at point-1), A Large Ion Collider Experiment (ALICE, at point-2), the Compact Muon Solenoid (CMS, at point-5) and the LHC Beauty experiment (LHCb, at point-8).

LHC parameters

The nominal center-of-mass energy of the LHC in proton-proton collisions is $\sqrt{s} =$ 14 TeV. For other nuclear species, the center of mass energy scales with Z/A, where Z and A are the nuclear proton and mass numbers, respectively. In the case of $PbPb$ collisions,

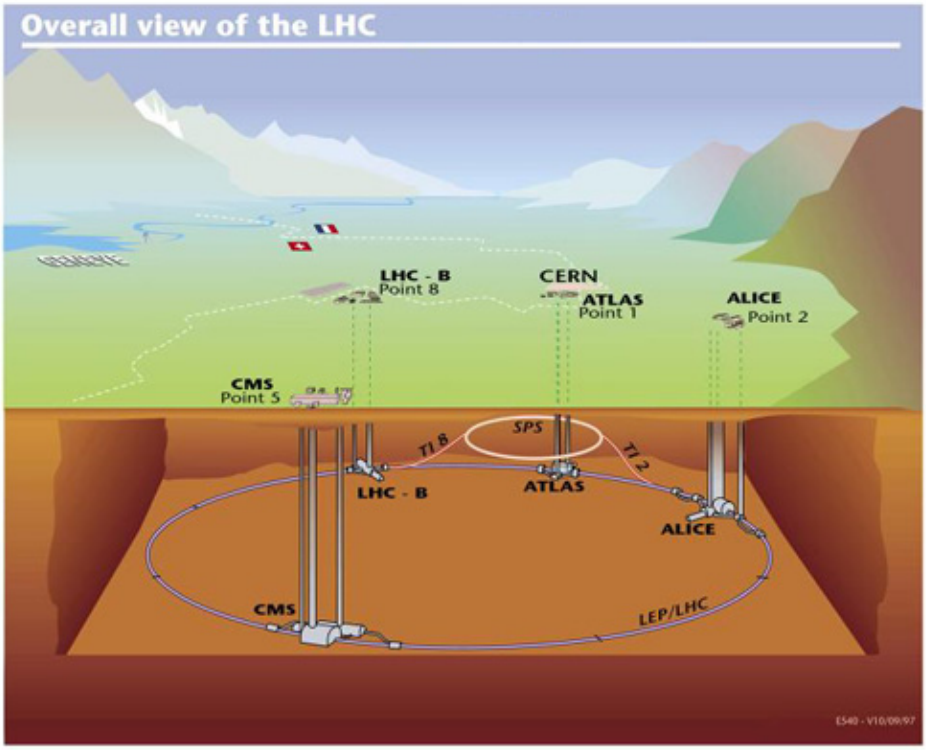

Figure 3.1: LHC layout.

we use $^{208}_{82}$Pb, which can therefore be collided at a maximum energy of $\sqrt{s_{NN}} = 5.5$ TeV. The event rate generated in the LHC is given by Eq. 3.1:

$$dN/dt = L\sigma_{\text{process}} \tag{3.1}$$

where σ_{process} is the cross section for the process under the study and L the machine luminosity. The luminosity depends only on the beam parameters and is,

$$L = \frac{N_b^2 n_b f_{\text{rev}} \gamma_r}{4\pi\epsilon_n \beta^*} F \tag{3.2}$$

for a Gaussian beam distribution N_b is the number of particles per bunch, n_b the number of bunches per beam, f_{rev} is the revolution frequency, γ_r the relativistic gamma factor, ϵ_n the normalized transverse beam emittance, β^* the beta-star function at the collision point (β is a beam optics quantity determined by the accelerator magnet, the $*$ indicates that it is measured at the interaction point), and F the geometric luminosity reduction factor due

to the crossing angle at the interaction point (IP):

$$F = \left(1 + \left(\frac{\theta_c \sigma_z}{2\sigma*}\right)^2\right)^{-1/2} \tag{3.3}$$

Now, θ_c is the full crossing angle at the IP, σ_z the RMS bunch length, and σ^* the transverse RMS beam size at the IP. The above expression assumes beams with circular profiles in the plane transverse to the beam direction, with $\sigma_z \ll \beta$, and with equal beam parameters for both beams.

The LHC was designed to collide protons, instead of proton and antiprotons. Proton collisions require that the two counter-rotating beams make use of opposite magnetic dipole fields in each ring. The two beams share an approximately 130 m long common beam pipe along the Interaction Regions (IRs). There is not enough room for two separate rings of magnets in the LHC tunnel. Therefore, the LHC uses twin bore magnets that consist of two sets of coils and beam channels within the same mechanical structure and cryostat.

The maximum particle density per bunch is limited by the non-linear beam-beam interactions that each particle experiences when the beam bunches collide with each other. The beam-beam interaction is measured by the linear tune shift,

$$\xi = \frac{N_b r_p}{4\pi\epsilon_n} \tag{3.4}$$

where r_p is the classical proton radius, $r_p = e^2/(4\pi\epsilon_0 m_p c^2)$. Experience with existing hadron colliders indicates that the total linear tune shift summed over all IPs should not exceed 0.015 [51]. With three proton experiments requiring head-on collisions, this implies that the linear beam-beam tune shift for each IP should satisfy $\xi < 0.005$ [51].

The luminosity lifetime in the LHC is not constant over a physics run. It decays due to degradation of intensities and emittances of the circular beams. The main cause of beam loss is from collision. The initial decay time of bunch intensity due to this effect is:

$$\tau_{\text{nuclear}} = \frac{N_{\text{tot},0}}{L\sigma_{\text{tot}}, k} \tag{3.5}$$

where $N_{\text{tot},0}$ is the initial beam intensity, L the initial luminosity, σ_{tot} the total cross section and k the number of IPs. Assuming an initial peak luminosity of $L = 10^{-34}\text{cm}^{-2}\text{s}^{-1}$ and

two high luminosity experiments, the above expression yields an initial decay time of $\tau = 44.85$ h. Equation 3.5 results in the decay of the beam intensity and luminosity as functions of time:

$$N_{tot}(t) = \frac{N_{tot,0}}{1 + t/\tau_{\text{nuclear}}} \tag{3.6}$$

$$L(t) = \frac{L_0}{(1 + t/\tau_{\text{nuclear}})^2} \tag{3.7}$$

The time required to reach $1/e$ of the initial luminosity is given by:

$$t_{1/e} = (\sqrt{e} - 1)\tau \tag{3.8}$$

a luminosity decay time of $\tau_{\text{nuclear},1/\text{e}} = 29$ h. Other contributions come from Toucheck scattering and from particle losses due to a slow emittance blow-up [51].

The integrated luminosity over one run is,

$$L_{\text{int}} = L_0 \tau_L \left[1 - e^{-T_{\text{run}}/\tau_L}\right] \tag{3.9}$$

where T_{run} (14.9 h) is the total length of the luminosity run.

3.1.2 LHC design

The LHC complex is itself made up of subsystems that work to ionize, store, transfer and ramp up the energy of the beams. The LHC is therefore designed as a proton-proton collider with separate magnet elds and vacuum chambers in the main arcs and with common sections only at the insertion regions where the experimental detectors are located. The LHC is supplied with protons from the injector chain: Linac2 - Proton Synchrotron Booster (PSB) - Super Proton Synchrotron(SPS), as shown in Fig. 3.2. The main challenges for the PS complex are (i) the unprecedented transverse beam brightness (intensity/emittance), almost twice that previously produced by the PS and (ii) the production of a bunch train with the LHC spacing of 25 ns before extraction from the PS. The Linac2 generates 50 MeV protons, which are fed to the PSB. These protons get accelerated to 1.4 GeV and sent into the PS where they get ramped up to 26 GeV. After that, the SPS takes them to an energy

of 450 GeV, the energy at which they are injected in the LHC. In the main ring the bunches are accumulated, and accelerated to reach the peak energy for collisions.

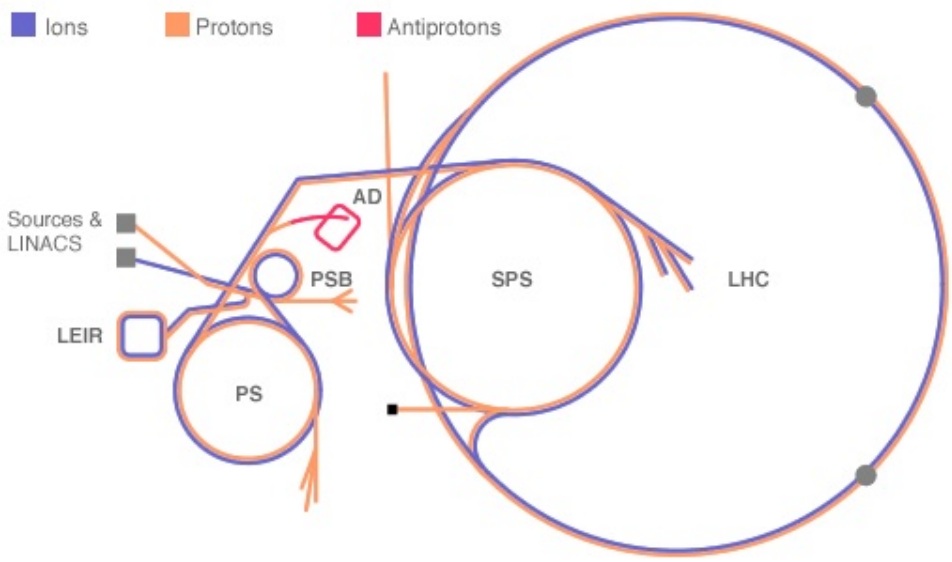

Figure 3.2: LHC injection complex.

3.1.3 The LHC as an ion collider

Heavy-ion collisions were included in the conceptual design of the LHC from an early stage. The nominal magnetic field of 8.33 T in the dipole magnets will allow for a beam energy of 2.76 TeV/nucleon yielding a total center-of-mass energy of 1.15 PeV at a design luminosity of $1.0\times10^{27}\mathrm{cm}^{-1}\mathrm{s}^{-1}$. Currently, the magnets are operating at half the designed field. Achieving a total center-of-mass energy of 2.76 TeV/nucleon. While the major hardware systems of the LHC ring appear compatible with heavy-ion operation, the beam dynamics and performance limits are quite different from those for *pp* collisions. Some of the aspects of heavy-ion beams are similar to those in proton beams, such as the emittance which has been chosen so that the ion beams have the same geometric size as the proton beams.

The lead ions are produced from a highly purified lead sample heated to a temperature of about 550° C. Many different charge states are produced with a maximum around Pb^{+27}. These ions are selected and accelerated to 4.2 MeV/nucleon by the Linear Acceler-

ator (Linac3) before passing thorough a carbon foil, which strips most of them to Pb^{+54}. The Pb^{+54} beam is accumulated, then accelerated to 72 MeV/nucleon into the Low Energy Ion Ring (LEIR). Subsequently, the ions are transfered to the PS and accelerated to 5.9 GeV/nucleon. Then, later get sent to the SPS after first passing them through a second foil where they are fully stripped to Pb^{+82}. The SPS accelerates them to 177 GeV/nucleon and sends them to the LHC where they reach the energy of 2.76 TeV/nucleon.

Ion beam loss by nuclear interaction at the LHC

When ultra-relativistic lead ions collide at LHC energies, numerous processes of nuclear fragmentation and particle production can occur. Some of these have direct consequences for the performance limits of the collider. In addition to the hadronic nuclear interactions of interest due to direct nuclear overlap ultra peripheral collisions (UPCs) of the form

$$^{208}_{82}\mathrm{Pb} + ^{208}_{82}\mathrm{Pb} \xrightarrow{\text{nuclear}} \mathrm{X} \tag{3.10}$$

yield a cross section of $\sigma_{\mathrm{H}} \approx 8$ barn which gives way to the longer range electromagnetic interactions. All contributions to the total cross section will affect the total beam loss rate and the resulting beam lifetime. However, certain processes cause concentrated particle losses. By heating localized sections of the LHC, resulting in a magnet quench. One of these processes is electron capture from pair production (EECP). In electromagnetic dissociation (EMD), the lead ion makes a transition to an excited state and then decays by emitting a neutron, leaving a lighter isotope. The total cross section for the removal of an ion from the beam is

$$\sigma_{\mathrm{Total}} = \sigma_{\mathrm{hadronic}} + \sigma_{\mathrm{EECP}} + \sigma_{\mathrm{EMD}} \tag{3.11}$$

Synchrotron radiation

The LHC is not only the first proton storage ring in which synchrotron radiation plays a noticeable role, but also the first heavy-ion ring in which synchrotron radiation has

a significant effect on beam dynamics. Surprisingly, some of these effects are stronger for lead ions than for protons because charges in the ions behave coherently. Quantities such as the energy loss per turn from synchrotron radiation and the radiation damping time for ions are obtained from the familiar formulae for electrons by replacing the classical electron radius and the mass by those of the ions. Radiation damping for lead ions such as lead is about a factor of two faster than for protons. In addition, the emittance-damping times are comparable with the growth times from intra-beam scattering [52].

3.2 The CMS detector

3.2.1 Overview

The Compact Muon Solenoid (CMS) is one of the four experiments that are part of the LHC. It is located in the LHC main ring at point-5, 100 meters underground, in Cessy, France. CMS, is one of the two multi-purpose experiments at the LHC (ATLAS is the other). While the CMS program spans many areas of high-energy and heavy-ion physics, it is especially suited for the high-p_T regime. As a discovery machine, one of the main areas of interest comprises the search for the Higgs Boson(s) in the Standard Model and its extensions, such as the search for SUperSYmmetry (SUSY), and extra dimensions. At the center of the heavy-ion program is the study of strongly-interacting matter produced in $PbPb$ collisions at the highest energy densities ever reached in the laboratory. To achieve this, CMS makes use of various types of technologies that compliment each other and ensure robust measurements. Very good tracking resolution, a wide calorimetric coverage, great muon identification, a fast triggering system and a 4 Tesla magnetic field are some of the key components that make up this state-of-the art-detector. The main requirements for CMS to meet the physics goals are:

- Good muon identification and momentum resolution over a wide range of momenta and angles, good dimuon mass resolution ($\approx$ 1% at 100 GeV), and the ability to unambiguously determine the muon charge for $p_T < 1$ TeV/c.

- Good charged particle momentum resolution and reconstruction efficiency in the inner

tracker. Efficient triggering and offline tagging of τ's and b-jets require a pixel detector close to the interaction point.

- Good electromagnetic energy resolution, good diphoton and dielectron mass resolution ($\approx 1\%$ at 100 GeV), wide geometric coverage, π^0 identification and eventual rejection, and efficient photon and lepton isolation at high luminosity.

- Good missing-transverse-energy and jet-energy resolution, requiring hadronic calorimeters with large (nearly hermetic) geometric coverage and fine lateral segmentation.

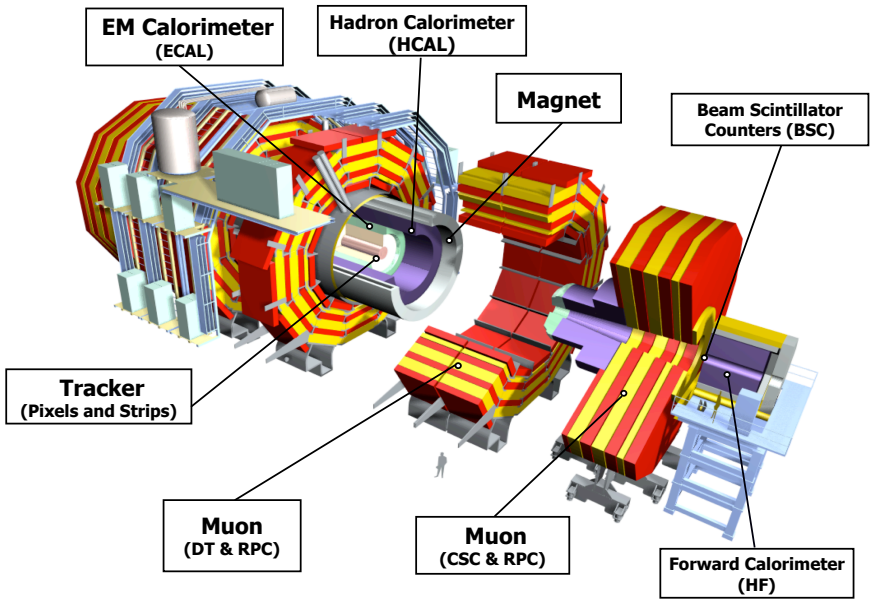

Figure 3.3: The CMS detector

A reference set of coordinates was adopted by the CMS collaboration in which the origin is at the center of the detector where collisions are expected to occur. The z-axis points along the beam axis towards the Jura mountains; the y-axis points vertically up, and the positive x-axis points inward towards the center of the LHC. A more "detector friendly" set of coordinates is the cylindrical set, in which the z-coordinate is the same as the z-axis, the ϕ-coordinate surrounds the z-axis in azimuth and the radial coordinate

increases perpendicular to the z-axis. In collider physics it is more useful to define the variable η, known as pseudorapidity. It is a variable defined with respect to the center of the detector, where the collisions occur,

$$\eta = -\ln\left[\tan(\theta/2)\right] \tag{3.12}$$

The CMS detector is roughly 22 m in length, 15 m in diameter and 12 500 metric tons in weight. A complete description of the construction and performance can be found in Ref. [53]. The central feature is a 4 Tesla solenoid magnet, 13 m in length and 6 m in diameter. A silicon tracker, utilizing both pixel and micro strip technologies, is the innermost detector subsystem in the central rapidity region. An electromagnetic calorimeter (ECAL) with a coverage of $|\eta| < 3$ and a hadronic calorimeter (HCAL) $|\eta| < 5$ are located within the magnet solenoid. The outermost subsystems are muon detectors with a coverage of $|\eta| < 2.4$, embedded in the return yoke. Three different technologies are used for muon detection. The Cathode Strip Chambers (CSC) and Resistive Plate Chambers (RPC) cover the endcaps while the RPCs and Drift Tubes (DT) span the barrel region. Three other detectors are located in the forward region. The CASTOR detector covers $5.3 < |\eta| < 6.6$, while a zero-degree calorimeter (ZDC) covers $|\eta| > 8.3$. To complement CMS, the TOTEM experiment will measure the total pp cross section by a luminosity-independent method and study elastic and diffractive scattering at the LHC.

3.2.2 Inner tracker

The inner tracker is comprised of two technologies. Radially, the innermost component is a silicon pixel tracker (PIX), followed by the silicon strip tracker (ST). The PIX is the closest detector to the interaction region and therefore subject to the largest particle flux. The size of a pixel is $\approx 100 \times 150\ \mu\text{m}^2$ giving an occupancy of about 10^{-4} per pixel per LHC crossing in the pp collision scenario. In the intermediate region ($20 < r < 55$ cm) the particle flux is low enough to make use of larger pitch microstrips with an occupancy $\approx$ 2-5% per LHC crossing. In the outermost region ($r \leq 55$ cm) the occupancy of $\approx$1% allows for the use of larger silicon strip of size 25 cm $\times$ 180 μm. In $PbPb$ collisions the occupancy

is expected to be kept at ≈ 1% in the pixels, while it is expected to be at around 20% in the silicon strips.

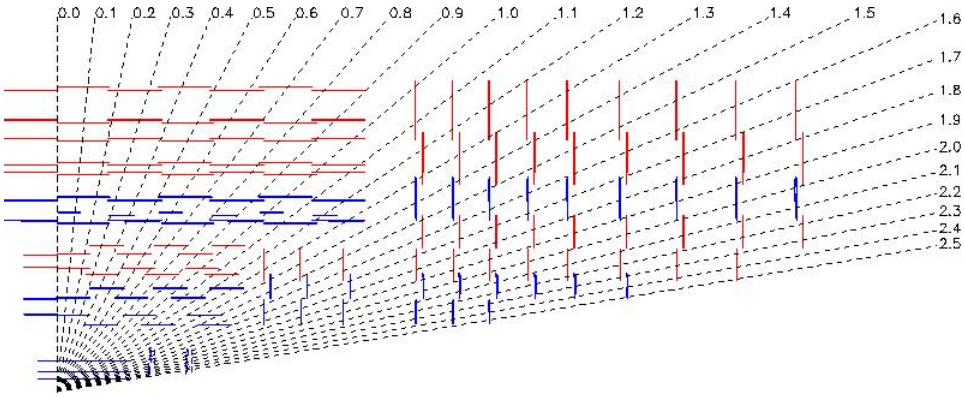

Figure 3.4: Quarter view of inner tracker. The coverage extends up to 2.5 units in η. The innermost layers are the silicon pixels. The outer layers are the silicon strips.

The PIX detector is made up of three layers at radii of 4, 7 and 11 cm in the barrel region. In the endcap, there are two layers of pixels. The silicon strip detectors are placed at radii between 20 and 110 cm while, in the forward region, there are 9 microstrip layers. Figure 3.4 shows a quarter view of the inner tracker layers. The total area of the pixel detector is ≈ 1 m^2 while the silicon strips span an area of ∼ 200 m^2 with a coverage up to $|\eta| < 2.4$. The inner tracker comprises 66 million pixels and 9.6 million silicon strips [54]. In order to achieve optimal vertex position resolution, an almost square pixel shape of 100 × 150 μm^2 in both the (r, ϕ) plane and the z-coordinate was adopted. The barrel region of the tracker comprises 768 pixel modules arranged into half-ladders of 4 identical modules each. The large Lorentz effect (Lorentz angle 23°) improves the r-ϕ resolution through charge sharing. The endcap disks are assembled in a turbine-like geometry with blades rotated by 20° to benefit from the Lorentz effect.

3.2.3 ECAL

The ECAL is a hermetic, homogeneous calorimeter comprising 61 200 lead tungstate ($PbWO_4$) crystals mounted in the central barrel, complemented by 7324 crystals in each of the endcaps. The crystals have short radiation lengths, $\chi_0 = 0.89$ cm, and have a Molière

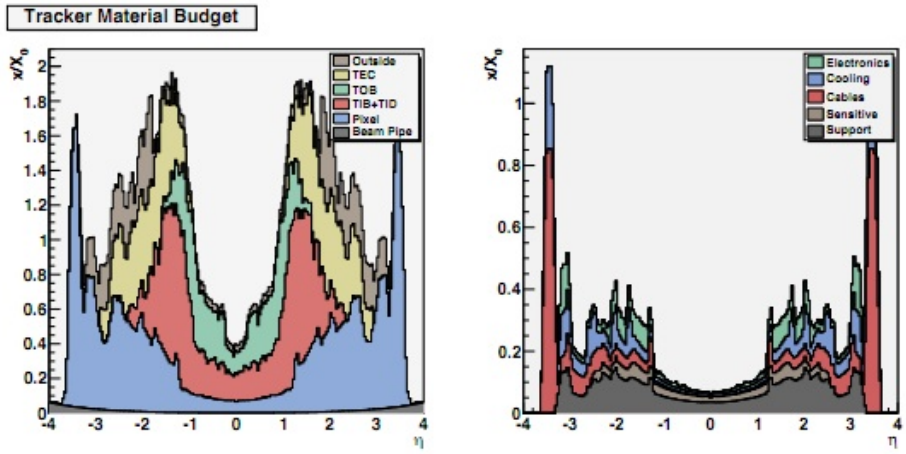

Figure 3.5: Material budget of tracker system and pixel detectors.

radius of 2.2 cm. The crystals have a fast response time, 80% of the light is emitted within 25 ns, and are radiation hard, up to 10 Mrad. Avalanche photodiodes (APDs) are used as photodetectors in the barrel and vacuum phototriodes (VPTs) in the endcaps.

The barrel section has an inner radius of 129 cm. It is structured as 35 identical "supermodules", each covering half the barrel length and corresponding to a pseudorapidity interval of $0 < |\eta| < 1.479$. The crystals have a front face cross section of $\approx 22 \times 22$ mm^2 and a length of 230 mm, corresponding to 25.8 χ_0.

The endcaps, at a distance of 314 cm from the vertex and covering a pseudorapidity range of $1.479 < |\eta| < 3.0$, are structured as 2 back-to-back semi-circular aluminum plates formed of structural units of 5×5 crystals, know as "supercrystals". The endcap crystals are arranged in an $x - y$ grid (not an $\eta - \phi$ grid). They are all identical and have a front face cross section of 28.6×28.6 mm^2 and a length of 220 mm (24.7 χ_0) [53].

3.2.4 HCAL

The design of the hadron calorimeter was driven by the choice of magnet parameters since most of the CMS calorimetry is located inside the magnet coil and surrounds the ECAL system. An important requirement of the HCAL is to minimize the non-Gaussian tails in the energy resolution and to provide good containment and hermeticity for the missing transverse energy. Thus, the HCAL design maximizes material inside the magnet coil in

terms of interaction lengths and is complemented by an extra layer of scintillators referred to as the Hadron Outer (HO) detector, placed outside the coil. The absorber material layers are made out of brass, which is non-magnetic and has a short interaction length.

The barrel part of the HCAL covers -1.4 $< \eta <$ 1.4, which translate to 2304 towers with a segmentation $\Delta\eta \times \Delta\phi = 0.087 \times 0.087$. There are 15 brass plates in total, each with a thickness of about 5 cm, plus 2 external stainless steel plates for mechanical strength. Particles leaving the ECAL volume see first a scintillator plate with thickness of 9 mm instead of the 3.7 mm thickness of the other plates. The light collected by the first layer is optimized to be about 1.5 times higher that the other scintillator plates.

The Hadron Outer detector covers the region -1.26 $< \eta <$ 1.26 which lies outside the coil. It samples the energy from penetrating hadron showers leaking through the rear of the calorimeters and make it past the magnet, increasing the effective thickness of the hadron calorimeter to over 10 interaction lengths (λ). All this reduces the energy resolution but improves the missing transverse energy resolution of the calorimeter. The Hadron Endcaps consist of 14 η towers with 5° segmentation in ϕ, covering the pseudorapidity region $1.3 < |\eta| < 3.0$, making a total of 2304 towers.

The Hadron Forward (HF) calorimeter covers the pseudorapidity range between 3.0 and 5.0. It is made out of steel/quartz fiber. The front face of the HF is located 11.2 m from the interaction point with a depth of 1.65 m. Because the neutral component of the hadron shower is preferentially sampled in the HF calorimeter, this design leads to narrower and shorter hadronic showers and hence is ideally suited for the congested environment of the forward region.

3.2.5 Muon systems

Muons are very valuable observables in CMS. They can be cleanly and unambiguously reconstructed, unlike jets or photons, and can be easily identified over the background, unlike electrons. The CMS muon system has three requirements: muon identification, muon trigger, and muon measurement. Comprehensive simulation studies have indicated that the physics goals can be achieved if the muon detector has the following functionality and performance [55]:

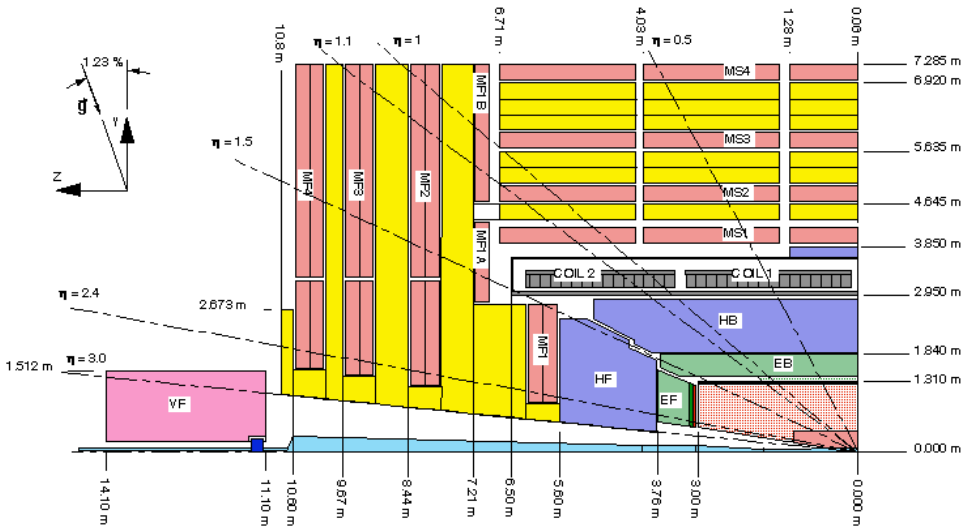

Figure 3.6: General layout of the different detectors that make up CMS. In light red, the muon chambers DT and CSC.

- Muon identification: at least 16λ of material is present up to $\eta = 2.4$ with redundant coverage of three different technologies.

- Muon trigger: the combination of muon chambers with precise resolution and a fast dedicated trigger detectors provide unambiguous beam crossing identification and allows triggering on single and multimuon events with well defined p_T thresholds from a few GeV to 100 GeV up to $\eta = 2.1$.

- Stand-alone momentum reconstruction from 8 to 15% $\sigma(\delta_{p_T})/p_T$ at a $p_T$of 10 GeV/c and 20 to 40 % at 1 TeV/c of transverse momenta.

- Global momentum resolution: after matching with the Inner Tracker, the resolution is from 1.0 to 1.5 % at $p_T = 10$ GeV/c, and 6 to 17% at 1 TeV. The momentum-dependent spatial position matching at 1 TeV/c is less than 1 mm in the bending plane and less than 10 mm in the non-bending plane.

- Charge Assignment: correct 99% confidence up to the kinematic limit of 7 TeV.

- Radiation hard: capable of withstanding the high radiation and the interaction background expected at the LHC.

The muon chambers are the outermost subsystems in the main body of the CMS detector. Direct muons that make it to the chambers have already been measured in the tracker and have made it through the magnet coil, which removes a sizable portion of punch-through hadrons. Backsplash from the face of the HF and the quadrupole magnet can produce a fake muon, especially in the outermost endcap chambers closest to the beam [55]. There are many factors that can limit the ability of the muon system to accurately measure the muon momentum:

- multiple scattering in the calorimeters and in the thick steel plates separating the muons stations;
- intrinsic resolution limitations of the detectors;
- energy loss from interaction with the materials of the detectors;
- extra detector hits generated by muon radiation, δ-rays, and other backgrounds;
- chamber misalignment;
- uncertainty in the B field;

The muon momentum resolution is defined in Eq. 3.13

$$\frac{\delta p_T}{p_T} = \frac{1/p_T^{\text{meas}} - 1/p_T^{\text{gen}}}{1/p_T^{\text{gen}}} \tag{3.13}$$

Figure 3.7 shows the p_T resolution for 2 pseudorapidity regions: the barrel (left) and endcaps (right). The p_T resolution of a "Full System" muon is obtained from the measurements in the tracker at low p_T, while at high-p_T the resolution is guided by the measurement in the muon chambers. It is also visible that the resolution worsens in the forward region due to the "weaker" bending experienced by forward tracks that exit the solenoid traversing a smaller radial distance.

CMS uses three gaseous detectors for muon identification: Drift Tubes (DT), Cathode Strip Chambers (CSC) and Resistive Plate Chambers (RPC).

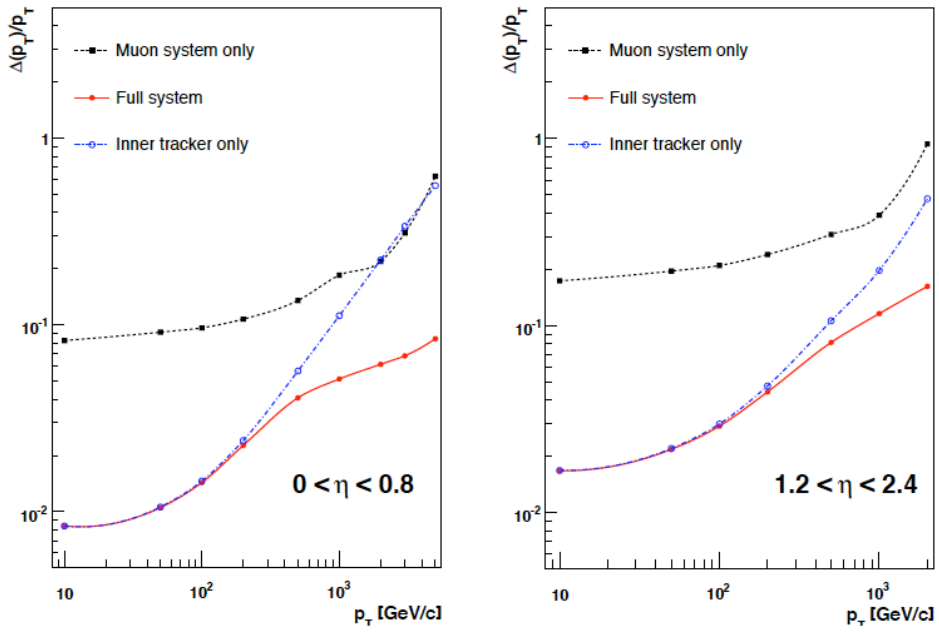

Figure 3.7: Muon p_T resolution in barrel region (left) and forward region (right).

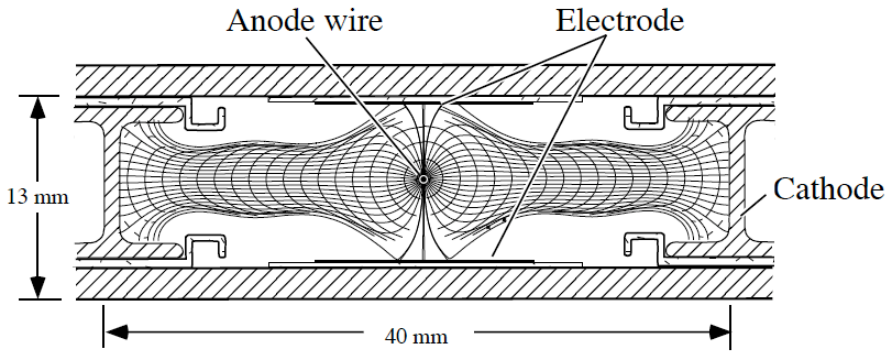

Figure 3.8: Drift Tube cell.

3.2.6 Drift Tubes

The Drift Tubes are located in the barrel region and have a coverage of $|\eta|$ <1.2. They are organized in 5 stations along the z-axis. Each station is made up of 4 concentric rings along the radial direction, as shown in Fig 3.9. This choice of detector for the barrel part is due to the low expected rate and the relatively low intensity of the local magnetic field. The principal wire length, around 2.5 m, is constrained by the longitudinal segmentation of the iron barrel yoke. The transverse dimension of the drift cell was chosen to be

2 cm or 350-400 μs. The tracking and timing performance of a chamber was optimized with a design using twelve layers of DTs divided into three groups of four consecutive layers named Super Layers (SL). Two SLs measure the (r,ϕ) coordinate, i.e. have wires parallel to the beam line, while the third measures the z-coordinate. The mechanical precision of the chamber construction is dictated by the aim to achieve the global resolution in (r,ϕ) of 100 μm. This is achieved by the 8 track points measured in the two (r,ϕ) SL, if the angular wire resolution is better than 250 μm. The cells operate at atmospheric pressure with an Ar/CO_2 gas mixture with a CO_2 concentration at 10- 20%.

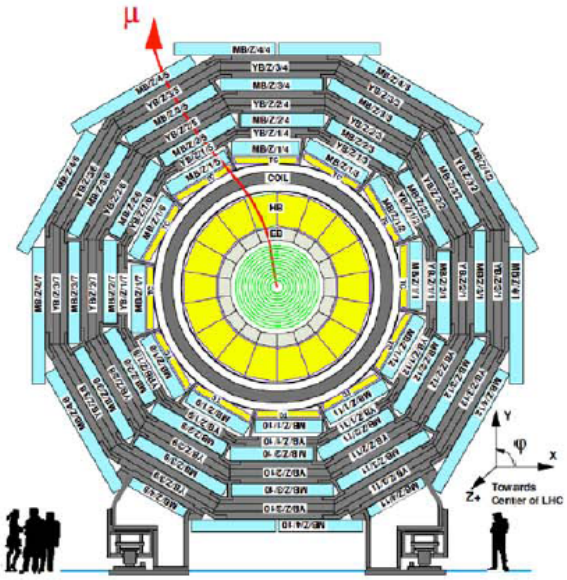

Figure 3.9: Layout of muon detector in the barrel region. In blue the DT and gray the return yoke. A muon track exemplified in red.

The baseline cell design is shown in Fig 3.8, it has a pitch if 40 mm by 13 mm. At the center is the anode wire, made out of 50 μm diameter stainless steel. The cathodes defining the cell width are aluminum I-beams which are 1.2 mm thick and 9.6 mm high. A plastic profile is glued to the upper and lower side of the I-beams to isolate from the cathode. The wall plates are kept at ground potential, and a drift field is formed by putting the wires at positive voltage and the cathode wire at negative. A pair of positively-charged strips has the effect of squeezing the drift lines, improving the linearity of the space-time relationship and resolution of the cell.

3.2.7 Cathode Strip Chambers

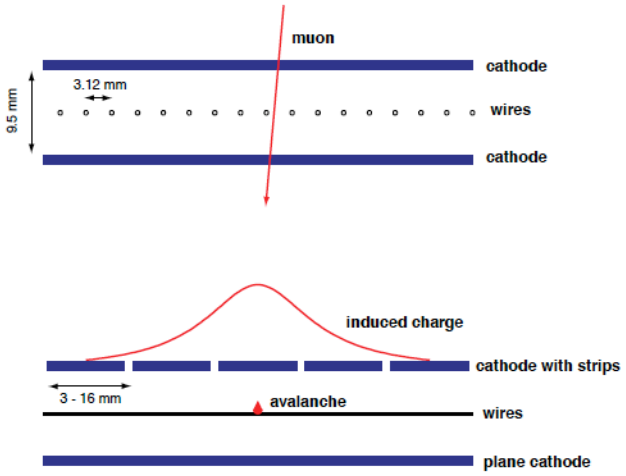

Figure 3.10: Coordinate measure of the CSCs. It shows the trajectory of a muon (top) and the induced charge left (bottom) that will be read

The Cathode Strip Chambers are part of the muon endcaps and have a coverage of $|\eta| > 0.8$. The CSCs are arranged in four discs on each side of the CMS barrel with full ϕ coverage. Each disk consists of concentric rings. Each ring is comprised of 18 or 26 stations. The cracks between the chamber rings are not projective and thus coverage, defined as hits in at least 3 chambers on a muon path, is close to 100%. The arrangement can be seen in Fig. 3.11. The CSCs are multi-wire proportional chambers in which one cathode plane is segmented into strips running across wires. An avalanche developed on a wire induces a disturbed charge of a well known shape on the cathode plane, see Fig. 3.10. Charpak *et al.* [56] showed that, by interpolating the fractions of charge picked up by these strips, one can reconstruct the track position along the wire with a precision of 50 μm or better. A typical CSC is a six plane chamber of trapezoidal shape with maximum length of 3.4 m and a maximum width of 1.5 m. The major advantages of the CSCs are:

- their intrinsic spatial resolution, can be as good as 50 μm,
- closely spaced wires make the CSC a fast detector, with a time resolution of up to 6 ns,

- by measuring signals from strips and wires, one easily obtains two coordinates from a single detector plane,
- strips are fan-shaped to measure ϕ coordinate naturally,
- CSCs can operate in a large non-uniform magnetic field without significant deterioration to the performance,
- gas mixture composition, temperature and pressure do not directly affect CSC precision and thus stringent control of these variables is not required.

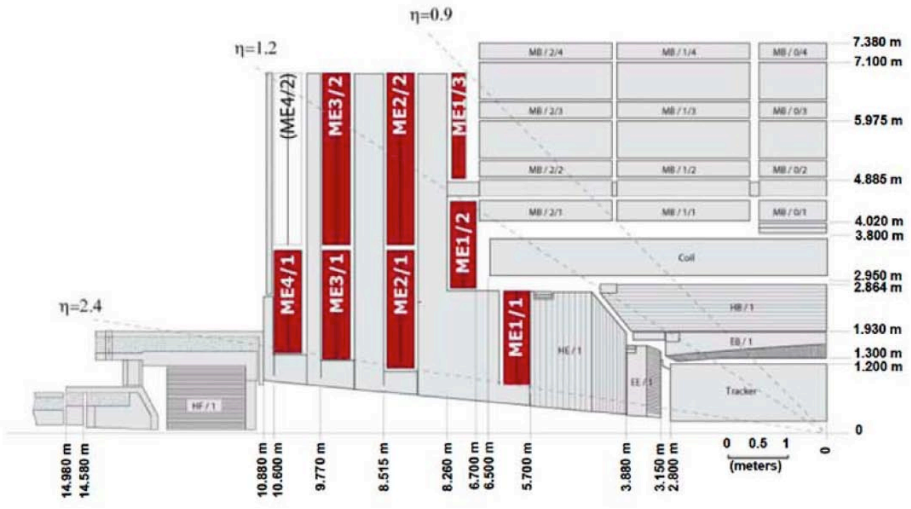

Figure 3.11: Location of CSCs (in red) within the muon system.

Standard nomenclature refers to the subsystems as ME i/j where i labels the station and j the ring. Thus for example the innermost ring of the rst station, closest to the Interaction Point, is called ME1/1. All the CSCs lay outside the magnet except for the innermost ring of the first disk, the ME1/1 chambers. Given their positions they operate in an axial magnetic field. To compensate for this, the chambers are tilted by 25° with respect to a perpendicular to the chamber centerline. Since these chambers are the closest to the collision point, they experience a high interaction rate. The main source of background hits comes from random hits from neutrons/gammas (after knocking out electrons from the surrounding materials), punch-through, pion and kaon decays-in-flight, tunnel muons and debris from muons going through detector hardware.

3.2.8 Resistive Plate Chambers

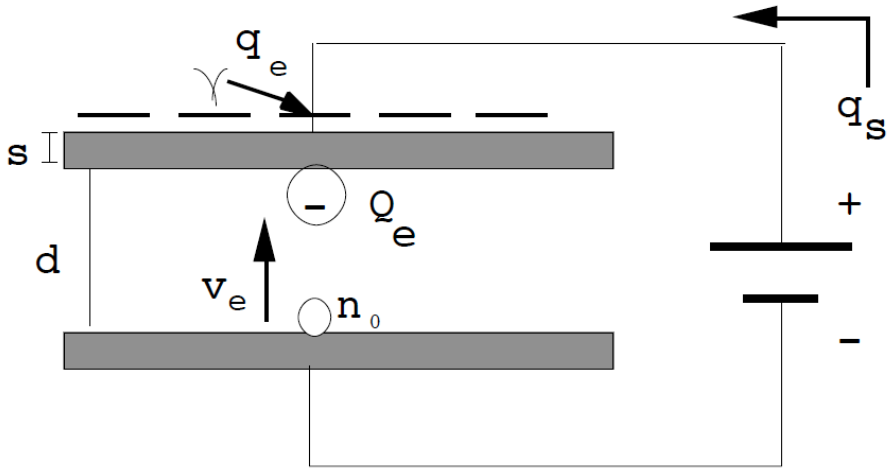

Figure 3.12: Schematic of parallel plates that make up the RPCs.

The RPC are gaseous parallel-plate detectors that combine adequate spatial resolution with time resolution comparable to that of the scintillators [57]. An RPC is capable of tagging the time of an ionizing event with a time resolution in a much shorter time, 3ns, than the 25 ns between two consecutive LHC bunch crossings. Therefore, a fast, dedicated muon trigger can unambiguously identify the relevant bunch crossing at the design rate expected from the LHC. The RPC system offers a redundancy in the muon coverage, extending over the region $|\eta| < 2.1$ with full ϕ-coverage. An RPC-based trigger has to perform three basic functions simultaneously:

- identify a muon candidate;
- assign a bunch crossing to candidate track(s);
- and estimate the muon transverse momenta.

An RPC consists of two parallel plates separated by a gas gap of a few millimeters. The outer surfaces of the resistive material are coated with conductive graphite paint to form the HV and ground electrodes. The electrode resistivity mainly determines the rate, while the gap determines the time performance. Figure 3.12 shows a diagram of the RPC

operation. A cluster of n_o electrons, produced by an ionizing particle, ignites the avalanche multiplication. An electronic charge Q_e is then developed inside the gap of height d. The drift of the charge towards the anode induces a fast charge q_e on the pick-up electrode, which represents the useful signal of the RPC.

3.2.9 Forward detectors

The Beam Scintillator Counters (BSC) are a set of large area scintillators mounted in front of the HF to provide raw timing and beam halo information. The BSCs are composed of 32 (BSC1) + 4 (BSC2) polyvinyl-toluene plastic scintillator tiles. The location of the BSC tiles in front of and behind the HF reduces the ambiguity of measuring the particle timing. The inner BSC detector tiles are known as disks while the outer tiles are known as paddles [58].

The Beam Pick-Up Timing for experiments (BPTX) are electrodes situated on the LHC ring at $\pm$175 m from the CMS interaction point. The beams passing through the center induce a charge in the electrodes, giving a highly accurate beam timing and position information. The BPTX system is the primary reference for triggering on particle beams passing through CMS. It provides a reliable, zero-bias signal with zero dead-time and is used for triggering several subsequent detectors.

Chapter 4

Simulation and Reconstruction

A generated sample that mimics physical processes based on statistical distributions is also known as a Monte Carlo (MC) sample. The generators that produce these MC samples have parameters that can be tuned to match previous measurements. Once a generator is 'tuned' it can be used to extrapolate a measurement to a region of phase space not accessible by experimental measurements. The use of MC samples allows us to assess detector performance and the state of reconstruction and trigger algorithms prior to the first collisions. In order to accurately evaluate the response of the detector, it is expected that the MC sample properly (or within a certain degree of confidence) reproduces kinematic distributions, multiplicities, etc. at the hardware level. Therefore, an accurate and up-to-date detector geometry parameterization must be part of the simulation. A useful approach to bypass the risk associated with possibly incomplete descriptions of the detector response in the simulation software is to embed a signal event into real collision data.

4.1 Simulation of $Z^0 \rightarrow \mu^+\mu^-$ in heavy-ion events

The simulation of specific physical processes in heavy-ion collisions is carried out in steps. Given that the goal of this physics analysis is to measure $Z^0 \rightarrow \mu^+\mu^-$ events in heavy-ion collisions, a 'signal' $Z^0 \rightarrow \mu^+\mu^-$ event is generated first. The kinematics of these signal distributions can be constrained to the detector phase-space has coverage to maximize the use of computing power. Once the signal events are generated, they will be

embedded into a heavy-ion event at the sim level, that is when the detector response has been simulated. At the *simulation step* (sim) the response from the detectors prompted by the presence of a particle is after the 'signal', and heavy-ion event are successfully merged so that they can be reconstructed seamlessly as one event.

4.1.1 Generation of the $Z^0 \rightarrow \mu^+\mu^-$ signal

The generation of the $Z^0 \rightarrow \mu^+\mu^-$ process can be carried out in different ways. A simple PYTHIA *pp* collision simulation can be embedded into a heavy-ion event. PYTHIA will generate Z^0s simulated *pp* events according to realistic distributions, including regions of phase space not accessible in the current detector configuration. A much simpler and efficient way is to employ PYTHIA as a 'particle gun'. A particle gun is a randomly generates a mother particle, based on a distribution defined in rapidity (y^Z) and transverse momentum (p_T^Z) space. After the mother particle has been generated, it is allowed to decay according to 2-body decay kinematics. To optimize the computing resources the Z^0s were restricted to decay only into $\mu^+\mu^-$ pairs. The Z^0s from the particle gun were generated with a flat rapidity distribution within the CMS (barrel and endcaps) region $|y^Z|$ <2.4, and a flat $p_T$distribution for $p_T^Z \leq 50$ GeV/c. The use of these flat distributions is to uniformly span the relevant phase space region. A re-weighing of events with a more realistic distribution is applied later in the analysis.

4.1.2 Generating heavy-ion events

The generation of heavy-ion events was carried out using the HYDJET generator [59]. HYDJET is a heavy-ion event generator that simulates jet production, jet quenching and flow effects in ultra-relativistic heavy-ion collisions. The selection on impact parameter was not restricted in the generated heavy-ion events in order to obtain a minimum bias distribution of collision centralities.

4.1.3 $Z^0 \rightarrow \mu^+\mu^-$ embedding in HYDJET events

The method to combine the signal event with the heavy-ion events is known as embedding. The CMS software tool used for this purpose is the `DataMixer`, also used

to study detector noise and pile-up events. In order to preserve as much information as possible, the philosophy is to merge the data streams at the earliest stage where the two streams have the same format. In this method, a collection of pre-generated events at the sim level is accessed. For each event, the vertex location is found [60]. The signal event is forced to match the same vertex location and is generated "on the fly". At the sim level, both collections are merged into one. From this point on, the merged collection will go through the subsequent analysis stages as a single collection.

4.1.4 $Z^0 \rightarrow \mu^+\mu^-$ embedding in real heavy-ion data

A more reliable method of evaluating the performance of the trigger and reconstruction algorithms is to embed a simulated signal into a real data event. The advantage of this approach is that the uncertainties related to the accuracy of the heavy-ion generator are completely removed. The uncertainty related to the accuracy of the hardware detector response remains. However, it is greatly reduced because it only affects the decay muons. The detector response includes dead channels, chambers and sectors of the many subdetectors. A minimum bias sample was used for this study. The embedding procedure was the same as described in the previous section. This sample was produced by embedding one $Z^0 \rightarrow \mu^+\mu^-$ event in each minbias event. A comparison between samples ($Z^0 \rightarrow \mu^+\mu^-$ into HYDJET and $Z^0 \rightarrow \mu^+\mu^-$ in real data) is done to ensure the reliability of the heavy-ion generator, as discussed in Sec. 5.2.4.

4.2 Reconstruction

The goal of a reconstruction algorithm is to accurately read the event from the information collected from all the subdetectors. The reconstruction, in a general way, depends on the detector configuration and occupancy. The occupancy is dependent on the event multiplicity. The main difference between *pp* events and heavy-ion events is the increase in the multiplicity of low-momentum particles by $\sim$ 2-3 orders of magnitude. The increase in the occupancy is more dramatic in the innermost detectors, such as the inner tracker and calorimeters. A significant increase in occupancy is also detected in the forward

region of the muon chambers, while in the barrel the 4 Tesla magnetic field prevents most low-p_T tracks from reaching the outermost detectors. The muon occupancy is shown in Fig. 4.1. The muon endcap stations are shown where the innermost stations (ME$\pm$ 1) have the largest number of reconstructed hits (rechits) at the point closest to the beam axis.

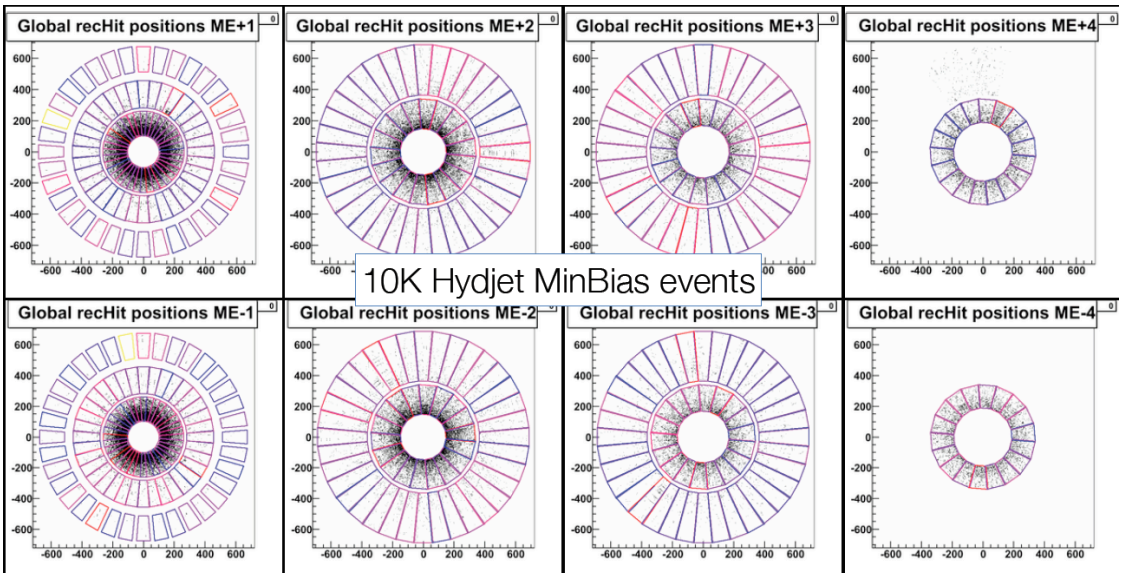

Figure 4.1: Occupancy of the CSC from MC events.

The default reconstruction algorithm used for *pp* collisions is not well suited for the high multiplicity environment. In fact, it runs out of memory when deployed in the most central collisions due to large number of combinatorics when building the large number of tracks in the inner tracker. Calorimetry is also affected by the high level of activity, and needs to be properly rescaled to account for the underlying event. The outside-in approach of the muon reconstruction used for *pp* collsions is already well suited for the reconstruction of muons in heavy-ion collisions, modulo the inner-tracker part of the algorithm.

4.2.1 Heavy-ion tracking

The heavy-ion track reconstruction uses pixel-triplet track seeds constrained to originate from the collision region. It then makes use of the pattern recognition (CKF) algorithm written for track reconstruction in proton-proton events with settings tuned for heavy-ion collisions [61]. The main differences in heavy-ion implementations are the follow-

ing:

- Due to the combinatorics in high multiplicity central heavy ion events, only pixel triplets (and not pixel pairs) are used in track seeding;
- The tracking is currently done in a single pass, though recent studies have shown that the standard iterative procedure is very effective in peripheral heavy ion collisions (up to around $b \sim 10$fm when the jobs run out of memory). There are plans to develop a set of iterative steps customized to heavy-ion needs.

heavy-ion tracking sequence

The heavy-ion tracking sequence is a series of well defined steps to build and select tracks collection at each stage, while using the track information to identify a collision vertex. The heavy-ion tracking sequence can be briefly described as follows [61]:

- **hiPixelClusterVertex** This step provides a rough estimate of the z-vertex position obtained by maximizing the compatibility of the pixel cluster lengths with their z-positions. This vertex is used to constrain the tracking region for the following step.
- **hiPixel3ProtoTracks** This is a collection of pixel-triplet tracks (without primary vertex constraint and using a variable-size tracking region based on pixel-hit multiplicity) that are the input to the median vertex algorithm.
- **hiPixelMedianVertex** The median vertex is a fast and multiplicity-dependent algorithm. The $\eta - \phi$ window is reduced in central events to allow for fast processing;
- **hiSelectedProtoTracks** A subset of the `ProtoTracks` collection consisting of those tracks that are compatible with the median vertex z-position and transverse position of the beamspot. They are feed into the slower but more precise 3D adaptive vertex fitter (next step). The minimum p_T of the selected prototracks is variably dropped from 1.0 to 0.075 GeV depending on the pixel hit multiplicity so that peripheral events have more tracks available to form the vertex.
- **hiPixelAdaptiveVertex** This is the collection of vertices calculated using `hiSelectedProtoTracks` selected based on the x-vertex compatibility.

- **hiBestAdaptiveVertex** This step contains only the adaptive vertex with the most associated tracks.

- **hiSelectedVertex** The same as `hiBestAdaptiveVertex` unless the adaptive algorithm failed (e.g. not enough prototracks), in which case the median vertex is used. If that fails, the beamspot is copied as the "selected vertex". The associated errors are also copied over. The beamspot can have a statistical precision of 2μm [62].

- **hiPixel3PrimTracks** This includes the collection of pixel-triplet tracks that are constrained to originate from a tracking region around the selected vertex obtained in the previous step.

- **hiPixelTrackSeeds** The seeds are generated from the above pixel tracks and used to seed the full track.

- **hiPrimTrackCandidates** These are the track candidates from the trajectory propagator through the strip tracker.

- **hiGlobalPrimTracks** This represents the output of a global covariance fit to the `hiPrimTrackCandidates`.

- **hiSelectedTracks** The subset of the above tracks that pass some track quality cuts, such as compatibility with vertex, number of hits, etc.

In order to minimize the contribution of fake and non-primary tracks while maintaining relatively high efficiency in the highest track density environment, additional quality selection criteria were applied to the tracks from the `hiGlobalPrimTrack` (Sec. 5.2.4) collection in the standard heavy-ion tracking collection. The `hiGlobalPrimTrack` collelction is used to reconstruct a global muons, these tracks are also know as tracker tracks.

4.2.2 Vertex

To calculate the vertex in heavy-ion events, the first step is to get a rough estimate of the z-vertex position by stepping in z from -20 to 20 cm and determining the compatibility of the pixel cluster lengths with the vertex hypothesis. For each step, the number

of compatible hits based on the cluster length is calculated. The z-vertex step with the maximum number of compatible hits is called the 'cluster vertex'. After finding the cluster vertex, the track reconstruction of the pixel-triplet tracks is initiated. Figure 4.2 compares the vertex z distribution from data and MC.

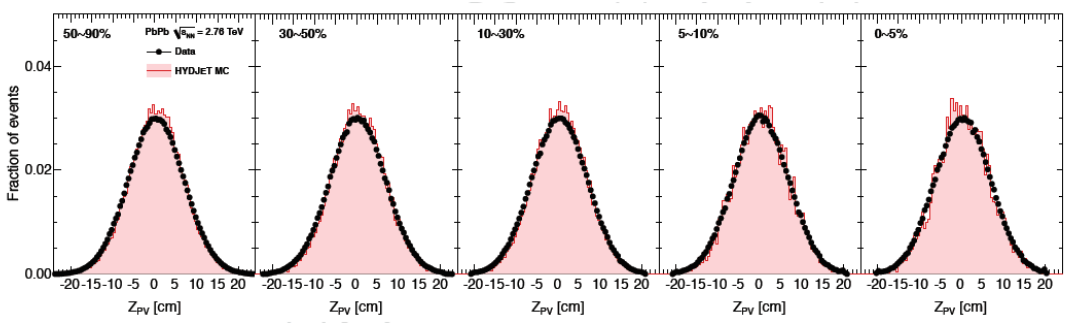

Figure 4.2: z-vertex position from HYDJET and data events in different centrality classes.

A data-driven vertex resolution study was carried out by dividing all the tracks in a single event into two sub-events. The difference between the vertices reconstructed in the two sub-events is related to the resolution in x, y, and z. Figure 4.3 shows the x-axis vertex resolution vs. the number of tracks.

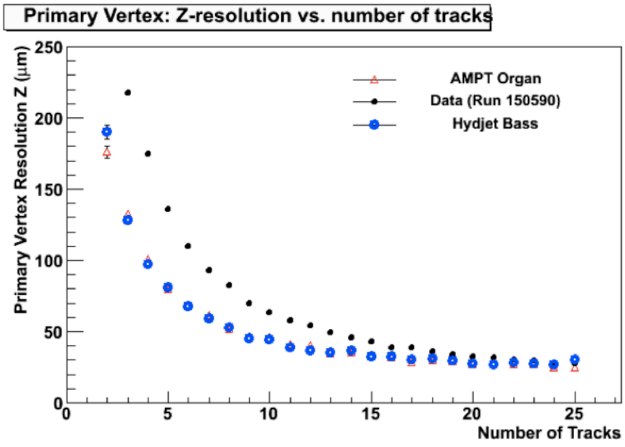

Figure 4.3: z-vertex position resolution vs number of tracks with AMPT, HYDJETsimulations compared to HI data samples

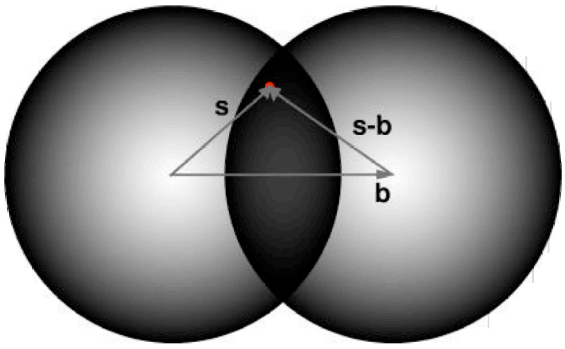

Figure 4.4: Overlap region of two nuclei [4].

4.2.3 Centrality

The centrality variable is calculated based on HF energy deposits which are classified according to the fraction of the total inelastic cross-section. Details can be found in Ref. [63]. Heavy-ion collisions can occur over a range of impact parameters, from head-on (central) collisions to grazing (peripheral) interactions. By approximating each of the colliding nuclei as spheres with a density profile, the centrality of the collision can be characterized by the geometric overlap of the two nuclei. The distance between the two centers of the spheres is the impact parameter, b. The overlap region is the "almond-shape" area where the two colliding nuclei are superimposed, as seen from the beam axis, Fig. 4.4. If $\int d^2s\ T_A(s) = 1$, the overlap region is represented by the overlap function T_{AB},

$$T_{AA}(b) = \int d^2s\ T_A(s) T_A(b-s) \tag{4.1}$$

where $T_A(s)$ and $T_A(b-s)$ are the nuclear profile functions, based on Woods-Saxon parameterizations, for nuclei A and B. Integrating Eq 4.1 over all impact parameters we get the normalization.

$$\int d^2b\ T_{AA}(b) = 1 \tag{4.2}$$

The probability to have n inelastic baryon-baryon collisions at an impact parameter b is given by

$$P(n,b) = \begin{pmatrix} A^2 \\ n \end{pmatrix} [T(b)\sigma_{pp}]^n [1 - T(b)\sigma_{pp}]^{A^2-n} \tag{4.3}$$

where the first factor represents the number of combinations giving n collisions out of A^2 possible nucleon-nucleon collisions. The second factor gives the probability of having exactly n collisions, while the third factor is the probability of having exactly A^2 - n misses. The total inelastic cross section is,

$$\sigma_{AA} = \int d^2b \Big\{ 1 - [1 - T(b)\sigma_{pp}]^{A^2} \Big\} \tag{4.4}$$

The experimental centrality determination allows the events to be characterized. Once the experimental centrality value is obtained it can be combined with information obtained "*a priori*" from a geometrical model to infer quantities such as b, $N_{\rm part}$ (number of participant nucleons), and $N_{\rm coll}$ (number of colliding nucleons). The can be defined as follows:

$$N_{\rm coll}(b) = \sigma_{pp}\ A^2\ T_{AA}(b) \tag{4.5}$$

$$N_{\rm part}(b) = 2A \int d^2s\ T_{AA}(s) \Big\{ 1 - \Big(1 - T_{AA}(s-b)\sigma_{pp} \Big)^{A^2} \Big\} \tag{4.6}$$

where σ_{pp} is the pp cross section of a system at the same center-of-mass energy.

Experimental determination of centrality classes

The event centrality in nucleus-nucleus collisions can be determined by measuring the charged particle multiplicities or the transverse energies in various regions of pseudo-rapidity. The signals can be divided in centrality bins. To study their production as a function of centrality. In CMS, the centrality of the event is inferred from the transverse energy deposited in the Hadron Forward calorimeters with coverage $3 < |\eta| < 5.2$. The energy on both sides of the detector is summed up. As a cross check, the pixel detector multiplicity is studied, since it increases monotonically, similar to the HF signals. The number of non-interacting neutrons released from in the collision is measured by the ZDC and

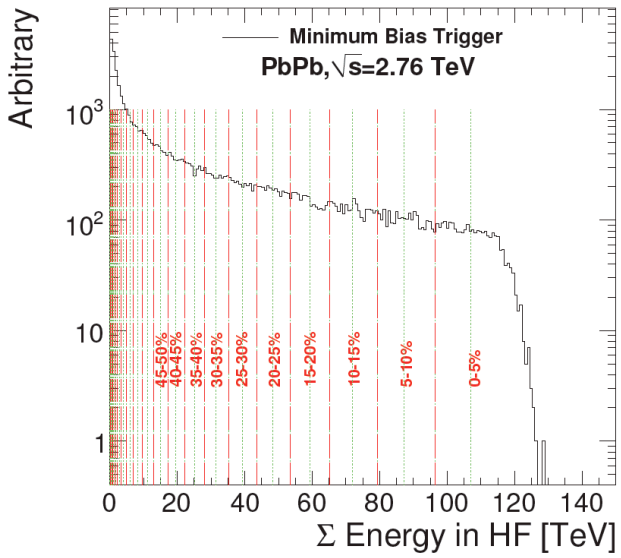

Figure 4.5: HF energy distribution in centrality bins

is negatively correlated with central events. Once the total transverse energy is collected by the HF, it is assigned a centrality bin when compared to the integrated sample. Figure 4.5 shows the centrality bin classes in a HF energy distribution. Using the HF energy-sum limits shown in the figure, bins containing equal fractions of the minimum-bias cross section can be defined. Then they serve as centrality classes for subsequent analysis. The resulting distribution should be flat for a minimum bias data sample by construction, as shown in Fig 4.6. The centrality bins are each assigned $1/40^{\text{th}}$ of the cross section each.

4.2.4 Muon reconstruction

Since the muon is a massive (compared to the electron) lepton, a muon with enough p_T to overcome the magnetic field can make it to the outermost detectors leaving information in all the relevant systems along the way. The muon reconstruction combines inner tracking information with the information collected by the muon chambers, as well as some calorimetry for specific cases. Muons can be thought of as massive electrons that can be traced in the tracker, leaving a minimum ionization signature in the ECAL, and no signal in the HCAL. The muon sub-detectors can track the muon trajectory outside the return yoke. The muon reconstruction is carried out in steps: it starts with the local

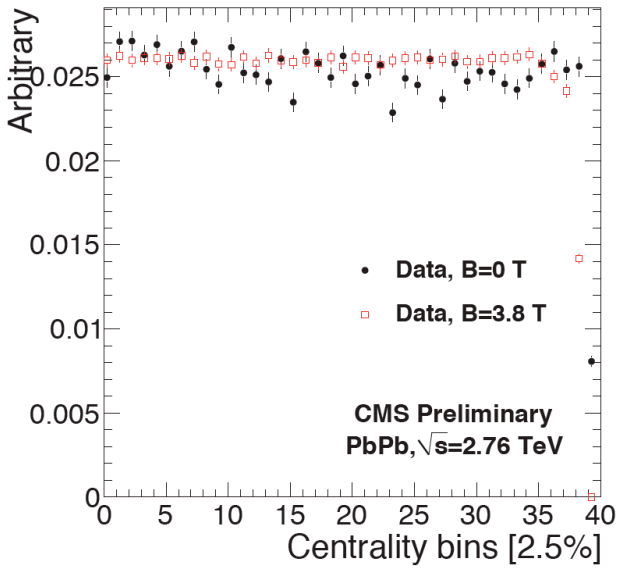

Figure 4.6: Centrality bins in minimum-bias events

reconstruction of 'tracklets' or segments in each of the muon sub-systems and tracker, as explained in Sec 4.2.1. Then the information from the muon systems is combined to form a stand-alone (SA) muon. Finally, the SA muon trajectory is matched to a track from the tracker to form a Global muon.

Local reconstruction

The local reconstruction begins with the identification of a signal left by a traversing particle. Proper interpretation of these signals can be turned into reconstructed hits with a 3-dimensional location. The association of the reconstructed hits into a trajectory forms a segment. The local reconstruction in the CSCs begins with the identification of a pulse in a strip, followed by the cluster hit reconstruction. By identifying the cluster of hits in a CSC layer, the strip with the greatest ADC count is found. Using this as the central strip, the two strips on each side of the central strip are also included to form a hit cluster. The pulse is fitted with a Gatti distribution. The Gatti distribution is not exact since it does not take into account effects due to drift, time dispersion, and non-normal incidence of tracks, but it has been shown in Refs. [55, 64] to be less biased. Before fitting, a wire group is associated with each strip. The local y-coordinate is found from the intersection of each

strip within a wire group with a signal. The local x-position is found by the minimization of the χ^2 determined from the Gatti fit of the pulse distribution. Each of the 6 layers of a chamber provides an independent 2-dimensional reconstructed hit (`rechit`). The `rechits` are fit to form a linear segment. In the case of the CSCs, a segment must have at least 4 hits. Only hits reasonably close (within 2.5 mm in $r-\phi$) to the line [65] are considered. The hits associated with a segment are flagged as 'used' and the procedure is iterated.

The local reconstruction of points in the DT is done by obtaining the distances with respect to the wire multiplying drift time by drift velocities. The reconstruction relies on a time-to-distance parameterization of the cell behavior. The measure $x_{\rm drift}$ is computed as a function of (i) the drift time ($t_{\rm drift}$), (ii) parallel and perpendicular components of the magnetic filed with respect to the wire in the radial direction ($B_{\parallel}$ and $B_{\perp}$) and (iii) the incident angle with respect to the direction of the chamber (α). The component of the magnetic field parallel to the drift lines can be neglected since it has no measurable effect on the drift time. Since the values of $B_{\parallel}$, $B_{\perp}$ and α are not known at the level of the individual hit, a 3-step reconstruction algorithm is implemented. The first step assumes a crude estimate of the impact angle and the hit position along the wire. The hits are updated twice: first, after they have been used to build a 2D $r-\phi$ or $r-z$ segment, and then after the subsequent segment has been used in the 3D segment fit. A segment is built from aligned hits. The segment starts from a pair of hits that must point in the nominal direction of the interaction region. The best segments amongst those sharing hits (solving conflicts, suppressing ghosts) are selected. The hit reconstruction is updated using segment information. Finally, a quality criterion is applied to require $\chi^2/{\rm ndf} < 20$ and more than 3 hits.

The local reconstruction in the RPCs is made out of points in the plane of the detector. First, a clustering procedure starting from all strips that carry signals is performed. By grouping all the adjacent fired strips, a reconstructed point is defined as the center of gravity of the area covered by the cluster of charges. It is assumed that each group of strips is fired by a single particle crossing and that the actual trajectory could have traversed anywhere with a flat probability over the area covered by the strips of the cluster.

Stand-alone muons

Once each of the sub-detectors has read the signals left by a traversing muon, and these signals have been converted into segments in each of the chambers, the information is combined to make the stand-alone muon object. The SA tracking algorithm combines reconstructed track segments and hits using a Kalman filter technique [64] to reconstruct muon trajectories. The track segments are extrapolated taking into account muon energy loss in the material, multiple scattering and non-constant magnetic field. The propagation of the measurement is inside-out at the beginning, collecting hits at each measuring surface of the detectors. First, from the two innermost measurements, trajectory parameters are calculated. These parameters are extrapolated to the next measuring surface and combined with the measurements there. This is done recursively until the outermost layer is reached. The propagation is then reversed to an outside-in direction. A smoothing algorithm is used to incorporate the full information and remove background hits [55]. The final track parameters and their errors are delivered at the innermost muon station. Muon tracks are then propagated through the calorimeters to the nominal vertex position in order to assign a p_T value at the interaction point. The SA muon reconstruction efficiencies are shown in Fig. 4.7.

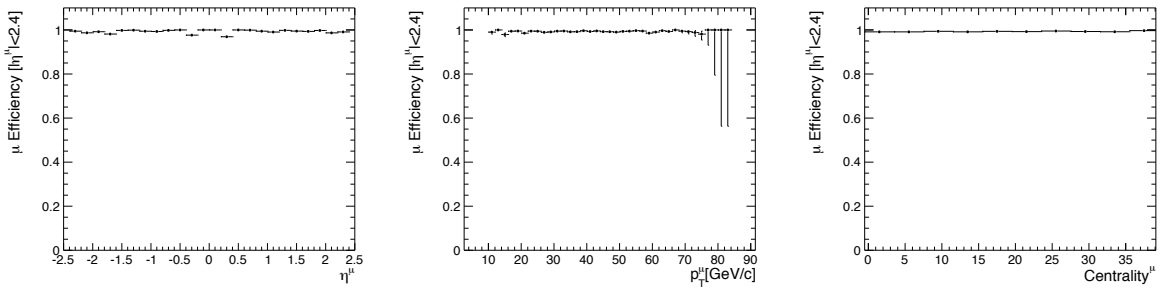

Figure 4.7: Single stand-alone muon reconstruction efficiency from $Z^0 \rightarrow \mu^+\mu^-$ embedded in minbias HYDJET as a function of, p_T (left), pseudorapidity (center) and centrality bin (right)

Global muons

The global muon reconstruction takes the stand-alone muon trajectories and extends them to include tracks in the tracker. The SA muon trajectory is taken from the innermost muon station and extrapolated to the outermost surface of the tracker taking into account energy loss and multiple-scattering effects. The extrapolated trajectory will be used to define an $\eta - \phi$ 'region of interest'. Each of the tracker tracks, specifically the collection `hiGlobalPrimTracks` defined in Sec. 4.2.1, that are within the region of interest are compared one-by-one to the stand-alone muon trajectory. For each "tracker track"-"stand-alone muon" pair an overall fit is performed. The overall fit is performed with the Kalman filter, taking into account energy loss and multiple-scattering effects. The best global muon is selected.

The global muon reconstruction efficiencies are shown in Fig. 4.8. The efficiencies are obtained from a $Z^0 \to \mu^+\mu^-$ decay embedded in a HYDJET event sample. The distribution of reconstructed muons is normalized by the number of generated muons with $|\eta| \leq 2.4$ and $p_T \geq 10$ GeV/c. The stand-alone muon efficiency is saturated at unity over all single muon pseudorapidity, single muon p_T, and event centrality phase space. The global muon reconstruction exhibits a flat distribution as a function of muon p_T with a slight dependence on the event centrality. The efficiency as a function of muon pseudorapidity shows a plateau in the barrel region ($|\eta| \leq 0.8$), decreasing with increasing muon pseudorapidity.

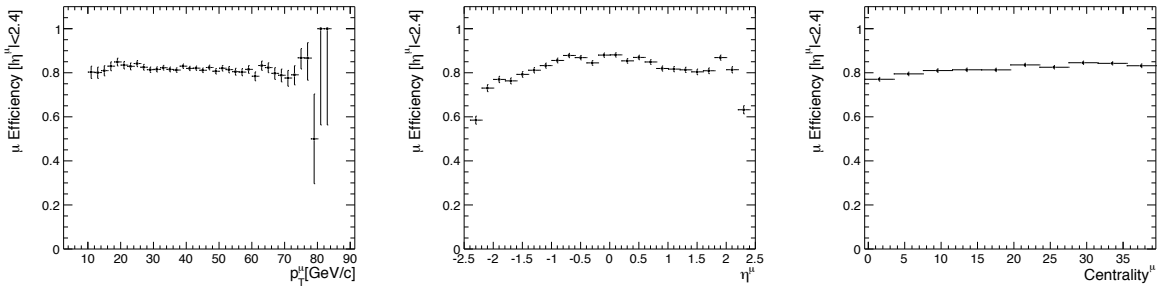

Figure 4.8: Single global muon reconstruction efficiency from $Z^0 \to \mu^+\mu^-$ embedded in minbias HYDJET as a function of, p_T (left), pseudorapidity (center) and centrality bin (right)

The overall reconstruction of a muon trajectory can be seen in Fig. 4.9, where the solid

blue line is indicative of a global muon. The red line indicates the trajectory of an electron reconstructed in the tracker. A charged hadron (green line) leaves a signal in the tracker and deposits its energy in the HCAL. A neutral hadron is identified by the energy deposited in the HCAL without a trajectory in the inner tracker, indicated by the green dashed line. Finally, a photon leaves no signal in the tracker and deposits its energy in the ECAL.

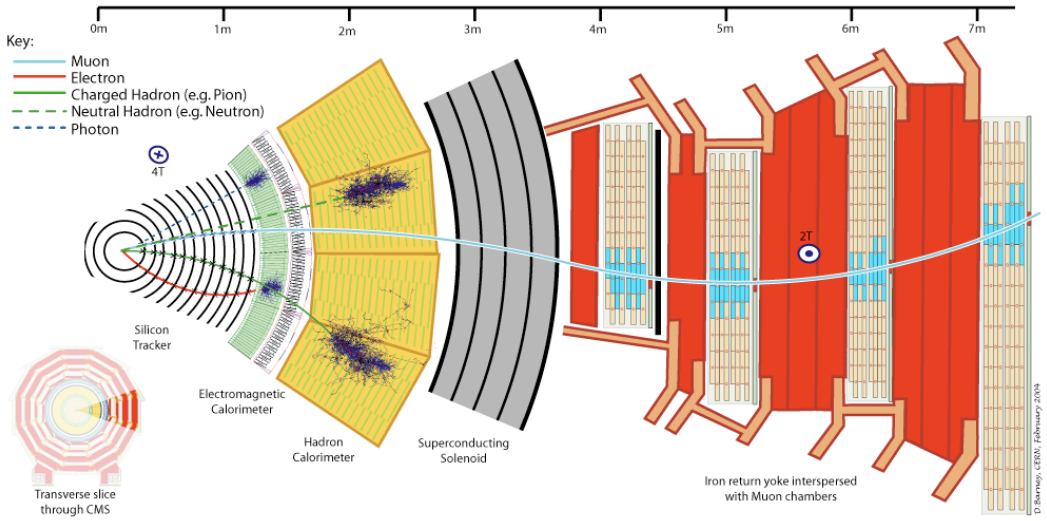

Figure 4.9: CMS slice showing the trajectories of a muon, an electron, a charged hadron, a neutral hadron and a photon

Dimuons

The reconstruction of Z^0 decays is done by requiring two opposite-charge global muons in the event. Each muon must pass a series of quality cuts. Furthermore, an additional constraint is imposed on the muon pair to beat down random background that might fake two muons. The vertex probability test evaluates the compatibility of two tracks to originate from the same vertex. The vertex probability is calculated using the χ^2 and the number of degrees of freedom of the vertex. The calculated probability is that of an observed χ^2 which exceeds the value χ^2 of the track fit by chance [66].

4.3 MC truth matching

In order to estimate the the performance of the reconstruction algorithms and perform readout studies it is important to have a handle on the generated information. The simulation step directly precedes the reconstruction step. The sim hits are used as seeds to start the reconstruction algorithms. Once the entire reconstruction chain has been executed, the information can be compared with the simulated data put in. In high multiplicity events many tracks can be close together in $\eta - \phi$ space and have similar tranverse momenta which makes it very difficult to associate tracks based solely on kinematics. A better approach is to unambiguously match the reconstructed object to the simulated object, and vice-versa, on a hit-by-hit basis.

4.3.1 Muon association by hits

The Muon Association By Hits (MABH) is a package that is used to do the aforementioned hit-by-hit comparison between reconstructed and simulated objects. The idea is to take the 3D location of the reconstructed hits that make up the reconstructed object and compare them with the 3D location of the simulated hits from the simulated track. With this information one makes a one-to-one map between sim and reco objects. In order to calculate efficiencies each simulated track is compared with the collection of reconstructed tracks. If a simulated track is found to have a match in the reco collection it is considered to be successfully reconstructed. A reco-to-sim approach is generally used to perform fake rate studies. The MABH can associate global muons in a modular fashion, allowing one to characterize the silicon tracker reconstruction and the stand-alone muon reconstruction separately.

Matching criteria

The criterion for a successful match depends on what percentage of hits are matched between the reco and sim object. The quality of the match is given in a range from 0 to 1. A quality of 1 means that all the hits in the simulated track were found to have a match in the reconstructed object. A quality of zero implies that the specific simu-

lated track does not share any hits with a given reconstructed track. This criterion can be evaluated separately for the 'tracker' part and the 'muon' of a global muon, both quality levels are set to 0.75 or higher. The advantage of requiring that each part meets the 75% criteria as opposed to an overall 75% approach is that the former requirement also ensures that the tracker track is properly reconstructed.

4.4 Tag-and-Probe

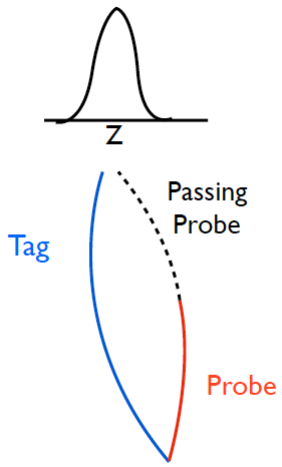

Figure 4.10: Tag and probe diagram with Z^0 mass resonance

`Tag-and-probe` is a data driven technique to calculate efficiencies with a "modular" approach. One of the main advantages of the `tag-and-probe` method is to avoid large systematic errors due to imperfections in modeling the data and the detector response. This is done by measuring the efficiency from the data itself with no reference to simulation. This method utilizes known mass resonances (e.g. J/ψ, Υ, Z^0) to select particles of the desired type and probe the efficiency of a particular selection criterion on those particles [67]. The `tag` is an object that passes a set of very tight selection criteria designed to isolate the required particle type (in this case a muon). The fake rate for passing tag selection criteria should be very small ($\ll$1%). A generic set of the desired particle types known as *probes* is selected by pairing with the `tags` such that the invariant mass of the combination is consistent with the mass of the resonance. Combinatoric backgrounds can be subtracted

by a fit or a sideband subtraction. The definition of `probe` depends on the specifics of the selection criterion being examined. The efficiency is measured by counting the number of `probe` particles that pass the desired selection criteria :

$$\epsilon = \frac{N_{\text{passing probes}}}{N_{\text{all probes}}} \tag{4.7}$$

where $N_{\text{passing probes}}$ is the number of probes that pass the selection criteria and $N_{\text{all probes}}$ is the total number of probes counted using the resonance. Figure 4.10 shows a simplified diagram of the `tag-and-probe` method. The `tag` (blue line) is selected with a tight selection criteria. A collection of `probes` with a looser criteria is selected. The `tag` gets paired with every `probe` and only the one that make the `Tag-Probe` pair add to mass of the resonance (Z^0 mass) will be considered. The efficiency is calculated from the ratio of how many `probes` satisfy the requirements to complete the black dashed line, divided by the number of all the `probes`.

The `tag-and-probe` method can be used to calculate different efficiencies depending on the definition assigned to the tags and probes. The efficiencies can be separated in a "modular" fashion to account for each of the steps needed to calculate an overall efficiency. In the case of the global muon reconstruction it can be divided into:

$$\epsilon_{\text{Global muon}} = \epsilon_{\text{tracker track}} \times \epsilon_{\text{matching}} \times \epsilon_{\text{muon track}} \tag{4.8}$$

where $\epsilon_{\text{tracker track}}$ is the efficiency for reconstructing the inner track of a muon, $\epsilon_{\text{muon track}}$ is the efficiency for reconstructing the outer part of the muon and $\epsilon_{\text{matching}}$ is the efficiency of matching an inner track with the muon track.

Chapter 5

Analysis Details

5.1 CMS heavy-ion setup

The high multiplicity environment produced in *PbPb* collisions, required the detector to adopt a setup optimized for such events. Some of the subsystems were required to make changes (with respect to the *pp* setup) in the readout schemes to accommodate the needs of various heavy-ion analyses. The main issues that were addressed were: data formats, firmware limitations, and level-1 (L1) triggering. In the pixels, the main modifications were done to the zero suppression algorithm and firmware. For the silicon strip detector, a different zero suppression algorithm was used and data were collected in the virgin raw mode. Selective readout schemes were also implemented for the ECAL. The muon system does not present such a big increase in the occupancy compared to *pp* collisions. However, the L1 configuration for the CSC was adjusted to cope with a higher fake rate.

5.1.1 Readout

During preparation for the heavy-ion run, some concerns regarding the readout strategy for the CSC were addressed. The forward muon chambers present a higher activity in the *PbPb*, environment as can be seen in Fig. 4.1. This activity is due to the large number of hadrons that make it to the first chambers with enough p_T to penetrate only a few layers. Most of these particles hit the forward-most chambers, ME1/1, and do not make it to the next layer. The large number of punch-throughs has a direct impact in the number of

level-1 triggers coming from the CSCs. The CSC track finder (CSCTF) is an algorithm that is in charge of connecting track segments into a full track (Sec. 4.2.4) and assign a p_T, η and ϕ value to it [55], achieving a 25% p_T resolution [68]. At the time of pp running, the configuration for the CSCTF required a muon trigger candidate to have at least one segment, also known as 'singles'. This configuration was optimized to trigger on low-p_T forward muons for the b-physics analyses. This loose criterion, used to trigger on muon stubs, would have resulted in a very high rate of CSCTF triggers in heavy-ion collisions. In order to reduce the rate of punch-throughs, the 'singles' requirement was removed. Instead, a 'coincidence' requirement was implemented, requiring different chambers to have hits consistent with coming from the same track to satisfy the CSC track finder.

Given the data sizes expected in the most central collisions, the data flow in the CSCs was under review to detect possible bottlenecks. Estimates made with MC samples indicate that, with an expected minimum-bias event rate on the order of $\approx$ 100 Hz, the data sizes were calculated to be well under the maximum limit restricted by the front end boards (FEBs). A direct comparison of the estimates of the data volume generated by the number of `recHits` and segments for minimum-bias events in pp collisions at $\sqrt{s}$= 7 TeV and $PbPb$ collisions at $\sqrt{s_{NN}}$ = 2.76 TeV is shown in Figs. 5.1 and 5.2.

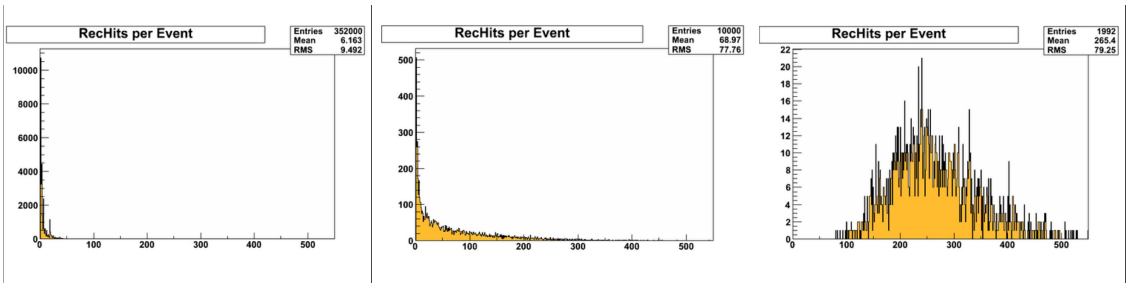

Figure 5.1: Comparison of `recHit` multiplicity for minimum-bias pp (left), minimum-bias $PbPb$ (center) and central $PbPb$ events (right).

The mean increase in `recHits` and segment multiplicity in the CSCs is about a factor of 3-4 when comparing minimum-bias pp and $PbPb$ events. However, the mean multiplicity for central (b=0) $PbPb$ events is significantly higher. Central events are rare. Furthermore, even at the high multiplicity tail of the distribution, the data volume is well

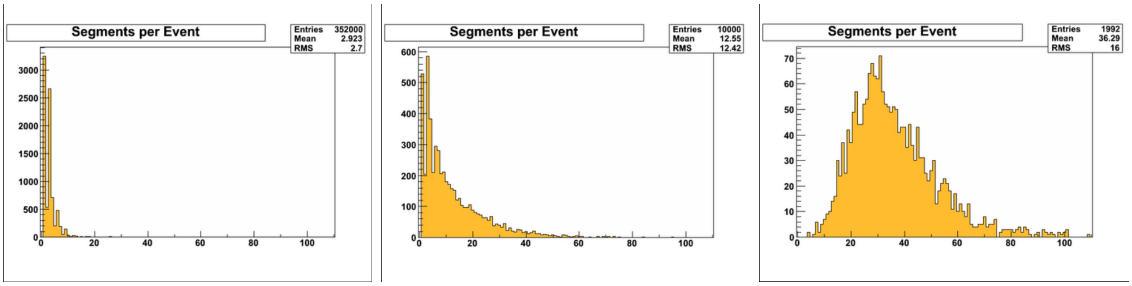

Figure 5.2: Comparison segment multiplicity for minimum-bias *pp* (left), minimum-bias *PbPb* (center) and central *PbPb* events (right).

under the maximum alloted by the front end electronics. Therefore, it was deemed safe to continue with the current, at the time, CSC readout scheme for the 2010 heavy-ion run.

5.2 Heavy-ion collisions

The November-December 2010 PbPb run was the first heavy-ion run at the LHC. The constantly-evolving conditions of the accelerator meant that the CMS detector had to be prepared for different trigger scenarios. The continuous increase in the instantaneous luminosity translates into an increase in the rate of data being recorderd to tape. This can be seen in Fig 5.3. The number of bunches delivered by the accelerator increased from $1\times$ 1 to 129 $\times$ 129. The total number of triggered minimum-bias events was N_{MB} = 53 584 437. The minimum-bias trigger was based on the transverse energy, E_T, measured in the HF calorimeters. The minimum-bias trigger efficiency, ϵ_{MB}, was calculated using a simulation of the response of the HF in HYDJET events, was 97$\pm$ 3% [63]. This resulted in 55 241 688 delivered minimum-bias events after correcting for trigger efficiency [5]. The trigger efficiency was cross-checked with a technique based on the number of good pixel hits. Further details are given in Sec. 5.2.2. The total integrated luminosity delivered was $\mathcal{L} = 7.2\ \mu\mathrm{b}^{-1}$ assuming $\sigma_{\mathrm{PbPb}} = 7.65$ b.

5.2.1 Data flow schemes

In order to optimize the resources and the availability of the data for analysis, a multi-stream strategy was devised. The data was divided into 3 different streams, a Data

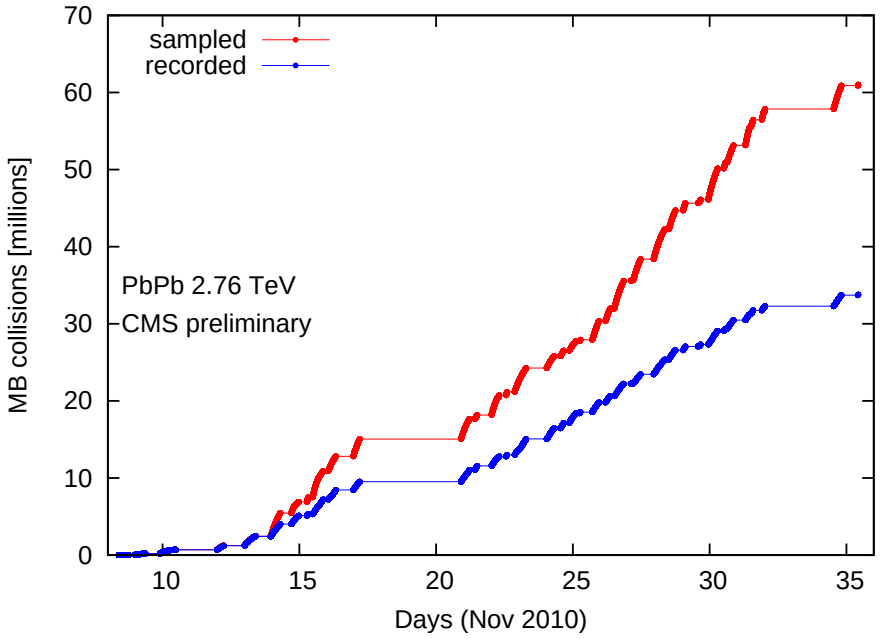

Figure 5.3: Total number of equivalent minimum-bias, sampled (in red) and recorded (in blue) by CMS.

Quality Monitor (DQM) stream, a minimum-bias stream and Physics-Analysis stream. All these streams had a different purpose. The DQM stream is the smallest of the three and it was used to feed the DQM framework in order to validate and monitor the data as it was flowing from the detector. The requirement of this data was to have a quick turnaround time and to take a small fraction of the bandwidth. The minimum-bias stream was the one occupying the largest fraction of the bandwidth. This sample contained the main minimum-bias trigger selection with some pre-scales as necessary. This stream, being the largest one of the three, had the largest delay due to reconstruction. Its main purpose was to be used for longer time-scale analyses. The third stream was designed to have a so-called *core physics* selection. This stream was fed by triggered data, such as the dimuon triggers used for this work. It was set up to be promptly reconstructed and analyzed. It started from a minimum-bias selection, followed by specific physics analyses triggers. The configuration to build the *core physics* stream was designed to maximize the number of useful events for analysis while keeping the bandwidth to the allocated fraction. This was a challenging task

as the instantaneous luminosity delivered by the LHC changed on a daily basis.

5.2.2 Triggering

The CMS detector has different ways to trigger on events, making use of the different subsystems. The main objective is to distinguish the activity captured by the detector coming from collisions to the one coming from noise, cosmics, beam background and other non-collision related activity. The sequence implemented to suppress non-collision activity starts from a minimum-bias L1 trigger selection. This is followed by a specific sequence of physics-related triggers. For this analysis the sequence included single and double muon triggers. The minimum-bias and muon trigger are executed *online*, that is, as the event data is being readout the trigger system makes a decision to either keep or reject the event. After triggering, *offline*, a series of event selection cuts are applied. Finally, specific quality cuts were implemented at the analysis level.

Minimum-Bias Trigger

The minimum-bias trigger used information from the HF and BSC. The minimum-bias trigger relied only on the BSC up to run 150593 (inclusive). The trigger required coincidence, that is, that the detectors should have activity on both sides. In addition, a bunch crossing identified by the BPTX was required. The coincidence requirements on the BSCs were set to look for at least one segment to fire on each side, dubbed 'threshold-1'. The BSCs have 16 segments on each side (32 total), of which 31 were operational. Most (75%) of the collisions illuminate all 31 segments, thus making the effect of one dead segment negligible [69]. After run 150093, the minimum-bias trigger incorporated information from the HF as an "OR" operator. The HF trigger required at least two towers that had deposited energy exceeding the firmware threshold. Compared to the BSC trigger, the HF trigger was also noise-free, but offered a better efficiency to identify minimum-bias collisions. In addition, the HF trigger offered a better overlap with the offline event selection. The combination of the two trigger bits provided a robust and more reliable net to "catch" hadronic *PbPb* collisions. Having the HF requirement as an "OR" with the BSC coincidence provided a measure of redundancy in case any hardware problems presented

themselves.

Muon Triggers

The triggering system is organized in levels where each provides a selection to further reduce the data volume. Trigger candidates passing the level-1 (L1) stage move on to the level-2 (L2) trigger and to level-3 (L3), the latter two composing the High Level Trigger(HLT). The level-1 trigger analyzes every bunch crossing. The L1 trigger decisions are made by programable hardware electronics, while the HLT is a software system implemented in a farm of about a thousand processors using reconstruction software similar to one used in the offline analysis. A series of single muon triggers can be deployed depending on p_T threshold and quality of the triggered muon. The level-1 muon trigger makes use of the CSC, DT and RPC sub-detectors. The DT and CSC electronics first process the information from each chamber locally. A position and angle per muon station is delivered for every muon that crosses a station. Vectors from different stations are combined to form a muon track and to assign a transverse momentum value. The RPCs deliver their own track candidates based on regional hit patterns. The information from the three subsystems is combined, achieving an improved momentum resolution and efficiency. The four highest-p_T muons from each sub-system are selected for further processing. Finally, the muon p_T thresholds are applied [55]. The L1 muons serve as seeds for the L2 muons. The L2 algorithm reconstructs hits from the muon sub-systems and constructs tracks using the Kalman Filter technique [70]. The resulting trajectories are used to refine the resolution of the measured muon kinematics.

Various L1 triggers were used during the 2010 heavy-ion run. These included triggers which selected muon with p_T thresholds at 3, 5, 15 and 20 GeV/c. The L2 p_T thresholds were 3, 5, and 20 GeV/c.

Dimuon Triggers

Dimuon triggers are also implemented at different levels of the triggering system. For this analysis, two dimuon triggers were used. One used L1 muons, and simply required the presence of two in one event, regardless of their p_T. No RPC information was required.

These events were dubbed `L1DoubleMuOpen`. A second trigger used L2 muons, requiring the presence of two in one event, with the additional condition that each had $p_T \geq 3$ GeV/c. The RPC information was used in this case. These events were dubbed `L2DoubleMu3`.

The low luminosity at the beginning of the heavy-ion run allowed for less restrictive triggers. The double muon trigger `L1DoubleMuOpen` requires that two muons leave a signal read by the muon hardware systems. This makes it a very efficient algorithm and also very susceptible to background noise and punch-throughs, because hadrons can have just enough energy to trigger the muon hardware systems. As the performance of the accelerator improved, the instantaneous luminosity increased, requiring a more restrictive double muon trigger to fit in the allotted readout bandwidth. The `L2DoubleMu3` trigger is more selective than the `L1DoubleMuOpen` in three respects. It implements the L2 muon algorithm which makes use of local muon reconstruction similar to the stand-alone muons described in Sec. 4.2.4, This allows for a better resolution of the kinematic parameters to be achieved. This trigger requires coincidence in the muon trajectories found by the DT and CSC with the trajectories found by the RPC. Since the data obtained from this trigger sample was mainly used for the $Z^0 \to \mu^+\mu^-$ analysis, a p_T threshold of 3 GeV/c was also used to keep the readout volume under control. This cut has a negligible acceptance effect for muons coming from a Z^0 decay.

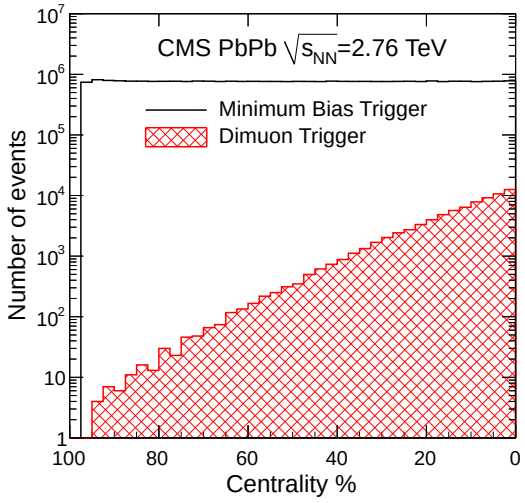

Figure 5.4: Centrality distribution for minimum-bias and dimuon-triggered events.

Figure 5.4 shows the centrality distribution of events that fired the minbias trigger (black histogram). The fraction of the hadronic cross section is integrated starting from the most central (b≈0) events. The bin widths are constructed to contain equal fractions of the total hadronic cross sections, resulting in a flat shape in the figure. The `DoubleMuOpen` triggered event distribution (red, hashed histogram) shows that the majority of these events come from the most central collisions, since the main dimuon sources in the CMS acceptance scale with the number of hard collisions.

Dimuon Trigger Efficiencies

The trigger efficiencies were obtained with a data-driven method known as `tag-and-probe`, see Sec. 4.4. Figures 5.5 and 5.6 show the trigger efficiency for the `L1DoubleMuOpen` and `L2DoubleMu3`, respectively. The efficiencies were calculated using different samples to estimate the systematic uncertainty and check for consistency. The `L1DoubleMuOpen` trigger efficiencies were obtained from a $Z^0 \rightarrow \mu^+\mu^-$ event embedded in a HYDJET minbias sample (red squares) and also embedded in a minbias selection of HI data (blue triangles). The efficiency is shown as a function of muon η (with a $p_T \geq 10$ GeV/c selection) and muon transverse momentum. The efficiency of this trigger is very close to unity and shows a flat distribution in the full η acceptance and for $10 \leq p_T \leq 80$ GeV/c. After run 150593 the trigger setup was changed to `L2DoubleMu3`. This trigger shows a slightly lower efficiency than `L1DoubleMuOpen` trigger. The same features are observed as a function of muon η. As function of p_T the efficiency shows a turn-on curve that saturates at $\approx 98\%$ after 10 GeV/c. The trigger efficiency obtained using the data-driven `tag-and-probe` method is also shown by black squares while the single-muon-triggered data are shown as open circles.

As seen in Fig. 5.6, the efficiency obtained from single-muon-triggered data (open circles) is lower in the p_T range from 10-20 GeV/c compared to the distributions obtained in the other samples. The single-muon-triggered data efficiency was calculated by obtaining the ratio between reconstructed muons matched to the `L2DoubleMu3` trigger primitives divided by all the reconstructed muons with high quality cuts shown in Table 5.1. Most of the muons that populate this distribution are in the lower p_T range [10- 20 GeV/c]. However, the muons from a Z^0 decays have a higher p_T, where there is a better agreement in the

results across the four different samples. For the purpose of this analysis, the difference in efficiencies will not be considered as a systematic error. Instead only the error on the `tag-and-probe` method will be used. This is done in order to obtain the uncertainty limitation directly from data, as opposed to relying on MC.

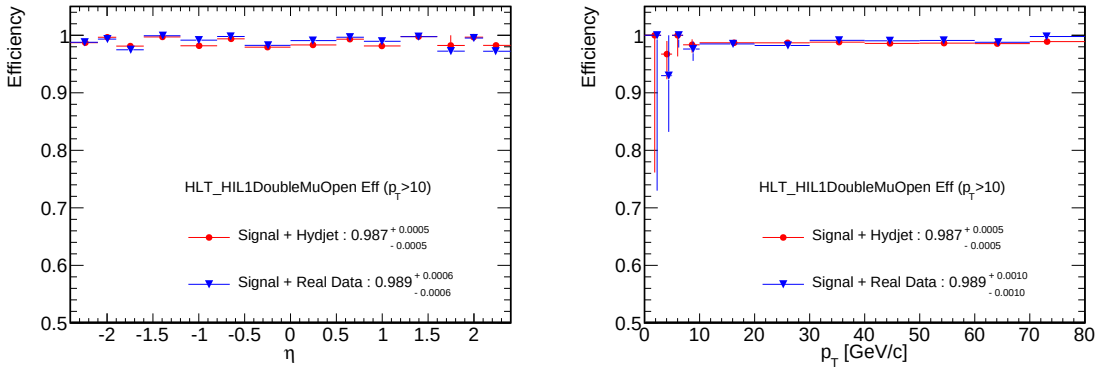

Figure 5.5: The efficiency for single muons from a L1 dimuon trigger as a function of muon η (left) and p_T (right). The efficiencies are obtained from a signal embedded in HYDJET (red) and in HI data (blue)

In order to calculate the trigger efficiencies using the `tag-and-probe` method the following definitions were used.

- `Tag`: A global muon, matched to a single muon trigger with a p_T threshold of 20 GeV/c.
- `Probe`: A global muon passing the quality cuts, to ensure a well defined *probe*.
- `Passing probe`: A probe that is matched to either the `L1DoubleMuOpen` or `L2DoubleMu3`, depending the stage of the run.

To avoid introducing a trigger bias, the sample was first filtered on the single muon trigger that is matched to the L2-single muon trigger with a 20 GeV/c p_T threshold. To obtain a pool of events that sample only the trigger efficiency. The efficiency on real data for single muons is obtained by the ratio of reconstructed muons matched to the `L2SingleMu3` (single muon trigger) over all the reconstructed muons with high quality cuts (see Table 5.1).

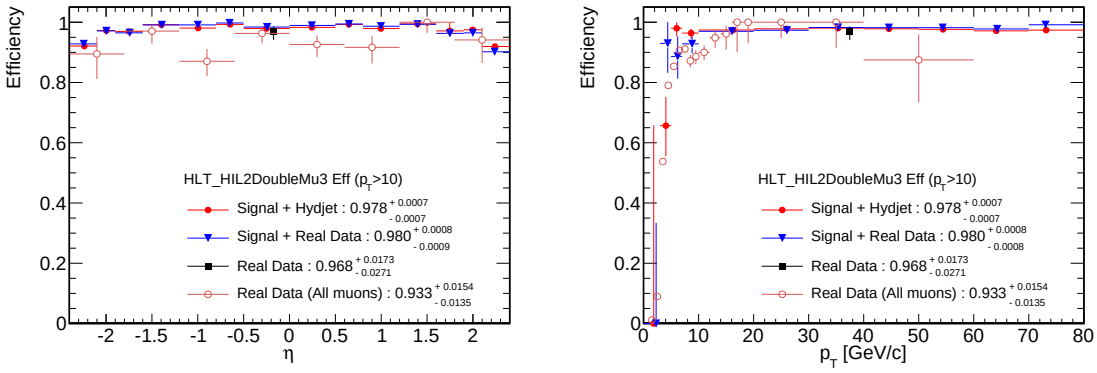

Figure 5.6: *Tag-and-probe* efficiency for single muons from a L2 dimuon trigger as a function of muon η (left) and p_T (right). Efficiencies obtained from: signal embedded in HYDJET (red) and signal embedded in HI data (blue), dimuon triggered data (black) and single muon triggered data (open red circles)

The cut `TrackerMuonArbitrated` refers to the requirement of that track to be considered a tracker muon after resolving the ambiguity of shared segments. A 'tracker muon' is an inner track that is matched to at least one segment reconstructed in the muon chambers. The `TMLastStationAngTight` cut is also a tracker muon requirement that applies position and pull cuts to the segment match in the deepest required station [71].

5.2.3 Offline event selection

The *good event* qualification was assigned to events that passed the minimum-bias trigger requirement and also satisfied a set of offline cuts. The offline event selection was implemented to clean up triggers coming from cosmics, beam-halos, background, beam-gas events and ultra-peripheral collisions (UPC). The cuts are the following:

- BSC halo-filter: Events in which any of the BSC halo triggers bits fired were excluded. The BSC halo trigger requires coincidence on both sides. This means that at least one hit on each side, in any segment within 40 ns (timed for a muon moving at the speed of light) would fire the trigger. This is intended to exclude muons consistent with having a trajectory that crosses the detector from one side to the other. Figure 5.7 shows the correlation between the number of hits in the first pixel layer and the total

Table 5.1: Quality cuts applied to global muons for trigger efficiency. Variables described in Sec 5.2.4

cut	Value Applied
`isTrackerMuon`	`true`
`isGlobalMuon`	`true`
`N. of valid hit in the inner track`	≥ 11
`N. of valid hit in the muon stations`	≥ 1
$\chi^2_{\text{global}}/\text{ndf}$	$\leq 10.$
$\chi^2_{\text{inner}}/\text{ndf}$	$\leq 4.$
d_{xy}(vertex)	≤ 0.2 mm
d_z(vertex)	≤ 14 mm
`pixel layers with measurement`	≥ 1
`TrackerMuonArbitrated`	`true`
`TMLastStationAngTight`	`true`

HF energy. The events from collisions (black) show good correlation between the two quantities. The events triggering the BSC beam halo bits (red) have small energy deposits in the HF and large activity in the pixel layers [69].

- A two-track primary vertex requirement was imposed. In peripheral events, all tracks with $p_T > 75$ MeV/c were used to reconstruct the vertex. In central events, the minimum p_T was increased to keep the maximum number of fitted tracks stable around 40-60, ensuring time-efficient reconstruction.

- To remove 'monster' events, a requirement of pixel cluster-length compatible with the vertex was implemented. 'Monster' events refer to high multiplicity events that originate from not-well-defined sources, other that a collision inside the detector. Figure 5.7 shows events (blue) in which HF deposit are much smaller than for any *PbPb* collisions. Those events are mostly eliminated by a cluster compatibility cut (defined below). Some are eliminated by the BSC cut alone but they are all eliminated by the

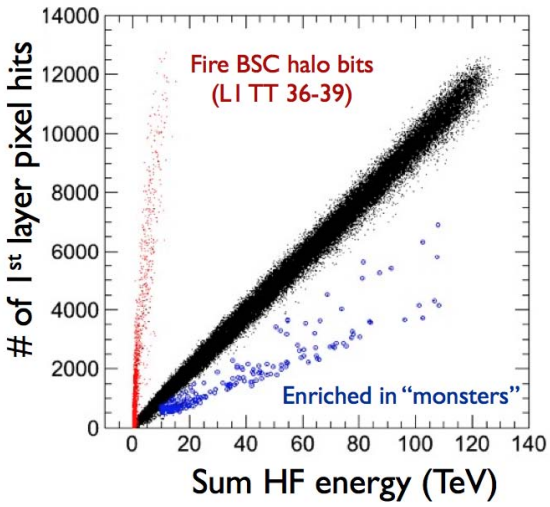

Figure 5.7: Correlation of between sum HF energy and 1st pixel layer activity for *good event* (black), BSC triggers (red) and 'monster' events (blue)

combination of both cuts. Figure 5.8 shows the cut implemented to exclude 'monster' events, these events fall below the red line. The compatibility variable is the number of clusters that have a length that is compatible with the reconstructed vertex, divided by the number of hits that are compatible with an artificially displaced vertex (offset $\pm$ 10 cm). If the ratio is high, that indicates a well-defined vertex and a valid collision. If the ratio is close to unity, this indicates that the vertex is ill-defined, characteristic of 'monster' events. At very low pixel multiplicity, the compatibility is allowed to be low, in order to keep events that have a little larger background hit fluctuation but otherwise good collisions. Figure 5.8 shows the relation between cluster-vertex compatibility and the number of pixel hits, used to define a 'good event'. The line shows the value of the cut being applied.

- An offline requirement of HF coincidence requiring at least 3 towers on each side of the interaction point with at least 3 GeV of total deposited energy in the HF.

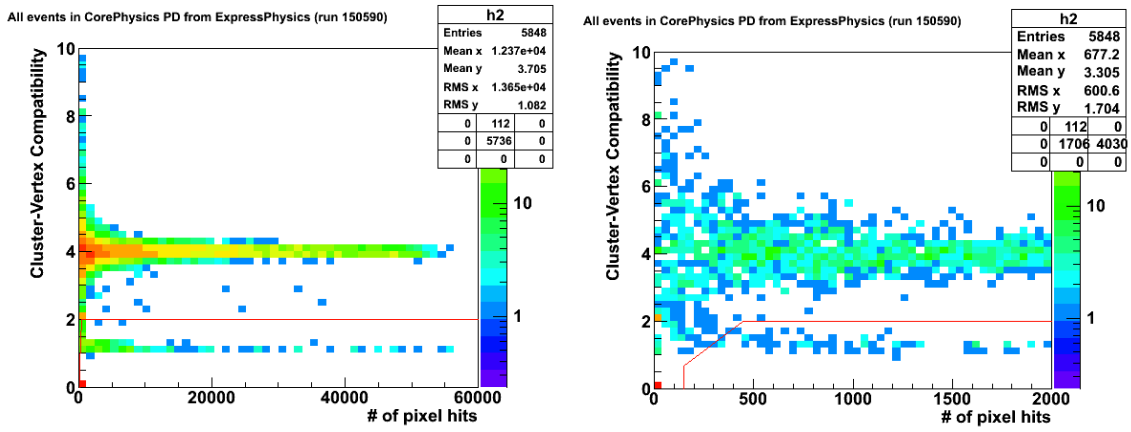

Figure 5.8: 'Monster' event cut, excludes events below the red line. Cluster-vertex compatibility (y-axis) against the number of pixel hits (x-axis).

5.2.4 Signal Extraction

The main objective of the signal extraction is to keep as many of the $Z^0 \rightarrow \mu^+\mu^-$ events while suppressing the background. In order to improve the signal-to-noise ratio it is important to know the parameters that can help remove some of the background without adversely affecting the signal. A series of quality cuts are applied to ensure that the information provided by reconstructed object is reliable. Some of the cuts have become standard within analyses that rely on muon reconstruction and/or use the heavy-ion tracking sequence. Given that the analysis relies on the proper identification of high-p_T muons, the main goal is to ensure that the global muon objects pass the basic quality standards. By virtue of the CMS design, not many punch-through hadrons make it to the outer muon chambers, resulting on a fake muon. However the can make the muon reconstruction, noisy. Cosmic muons can also 'fake' a collision muon. To ensure an unbiased selection of the cut parameters and their values, a cut analysis exercise was performed before taking a look at the data. Each of the quality cuts are summarized in the following section.

Quality cuts

In order to study the effects of each of the cuts on the variables, five different distributions were plotted in Figs 5.9 - 5.14. Reconstructed muons from MC ($Z^0 \rightarrow \mu^+\mu^-$ embedded in HYDJET events) were overlaid with reconstructed muons from HI data on the same canvas. Each distribution is defined as:

- Muons from Z^0: A set of reconstructed global muons that were traced back to a generated muon which came from a Z^0 decay (Gray histogram).
- Punch-throughs: A set of reconstructed global muons that traced back to anything other than a muon after the GEANT simulation (Red-hashed histogram).
- Other Muons: A set of reconstructed global muons that traced back to a muon but do not originate (at any level) from a Z^0 (Blue hashed histogram).
- Muons from `HIData`: A set of reconstructed global muons from real collisions, after passing quality cuts (Green triangles).
- Muon from `Zcand`: A set of reconstructed global muons that come from the Z^0 candidates in collisions (Red stars).

All the distributions have been normalized to match the integral area of the muons that come from Z^0 candidates (red stars). In the embedding process, as detailed in section 4.1.1, the $Z^0 \rightarrow \mu^+\mu^-$ events were generated with flat p_T and rapidity distribution. In order to show a "realistic" profile of each of the variables, a re-weigthing procedure was applied in rapidity and transverse momenta. The flat distributions were weighted according to the shapes generated with PYTHIA. The dashed red vertical lines indicate the value of the quality cut used for that variable. In all cases, the five distributions are plotted after all the quality cuts have been applied, except for the one that is being profiled.

Some of the cuts implemented were selected taking into account the physical acceptance of the CMS detector. The pseudorapidity coverage of the muon chambers is $\pm$ 2.4 units, thus reconstructed muons beyond those limits were not considered. Muons coming from Z^0 (MC or HI data) have a nearly flat distribution as a function of η, whereas muons

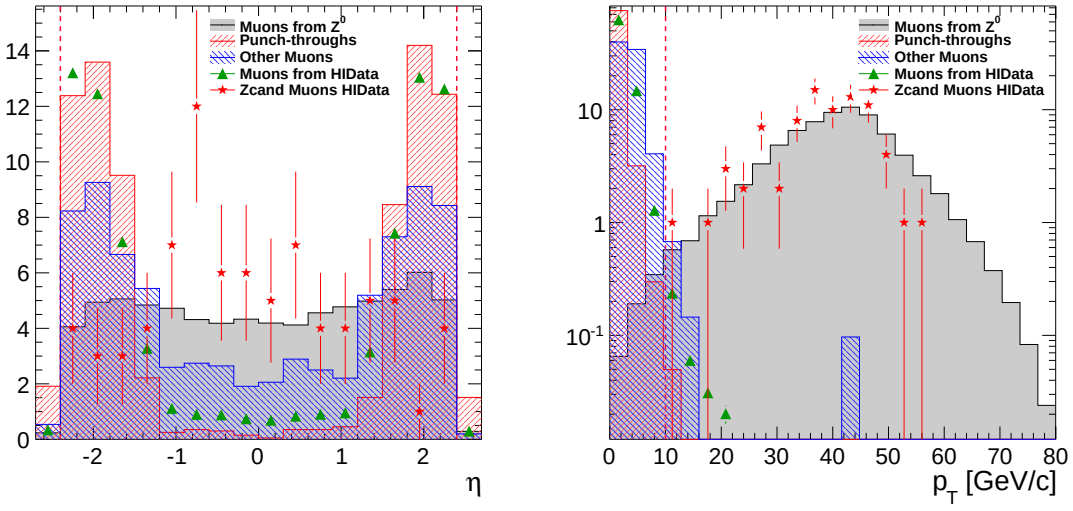

Figure 5.9: η and $p_T$distribution of reconstructed muons form HI data and MC (see text for description)

from in-flight decays or punch-through favor the forward direction. This is because the p_T requirement to be reconstructed in the barrel is higher than in the endcaps. Figure 5.9 (left) shows the η distributions of the five sets. The p_T distribution is shown on the right-hand side. The cut at 10 GeV/c applied for the analysis has a negligible effect on the muons from simulated Z^0 decays (gray histogram) and does not cut any of the muons from the Z^0 candidates. It is worth noting the impact of this cut on eliminating reconstructed muons that do not come from Z^0 decays. This cut was set to reduce the systematic error at the expense of losing 1% of the generated Z^0 ,since the turn-on curves of the triggers are safely under this value.

In order to better constrain muons originating from the collision, the distance between the reconstructed primary vertex and the closest point of the reconstructed trajectory is measured in the transverse plane (d_{xy}) and in the longitudinal plane (d_z). Figure 5.10 shows that the implemented cuts are very loose and do not affect the signal while cutting a small portion of the background. One of the characteristics of muons from a Z^0 decay is that the p_T is considerably higher than the muons from the underlying event. These high-p_T muon tracks have an improved pointing accuracy to the interaction point.

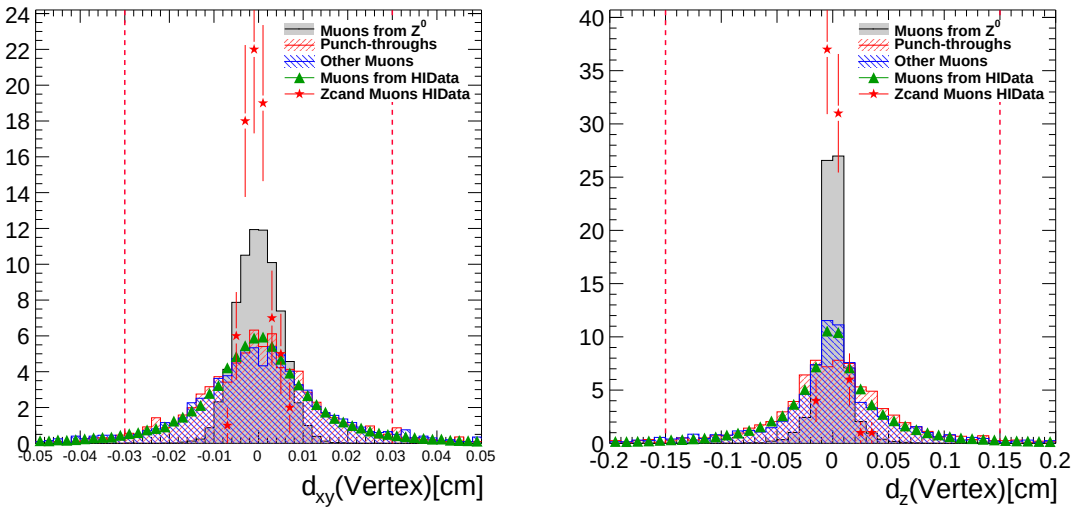

Figure 5.10: d_{xy} and d_z distribution of reconstructed from HI data muons and MC (see text for description)

For a reliable reconstruction, a goodness of fit is calculated at different levels of the reconstruction and properly normalized by the number of degrees of freedom. The χ^2_{inner}/dof is the normalized χ^2 distribution for the inner track that used to match to a muon detected by the muon chambers and form a global muon. The χ^2_{global}/dof is the normalized χ^2 distribution for the overall fit of the global muon. It is a powerful tool to reject both decay-in-flight and punch-throughs [72]. In both cases the applied cuts are very loose, as seen in Fig. 5.11.

The number of hits has an impact on the quality of the reconstruction. Figure 5.12 shows the distribution of the number of hits used for the reconstruction of the inner tracker track (left) that forms the global muon (right) and the number of hits used in the overall fit of the global muon. The number of hits in the tracker-track part of the global muon is ≥ 10 hits. Generally, tracks with smaller number of hits give a bad p_T estimate. In-flight decays give rise to lower hit occupancy in these tracks, since the track does not originate in the innermost layers. The requirement for the global muon is set to more than 1 "valid" hit. This requirement ensures that the global muon is not a bad match between the spatial and momentum information from the muon system and tracker. It is clear that this is one

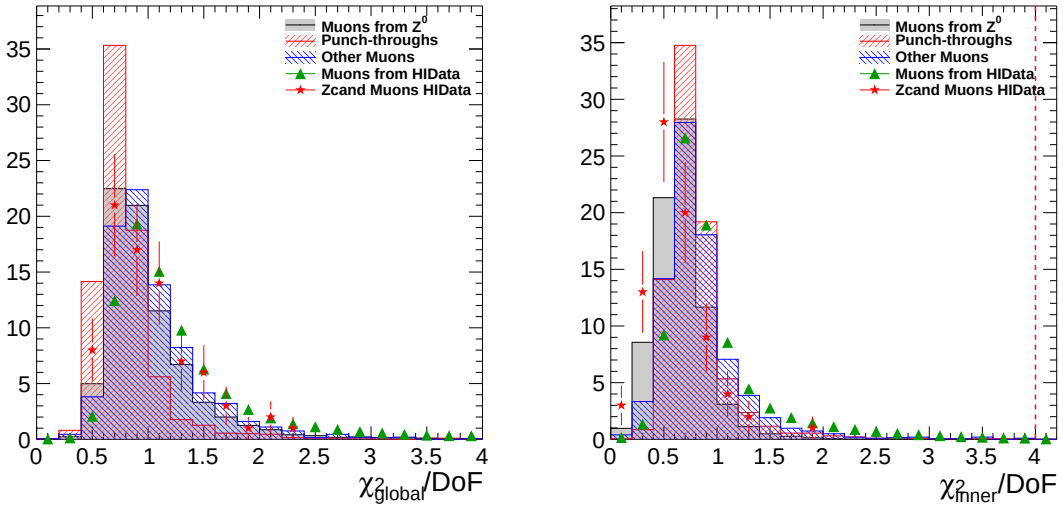

Figure 5.11: Inner χ^2 and global χ^2 distribution of reconstructed muons from HI data and MC (see text for description)

of the more effective cuts to eliminate of punch-throughs. s

Figure 5.13 shows the distribution of the number of pixel hits coming from the inner track (left) and the number of segments matched to the outer part of the global muon track (right). The innermost part of the tracker is an important for discarding non-prompt muons. By asking for a minimal number of pixel hits, we ensure that the track originates at least within the pixel detector geometry. The number of matched segments from the muon chambers to the global muon track is also shown in Fig. 5.13 (right). The larger the number of segments matched to the track, the more information from the local reconstruction (from each of the sub detectors) is used. This is an effective way to chose global fits using a substantial amount of information from the chambers themselves.

Figure 5.14 shows the boolean variable `isTrackerMuon` and the relative error of the reconstructed p_T. The `isTrackerMuon` variable refers to the quality of the global muon to also fulfill the requirements to be considered a *tracker muon*. A 'tracker muon' is a well reconstructed inner-track that is matched to at least one segment reconstructed in the muon chambers. This is an effective cut against in-flight decays, punch-throughs and accidental matching (with noisy background tracks or segments). The panel on the left shows the

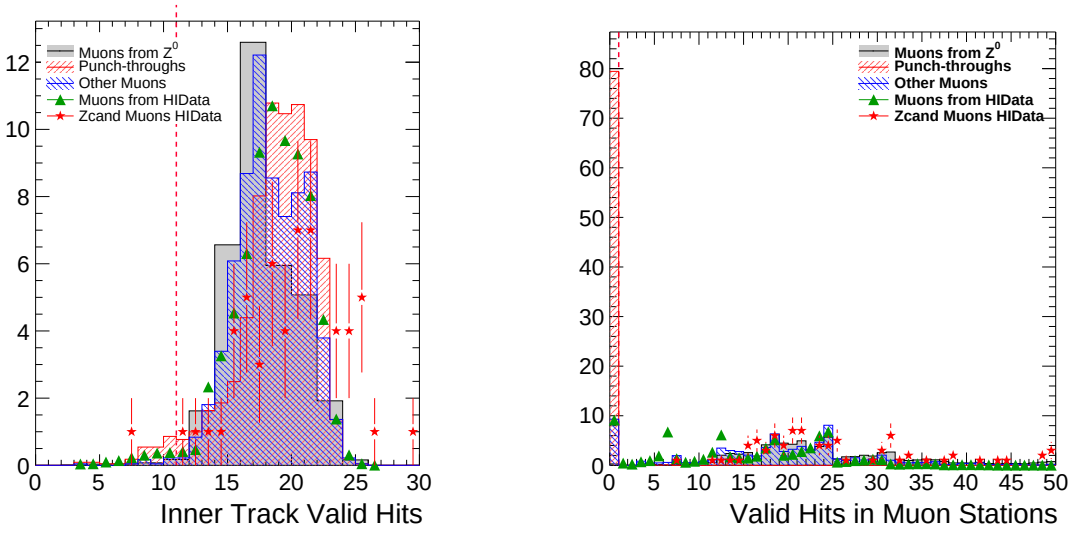

Figure 5.12: Inner track and global muon hits distribution of reconstructed muons from HI data and MC (see text for description)

relative error of the reconstructed p_T. For global muons, the p_T assignment is obtained from the inner track (up to 100 GeV/c). This cut simply removes those muons with a bad p_T assignment.

The quality cuts that were implemented on the muon global fit are in accord with recommendations from the Muon object group [73, 72] and follow the spirit of the cuts used in previous Z^0 measurements in pp collisions with the CMS experiment [74] where applicable. There is an overall agreement between the muon distributions coming from MC Z^0 decays and the muons coming from Z^0 candidates in the heavy-ion data.

Table 5.2 summarizes the value of each of the cuts in the second column. The third column shows the impact of each individual cut on the MC sample defined in Sec. 4.1.1. The percentage shown in the third column is the fraction of the sample kept when a specific cut is applied by itself. The fourth column shows the fraction of muons coming from a Z^0 decay that is kept when all other cuts are applied while the specific cut is excluded. It can be seen that none of the cuts introduce inefficiencies greater than 1%. The overall efficiency after applying all the quality cuts is estimated to 97.58%.

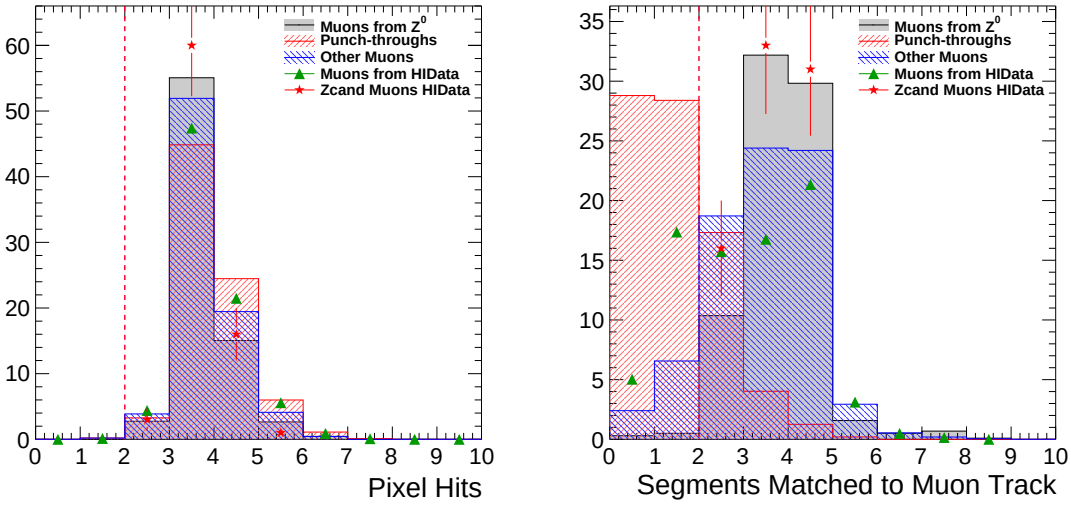

Figure 5.13: Pixel hits and matched muon segments distribution of reconstructed muons from HI data and MC (see text for description)

5.2.5 Z^0 Acceptance

Acceptance can be defined as the fraction of produced events which are measurable by the detector out of the total number of generated events within a given phase space region. In this light, the acceptance is dependent on the phase space spanned by the generated Z^0's, which will eventually decay into muons, and also on the kinematics that the daughters will need in order to be *detectable*. A *Detectable* muon must have sufficient p_T to reach the muon chambers and must leave a certain number of reconstructible hits in the sensitive areas of the muon chambers. Furthermore, the muons must be reconstructed with opposite-sign charges and with a a pair invariant mass from 60 to 120 GeV/c^2. The CMS detector has a coverage of $|\eta|$ <2.4 for muons. The muon p_T acceptance has an η dependence, but for the purposes of this analysis was set at a constant of 10 GeV/c, with full ϕ coverage. To generate the Z^0 decays, a PYTHIA [75] simulation at $\sqrt{s_{NN}}$ =2.76 GeV with the CTEQ6L1 PDFs [76] is employed. Figure 5.16 shows the Z^0 acceptance as a function of rapidity (y) and transverse momentum. The acceptance as a function of p_T is a constant of $\approx$ 77.7 $\pm$ 2% in the range for $\leq$ 50 GeV/c [5]. The acceptance as a function of p_T is maximal in the mid rapidity region, decreasing in the forward region. This implies that 77.7 $\pm$ 2% of the

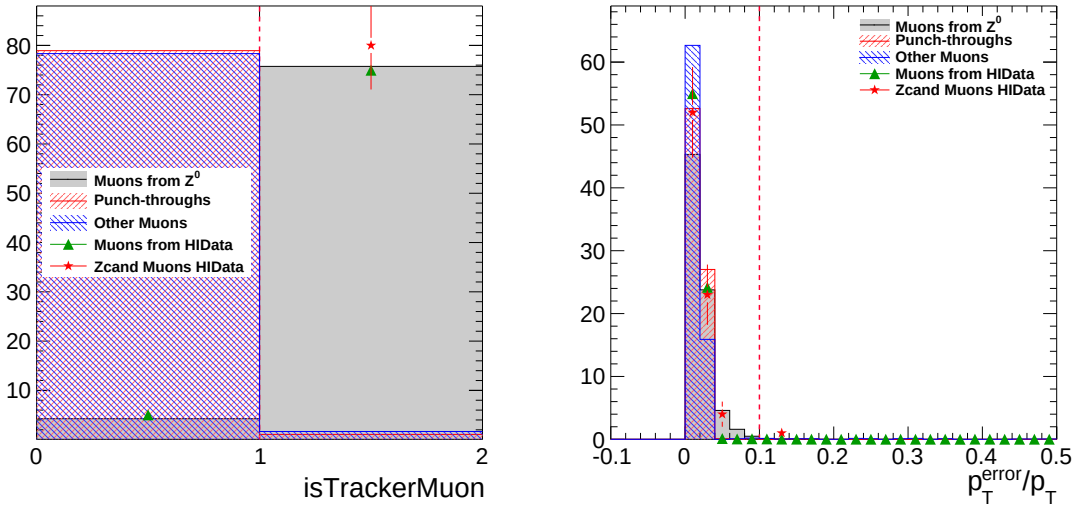

Figure 5.14: Tracker Muon requirement and p_T^{error}/p_T distribution of reconstructed muons from HI data and MC (see text for description)

Z^0 decays produced by our generator can indeed be reconstructed by the CMS detector.

5.2.6 Z^0 Acceptance $\times$ Efficiency

For the purpose of this analysis, it is more useful to calculate the combined acceptance and efficiency. The product of these two represents the fraction of Z^0 events successfully reconstructed with respect to the total number produced. One of the advantages of using the combined acceptance and efficiency, is that there is no risk of overcompensating for a missing event or completely ignoring some events that may fall between the definitions of acceptance and efficiency. For the calculation of `Acceptance` $\times$ `Efficiency` the PYTHIA gun sample embedded in minimum-bias real events described in section 4.1.4 was applied. In this sample, the Z^0 is generated with flat distributions in rapidity and transverse momentum. Thus, the `Acceptance` $\times$ `Efficiency` corrections will need to be readjusted with weights accounting for the realistic Z^0 rapidity and p_T distributions. The shapes of the weights are obtained from PYTHIA. This weighting procedure is also implimented to correct for the use of a minimum-bias event sample for the generated $Z^0 \rightarrow \mu^+\mu^-$ events, instead of one that reflects the hard collisions as shown in Fig. 5.4.

Table 5.2: Quality cuts applied to global muons

	Value Applied	Only this cut	All except this cut
$\|\eta\|$	< 2.4		
p_T	≥ 10 GeV/c	99.00%	98.47%
χ^2_{inner}/ndf	$\leq 4.$	99.98%	97.58%
χ^2_{global}/ndf	$\leq 10.$	99.69%	97.82%
d_{xy}(vertex)	≤ 0.3 mm	99.93%	97.59%
d_z(vertex)	≤ 1.5 mm	99.94%	97.59%
`Valid hits`$_{\texttt{inner track}}$	≥ 11	99.62%	97.90%
`Valid hits`$_{\texttt{muon stations}}$	≥ 1	99.72%	97.83%
`isTrackerMuon`	`true`	99.54%	97.94%
p_T^{error}/p^T	≤ 0.1	99.77%	97.70%
All cuts applied	97.58%		

The MABH tool described in Sec. 4.3.1 was used to calculate the `Acceptance` × `Efficiency`. This allows us to trace back (to the generator level) each of the single muons that make up the dimuon candidate in the mass range 60 - 120 GeV/c^2. The following definitions were used:

- Dimuons in our acceptance (defined in Sec 5.2.5) and successfully reconstructed in the mass range 60 - 120 GeV/c^2 are defined as having two opposite charged global muons with $p_T \geq 10$ GeV/c and $|\eta| \leq 2.4$ they both pass the muon quality cuts. In order to match a reconstructed muon with a simulated muon, a 75% hit sharing criterion was used, Sec 4.3.1.

- The normalization of the efficiency factor (denominator) is a dimuon in the mass range 60 - 120 GeV/c^2 and $|y| \leq 2.4$.

The corrections obtained from the `Acceptance` × `Efficiency` method were applied on a bin-by-bin basis as a function of dimuon rapidity and event centrality with the proper

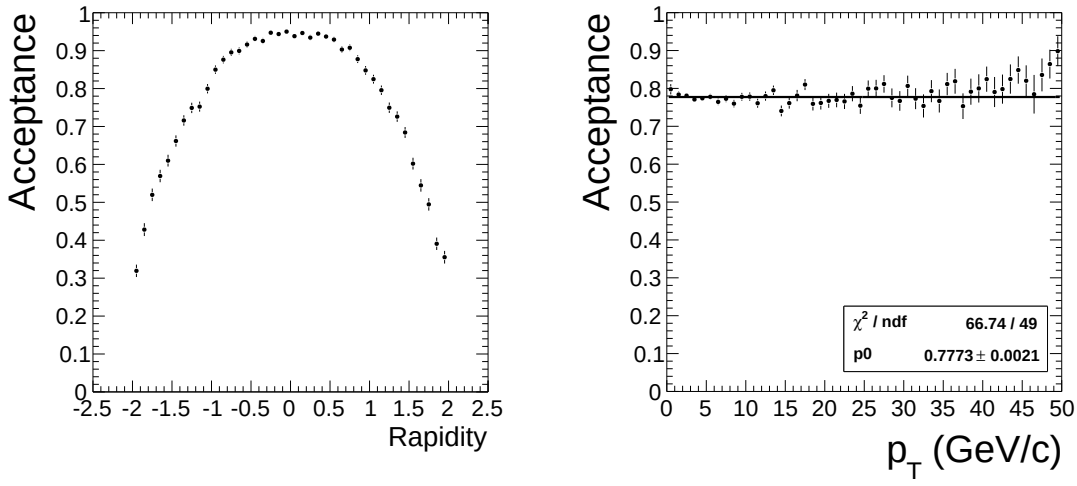

Figure 5.15: $Z^0 \to \mu^+\mu^-$ acceptance for each of the muons in $|\eta| < 2.4$ and $p_T > 10$ GeV/c as a function of Z^0 rapidity and transverse momentum [5]

weights to account for the realitic distributions described in Eq. 5.1. The middle panel of Fig. 5.16 shows a flat distribution of `Acceptance` × `Efficiency` and p_T. The `Acceptance` × `Efficiency` ($\alpha \times \varepsilon$) is flat as a function of Z^0 p_T, hence the p_T dependence is factored out of average value in Eq 5.1

$$\alpha \times \varepsilon_{avg} = \frac{\sum_{y \text{ bins}} \sum_{\text{cent bins}} \alpha \times \varepsilon(y, cent) \times \omega_{\text{PYTHIA}}(y) \times N_{\text{coll}}(\text{cent})}{\sum_{y \text{ bins}} \sum_{\text{cent bins}} \omega_{\text{PYTHIA}}(y) \times N_{\text{coll}}(\text{cent})} \tag{5.1}$$

In figure 5.16 a result obtained from "peak method" is also shown as a cross check. This is the method used in Ref. [5]. A good agreement is reached between the two approaches.

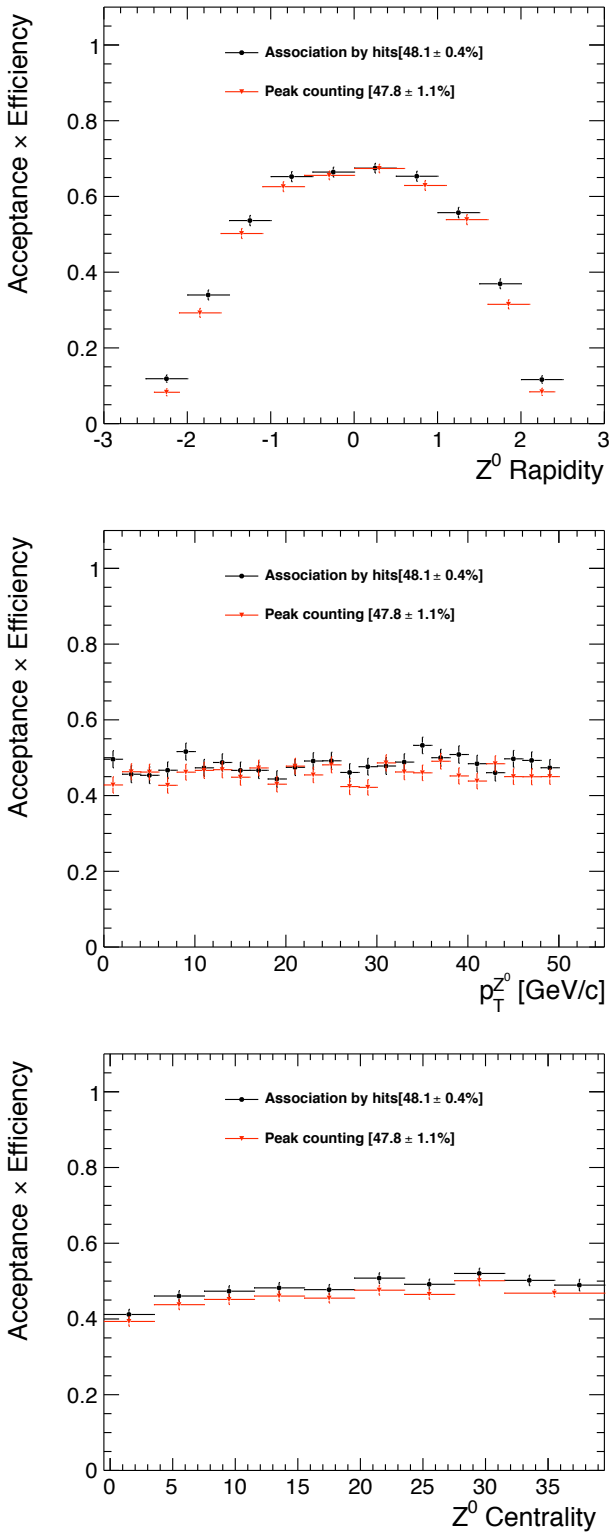

Figure 5.16: `Acceptance` × `Efficiency` as a function of rapidity, transverse momentum and centrality.

Chapter 6

Results and Discussion

In this chapter the $Z^0 \rightarrow \mu^+\mu^-$ measurement is presented as a function of rapidity, transverse momentum, and number of participants. The nuclear modification factor with respect to pp collisions at $\sqrt{s} = 2.76$ TeV is also presented.

6.1 The $PbPb$ analysis sample

The first $Z^0 \rightarrow \mu^+\mu^-$ event in $PbPb$ collisions recorded by CMS came in run 150590 on Nov. 9th, 2010 shown in Fig. 6.1. The event display shows the activity in the inner tracker represented by the yellow tracks that populate the innermost region of the detector. The high multiplicity expected from heavy-ion collisions is clearly visible. The towers activated in the electromagnetic calorimeter are shown in red while the towers in blue are from activity in the hadron calorimeter. Most of the activity in the ECAL and HCAL is in the forward region. The purple towers are the Hadronic forward calorimeters, used to trigger minimum-bias collisions and calculate the event centrality. The two reconstructed global muons are shown as black tracks. The first muon [η = 0.38, ϕ = -1.98 rad, p_T = 33.80 GeV/c] is reconstructed in the barrel region and the DT chambers, with segments belonging to the track shown in gray. The second muon [η = -2.28, ϕ = 0.71 rad, p_T = 29.41 GeV/c] is in the forward region with the CSC chambers also in gray. The outline of the detector can be seen in the background in a faint red and blue tone.

With an integrated luminosity of $\mathcal{L} = 7.2\ \mu\text{b}^{-1}$, a total of 39 dimuons were found

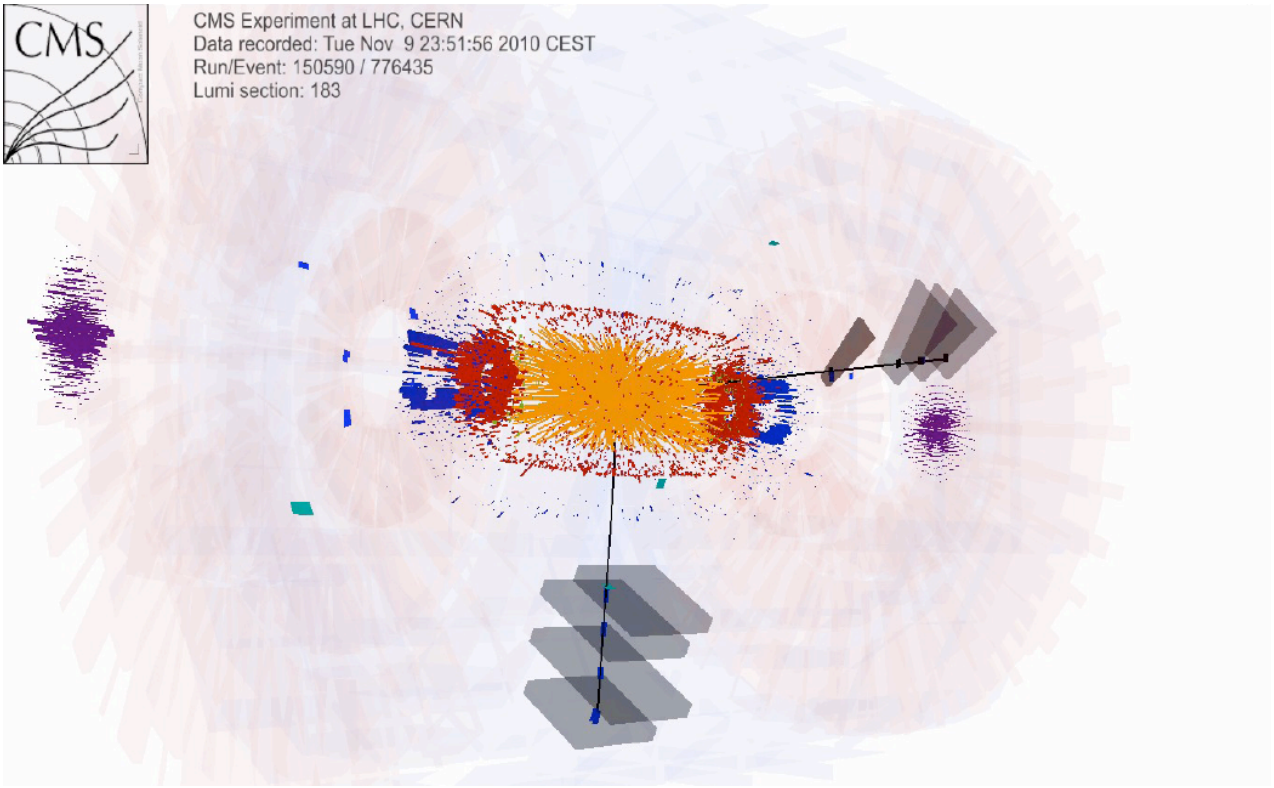

Figure 6.1: First $Z^0 \rightarrow \mu^+\mu^-$ candidate event in PbPb collisions in the CMS detector

after applying the quality cuts outlined in Table 5.2 and requiring two muons with opposite charge in the mass range 60-120 GeV/c^2. Figure 6.2 shows the invariant mass of the Z^0 candidate pairs (blue squares), as well as the only same-sign pair (red open circle) that passed the quality cuts in the range 30-120 GeV/c^2. It is easy to see the clear signal the emerges almost background-free. In the range 30-50 GeV/c^2 there is some structure due to the continuum from other physics processes, mainly $b\bar{b}$ production. A black histogram from the CMS $Z^0 \rightarrow \mu^+\mu^-$ measurement in pp collisions at $\sqrt{s} = 7$ TeV [77] is also shown. The pp measurement employed similar kinematic cuts. The pp invariant mass histogram has been scaled to match the integral obtained from the $PbPb$ data. The detector performance is comparable between $PbPb$ and pp collisions.

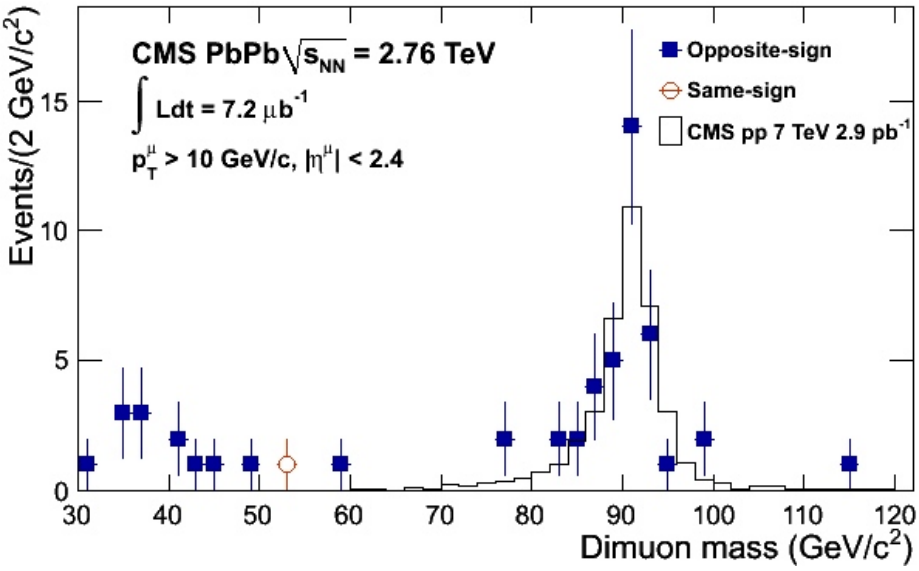

Figure 6.2: Invariant mass distribution of Z^0 candidates in PbPb collisions at $\sqrt{s_{NN}} = 2.76$ TeV

6.1.1 Mass fits

Due to the size of the data sample and lack of background for 60 $\leq$ M $\leq$ 120 GeV/c^2, this analysis can be carried out by counting the events that make up the invariant mass peak. However, it is still interesting to compare these events to relevant fits. Figure 6.3 shows the Z^0-candidate muon pairs in blue markers overlaid with different fits. The solid green line is a fit to the data using a Breit-Wigner (BW) [78] functional form,

$$f(E) \propto \frac{k}{(E^2 - M_Z^2)^2 + M_Z^2\Gamma_Z^2} \tag{6.1}$$

where the width of the Z^0, Γ_Z is fixed to the Particle Data Group (PDG) value of 2.49 GeV/c^2 and is related to the mean lifetime by $\tau = 1/\Gamma_Z$ (in natural units). The amplitude is given by the parameter k, which is allowed to vary in the fits. The parameter M_Z is the pole of the distribution which represents the value of the Z^0 mass. The Breit-Wigner is a natural fit for resonances in particle physics without taking into account resolution effects. The BW exhibits a tail at the low mass end of the distribution due to radiative losses. A better approach to fit the reconstructed data is to account for smearing of the distribution

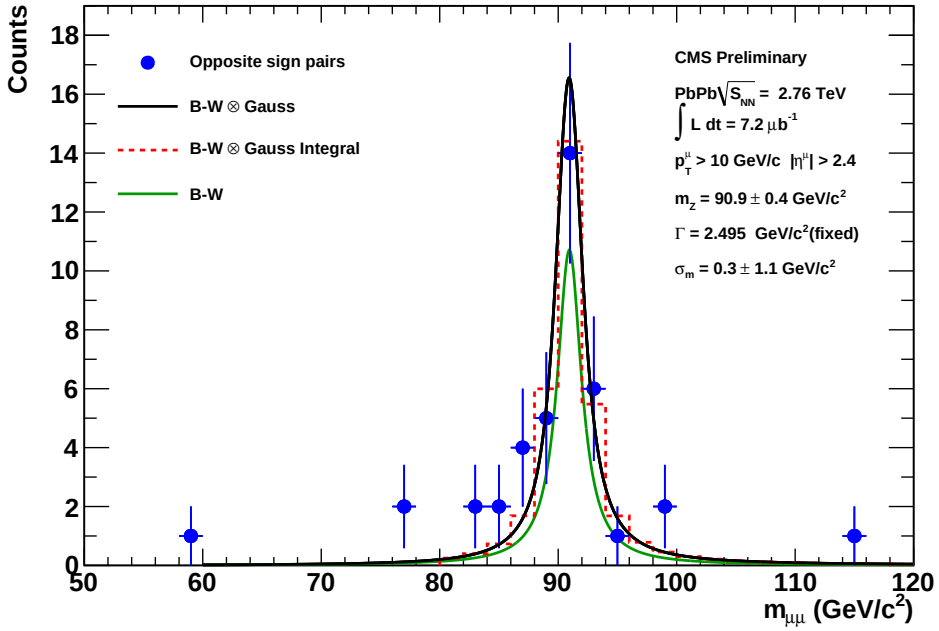

Figure 6.3: Invariant mass Z^0 candidates in $PbPb$ collisions at $\sqrt{s_{NN}} = 2.76$ TeV with fits, fit parameters listed for the BW convolved with a Gaussian

due to resolution effects. This can be accomplished by using a Breit-Wigner convolved with a Gaussian shape. An extra parameter is added with respect to the pure BW, σ_Z, the width of the Gaussian. Shown by the solid black line in Fig. 6.3. The dashed red line shows the bin integral version of the BW $\otimes$ Gaussian shape. The BW $\otimes$ Gaussian resembles the data more closely than the BW alone. The integral under the curve for the pure BW is $\sim$ 20 counts while the convolved BW $\otimes$ Gaussian yields $\sim$ 34 counts compared to the 39 muon pairs that are observed.

The parameters obtained from the fits are summarized in Table 6.1. In both fits the BW width was fixed to the PDG value. The rest of the parameters were obtained from the fits. The M_Z obtained from the BW fit is slightly lower than the PDG (91.1876 $\pm$ 0.0021 GeV/c^2 [2]) value, while the M_Z value from the BW $\otimes$ Gaussian fit is in agreement with the PDG.

Table 6.1: Fit parameters for Z^0 invariant mass peak.

Fit	Parameter	Symbol	Value
Breit-Wigner			
	Width	Γ_Z	2.495 GeV/c^2 (fixed PDG)
	Mean	M_Z	90.07 $\pm$0.43 GeV/c^2
	Integral		20
BW $\otimes$ Gauss			
	Natural Width	Γ_Z	2.495 GeV/c^2 (fixed PDG)
	Gaussian Width	σ_Z	0.3 $\pm$1.1 GeV/c^2
	Mean	M_Z	90.93 $\pm$ 0.37 GeV/c^2
	Integral		34

6.2 Systematic uncertainties

Minimum bias counting

The efficiency of the minimum-bias trigger was 97 $\pm$ 3%. This comes from the fact that not all the inelastic collisions lead to a triggered event. The uncertainty was evaluated varying the Glauber parameters in Ref. [63].

Background fitting

The statistical uncertainty that arises from the limited sample can be affected by contribution to the background in the 60 - 120 GeV/c^2. The main sources of backgrounds around the Z^0 pole can can originate from $W^{\pm}$ backgrounds, $Z \rightarrow \tau^+\tau^-$, muons from di-boson combinations ($W^{\pm}$, Z^0), $t\bar{t}$ decays and QCD multijet accompanied by a muon [77]. The contributions from all these sources add up to 3.7 parts per million. Electroweak backgrounds are not expected to be modified in the QGP. QCD backgrounds, however, should be modified by the QGP which can make the hadrons (that later decay into muons) lose energy as they traverses the medium. The main source of background that contributes to

the opposite-sign dimuon distribution come from semi-leptonic $b\bar{b}$ decays. The background $b\bar{b}$ is estimated to be a factor of 20 lower than the signal, even without assuming b-quark quenching [79]. To properly estimate the background that lies under the Z^0 mass peak the data are fit by an exponential in the mass range $35 \leq M_Z \leq 60$ GeV/c^2. The integral of the exponential in the Z^0 mass gives 1.48 counts while the measurement gives are 39 counts in the same mass region. The ratio of, background over signal, giving a 3.8% one-sided systematic uncertainty.

Quality cuts

In Table 5.2 we listed the sources of efficiency loss. The total efficiency after all the quality cuts have been applied is 97.6%. This is equivalent to the loss of a 1 Z^0 candidate. The systematic uncertainty introduced by the use of quality cuts is estimated to be 2.6%.

Acceptance

The fraction of events that fall within the defined acceptance depends on the choice of kinematic parameters used to generate the samples, as well as the number of contributing diagrams for such processes. Acceptance uncertainties derive from the choice of the kinematic distributions under two choices:

- choice of the Parton Distribution Function (PDF),
- difference between LO and NLO MC generators.

Systematic uncertainties were obtained by comparing distributions obtained using PYTHIA interfaced with two different PDFs, namely CTEQ6L1 and MRST2004LO with results from MC@NLO interfaced with CTEQ6L1 [80]. By comparing the sample generated with PYTHIA-CTEQ6L1 with the one generated with PYTHIA-MRST2004LO, the systematics with respect to the PDF choice are extracted. The comparison of PYTHIA-CTEQ6L1 with MC@NLO-CTEQ6L1 is used to obtain the systematic uncertainties related to the leading order calculation used by the generator. The comparison of PYTHIA-CTEQ6L1 with MC@NLO-CTEQ6L1 is done with a caveat, since CTEQ6L1 are LO PDFs. Figure 6.4 (left) shows the acceptance of the Z^0 boson as a function of p_T. The acceptance is defined by:

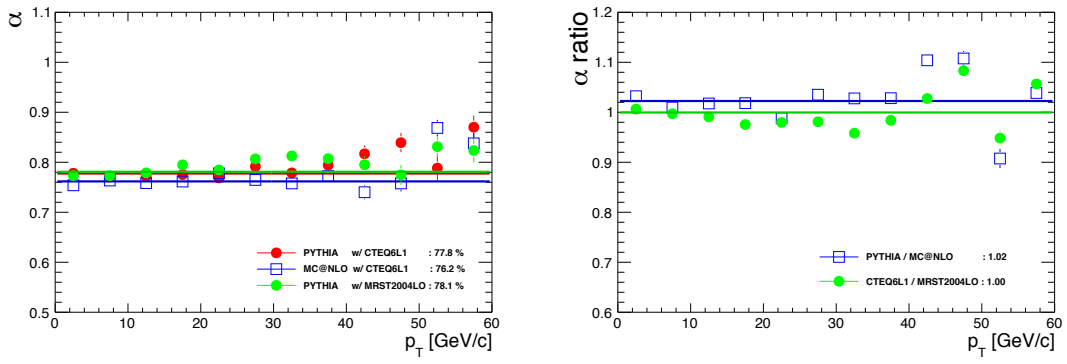

Figure 6.4: Left: Z^0 acceptance α versus p_T of the Z^0 : PYTHIA-CTEQ6L1 (red circles), PYTHIA-MRST2004LO (green full squares) and MC@NLO-CTEQ6L1 (open blue squares). Right: Acceptance ratios, for generator choice (blue open squares), and for PDF choice (green full squares) [5].

$$\alpha = \frac{N_z\ (|y^Z| < 2.0; p_T^\mu > 10\ \text{GeV}/c; |\eta^\mu| < 2.4; M_Z[\ 60 - 120\ \text{GeV}/c^2])}{N_z\ \ (|y^Z| < 2.0; M_Z[\ 60 - 120\ \text{GeV}/c^2])} \tag{6.2}$$

where the numerator is the number of Z^0's produced, within four units of rapidity, that decay into muons that can be reconstructed within a mass of $60 \leq M_Z \leq 120$ GeV/c^2. The denominator is the number of Z^0's generated in the same rapidity interval and mass range but without single muon cuts. The acceptance is approximately constant for the three generator-PDF configurations for $p_T \leq 35$ GeV/c. In all three cases the acceptance is ∼77%. Figure 6.4 (right) shows the ratios of the distributions on the left. The ratio of PYTHIA relative to MC@NLO is shown by the blue line. The ratio between the two different PDFs, CTEQ6L1 and MRST2004LO is given by the green line. The difference between the two results is less than ∼2%.

In order to be able to extrapolate our result for $|y^Z| \leq 2.0$; $p_T^\mu \geq 10$ GeV/c; $|\eta^\mu| \geq 2.4$ to the full entire phase space allowed for Z^0 production a total acceptance, α_{Total}.

$$\alpha_{\text{Total}} = \frac{N_Z\ (|y^Z| < 2.0; M_Z[\ 60 - 120\ \text{GeV}/c^2])}{N_Z\ \ (M_Z[\ 60 - 120\ \text{GeV}/c^2])} \tag{6.3}$$

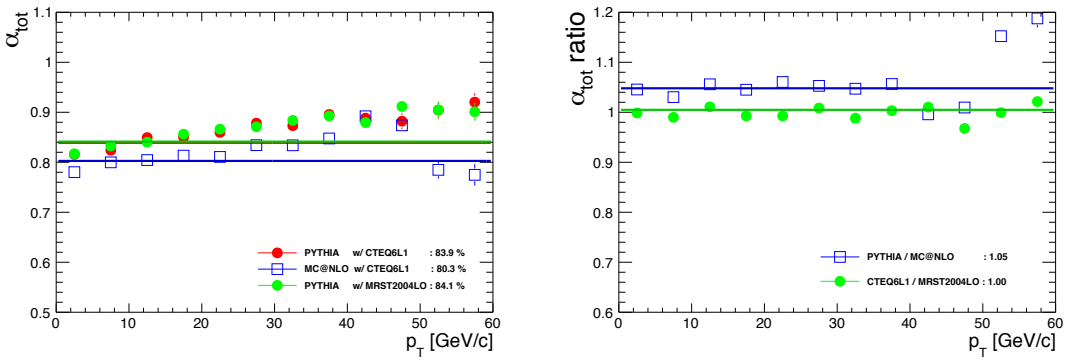

Figure 6.5: Left: Z^0 extrapolation to all rapidity $\alpha_{\rm tot}$ versus p_T of the Z^0 : PYTHIA-CTEQ6L1 (red circles), PYTHIA-MRST2004LO (green full squares) and MC@NLO-CTEQ6L1 (open blue square). Right: Acceptance ratios, for generator choice (blue open squares), and for PDF choice (green full squares) [5].

Figure 6.5 shows the acceptance of all Z^0 s in the range 60 $\leq M_Z \leq$ 120 GeV/c^2 that can be reconstructed in the $|y^Z| \leq 2.0$ phase space. The acceptance shows a slight increase with p_T. The average value is shown to guide the eye. The PYTHIA configurations interfaced with different PDFs show similar behavior. However, MC@NLO interfaced with CTEQ6L1 shows a smaller acceptance. The right side of Fig. 6.5 shows the ratio of the points on the left. The effect of interchanging the generator is larger than the effect due to PDF selection, estimated at 5%.

Table 6.2: Variations of the acceptance corrections due to generator-PDF choice [5].

Generator - PDF	α	α_{tot}
PYTHIA - CTEQ6L1	77.8%	83.9%
MC@NLO - CTEQ6L1	76.2%	80.3%
PYTHIA - MRST2004LO	78.1%	84.1%

The summary of the acceptance factors used to estimate the uncertainties is given in Table 6.2. The largest systematic uncertainty due to the generator-PDF choice is 1.9%

within the analysis acceptance. The systematic uncertainties due to the choice of generators and PDFs can also influence the shape of the `Acceptance` × `Efficiency` corrections. The overall corrections when comparing the different generator-PDF setups, the average of the difference between setups, are calculated to be less than 1% [79].

Isospin

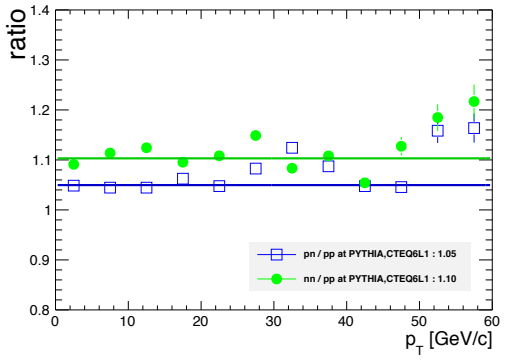

Figure 6.6: Ratios of the acceptance for pn/pp and nn/pp collsions, illustrating the systematic impact of isospin effects on the Z^0 acceptance [5].

Table 6.3: Variations of the acceptance corrections due to isospin effects.

Generator-PDF	α	α_{tot}
PYTHIA - CTEQ6L1 p+p	77.8%	83.9%
PYTHIA - CTEQ6L1 p+n	77.7%	83.8%
PYTHIA - CTEQ6L1 n+n	77.4%	83.4%

Another acceptance effect that has to be taken into account is due to isospin. This is because a $PbPb$ collision id indeed a collision system involving pp, pn, np and nn collisions, not just pp collisions. The contributions of the PDFs in these collisions as not identical to that of pp collisions. A comparison of the $p_T$acceptance from pn and nn collisions relative to pp collisions is shown in Fig 6.6 for PYTHIA-CTEQ6L1.The filled circles shows the ratio pp/nn while the empty squares show the pn/pp ratio. In both cases the ratios are close to

unity.

The summary of the acceptance factors due to isospin effects can be found in Table 6.3. The largest systematic uncertainty (from the difference between pp and nn collisions) is calculated to be 0.4%.

Shadowing and initial-state energy loss

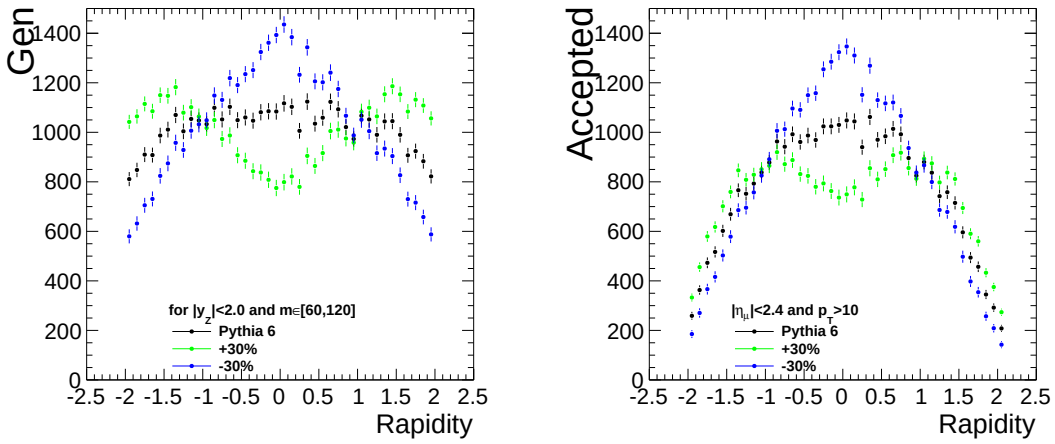

Figure 6.7: (Left panel) PYTHIA generated rapidity distribution (black), a +30% variation (green) and a -30% variation (blue) of the original shape. (Right panel) The rapidity distribution for the Z^0 that fall in the acceptance, for the same curves on the left [5].

According to theory predictions in Refs. [48, 49] shadowing and initial-state energy loss should modify the rapidity shape for the Z^0 . This also modifies the acceptance. The energy loss effect introduces a 3% modification, while shadowing is expected to have a 10-20 % impact. In order to properly account for the range of modifications at the acceptance level, artificial variations of the p_T and rapidity shapes were introduced. The rapidity shape of the Z^0 boson was varied by $\pm$ 30% in $|y^Z| \leq 2.0$ and the $p_T^Z \leq 50$ GeV/c^2. The artificial variation was choses to produce a maximal variance in the acceptance factor. The 30% variation is expected to encase the maximum expectations from theory predictions. To include isospin effects in these variations, the three types of collisions are considered (pp, nn, pn). All these effects are propagated through each of the collision configurations.

Figure 6.7 shows an example of the 30% variation done on the rapidity shape. The left panel shows the generated shapes: unmodified PYTHIA shape (black); the +30% variance (green); and -30% variance (blue). The right hand side shows the rapidity distribution as a function of accepted Z^0's for the three generated shapes from the left.

In order to properly incorporate the isospin corrections it is necessary to estimate an average acceptance that reflects the fraction of *pp*:*pn*:*np*:*nn* collisions such as:

$$\alpha_{\text{Isospin}} = \frac{82^2 \cdot \alpha_{pp} + 82 \cdot 126 \cdot \alpha_{pn} + 126 \cdot 82\alpha_{np} + 126^2 \cdot \alpha_{nn}}{82^2 + 2 \cdot 82 \cdot 126 + 126^2} \tag{6.4}$$

The acceptance is calculated in each kinematical bin of interest. The acceptance and its variations from the unmodified *pp* case, α default , +30% and -30% respectively are shown in Table 6.4. The average effect is calculated to be 3%.

Table 6.4: Acceptance and variation to account for shadowing and energy loss.

y	system	α default	α [+30%]	α [-30%]
$[-2;2]$	pp	77.8 ± 0.6	80.6 ± 0.6	75.0 ± 0.6
$[-2;2]$	pn	77.7 ± 0.6	80.5 ± 0.6	74.8 ± 0.6
$[-2;2]$	nn	77.4 ± 0.6	80.2 ± 0.6	74.5 ± 0.6
p_T	system	α default	α [+30%]	α [-30%]
$[0;50]$	pp	77.6 ± 0.6	78.1 ± 0.5	78.2 ± 0.7
$[0;50]$	pn	77.5 ± 0.6	77.9 ± 0.5	78.0 ± 0.7
$[0;50]$	nn	77.2 ± 0.6	77.6 ± 0.5	77.8 ± 0.7

Trigger

The systematic uncertainties due to the trigger efficiencies are calculated using the `tag-and-probe` method on real data. In Sec. 5.2.2 the `L2DoubleMu3` efficiency is estimated to be $0.968^{+0.017}_{-0.027}$. For simplicity, the uncertainties in the single muon efficiency are symmetrized to $\sim$ 2.2%. For a muon pair the uncertainty is doubled to $\sim$4.5%.

Reconstruction

The systematic uncertainties in the muon reconstruction are carried over from the data-driven pp analysis. The occupancy in the muon chambers, is comparable to that for pp collisions, is known at the 0.5% level [79]. Therefore, we use a similar uncertainty on the HI reconstruction, 1% for dimuons.

The tracking and matching part of the reconstruction efficiency is obtained from the `tag-and-probe` method in heavy-ion data using the following approach, illustrated in Fig. 4.10:

- `Tag` : A global muon, with a $p_T \geq$10 GeV/c and matched to the `L2SingleMu20` trigger object.
- `Probe`: A stand-alone muon.
- `Passing probe`: A probe that is matched to a global muon.

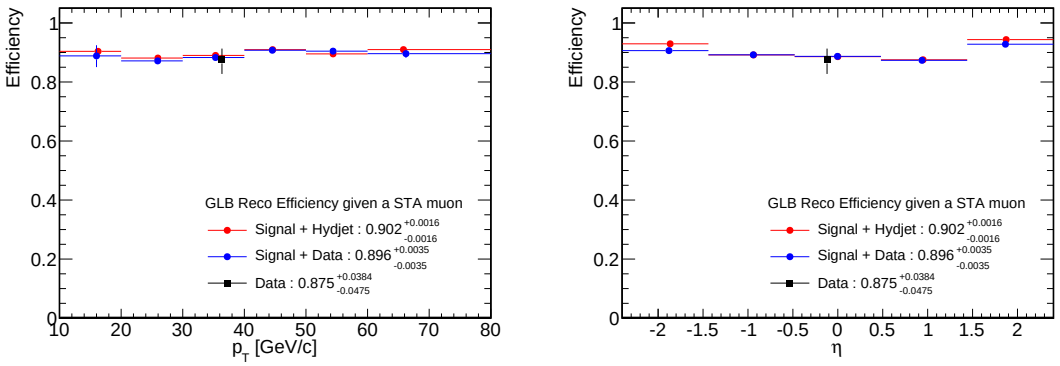

Figure 6.8: Single muon matching and tracking efficiency as a function of p_T (left) and η (right).

The single muon tracking efficiency is shown in Fig 6.8 as a function muon p_T and η. This efficiencies are calculated in MC heavy-ion events (Red) and HI data (Blue) with embedded $Z^0 \rightarrow \mu^+\mu^-$ events. The efficiency is also calculated in HI data (Black). The efficiency from data is $87.5^{+3.8}_{-4.7}$%. To calculate the systematic uncertainties the efficiency

from the `tag-and-probe` method is used since it has the advantage of being data driven. The total systematic uncertainty due to the tracking reconstruction is $^{+8.7\%}_{-10.7\%}$.

Other effects

Smaller corrections due to the differences between the embedded sample in real data and HYDJET are on the order of 1% [79]. Momentum scale and resolution corrections are dependent on the detector alignment and on the material present in it. These did not change with respect to the setup for the *pp* run, hence their systematic uncertainty is assumed to be 0.2%, as in Ref. [77].

All the systematic uncertainties discussed so far are summarized in Table 6.5. When they are added in quadrature we find a total systematic uncertainty of $^{+11.1\%}_{-13.3\%}$. The largest component is from the inner tracker reconstruction efficiency. The total systematic uncertainty is, however, still smaller than the statistical uncertainty of $(1/\sqrt{39})$ or 16% for this run.

6.3 *PbPb* Results

Table .9 shows some of the reconstructed variables of each of the 39 Z^0 candidates along with information on the daughter muons. The Z^0 distributions as a function of rapidity, transverse momentum and $N_{\rm part}$ can be extracted from this table.

6.3.1 Z^0 Rapidity

The $Z^0 \rightarrow \mu^+\mu^-$ differential yield as a function of rapidity is obtained in the window Δy=4.0,

$$\frac{dN}{dy}(|y| \leq 2.0) = \frac{N_Z}{\alpha\epsilon N_{\rm MB}\Delta y} \tag{6.5}$$

Out of a total of 55 $\times$ 10^6 minimum bias events and with 39 Z^0 candidates, $dN/dy = (33.8 \pm 5.5 \pm 4.4) \times 10^{-8}$. Figure 6.9 shows the rapidity distribution of the Z^0 candidates. The data is shown by the filled red circles for three rapidity bins: $|y| \leq 0.5$; $0.5 \leq |y| \leq 1.0$; and $1.0 \leq |y| \leq 2.0$. Systematic uncertainties are shown by the orange boxes while the statistical uncertainties are represented by the black bars. The theory results

Table 6.5: Systematic uncertainties

	uncertainty
Background fitting	- 3.8%
Quality cuts	± 2.6%
Acceptance	± 1.0%
Isospin	± 0.4%
Acceptance (Energy loss and shadowing)	± 3%
Trigger	± 4.5%
Muon reconstruction	± 1%
Tracking reconstruction	± +8.7%, -10.7%
MC simulation	± 1 %
Scale & Alignment	± 0.2%
Minbias counting	± 3%
Total	+11.1% -13.3%

include a POWHEG distribution interfaced with PYTHIA and scaled by $A^2/\sigma_{\mathrm{PbPb}}$ (black line). The model calculations discussed in here are per nucleon cross sections. To compare directly with our results, the model calculations are multiplied by $A^2/\sigma_{\mathrm{PbPb}}$. The results by Salgado and Paukkunen using the unmodified CT10 parameterization (green dotted line) [48] shows the difference that arises from isospin effects. They also included the EPS09 [81] shadowing parameterization (blue line with EPS09 systematic uncertainties given by the blue bands). The calculation by Neufeld and Vitev, using the MSTW08 parton distribution functions [50], also includes isospin effects (dotted brown line). Their calculation including energy loss effects is also shown (red-dashed line). Figure 6.9 shows the data follow a binary collision scaling, A^2/σ_{PbPb}, as do the models. This scaling indicates no modification induced by the hot medium. The experimental uncertainties do not allow to distinguish other smaller effects.

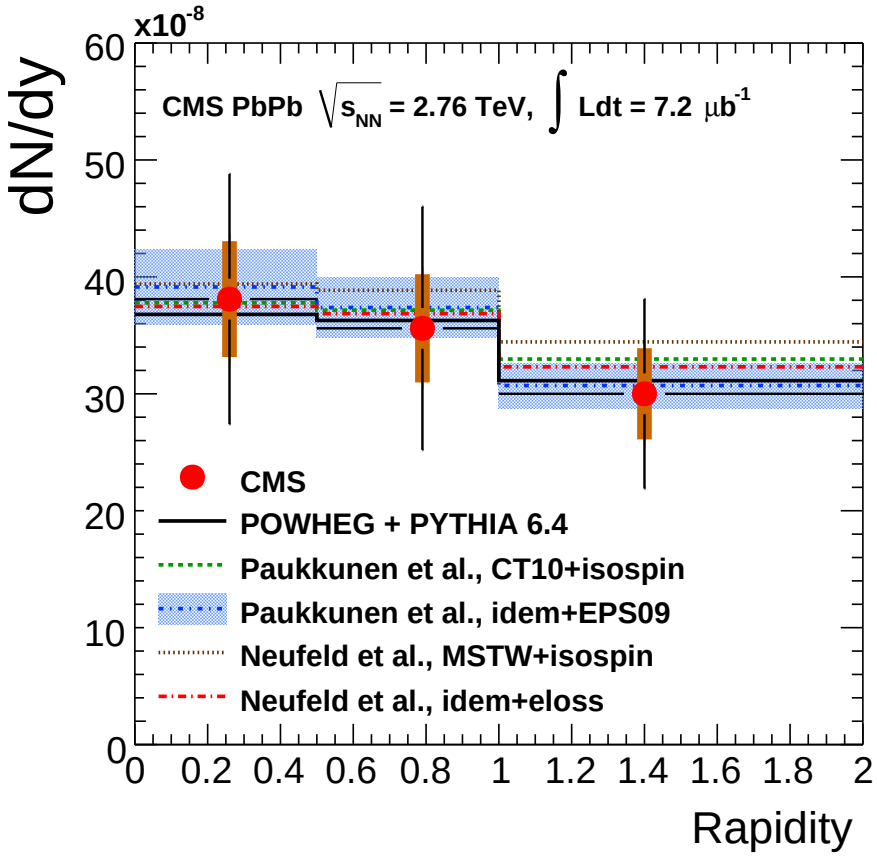

Figure 6.9: Rapidity distribution of Z^0 candidates in $PbPb$ collisions at $\sqrt{s_{NN}} = 2.76$ TeV

6.3.2 Z^0 transverse momentum

The differential yield as a function of Z^0 transverse momentum is

$$\frac{d^2N}{dydp_T} = \frac{N_Z}{\alpha\epsilon N_{\mathrm{MB}}} \cdot \frac{1}{\Delta y \Delta p_T} \tag{6.6}$$

The HI data are shown in Fig. 6.10. The data are shown by the red dots with systematic uncertainties in orange and statistical uncertainties in black. The HI data points are placed at the mean p_T values within the corresponding bin. The data are compared to calculation of POWHEG-interfaced-with-PYTHIA . Within statistical uncertainties, the POWHEG calculation scaled by the nuclear geometry agrees with the HI data.

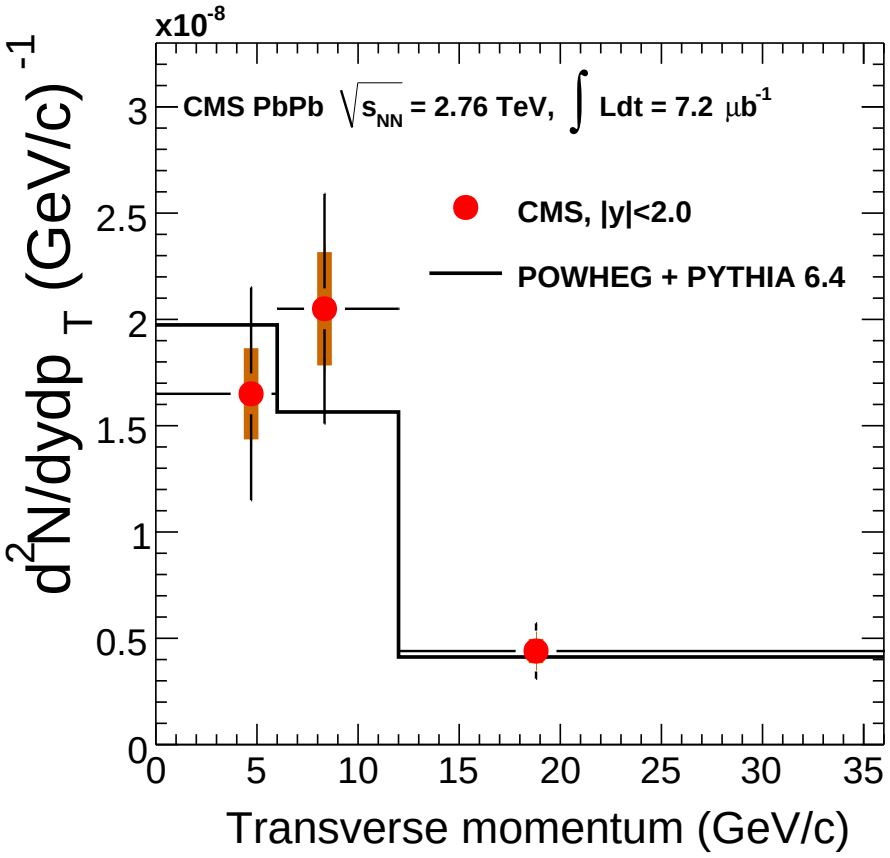

Figure 6.10: Transverse momentum distribution of Z^0 candidates in $PbPb$ collisions at $\sqrt{s_{NN}}$ = 2.76 TeV

6.3.3 High-p_T Z^0 event

In Fig. 6.10 one high-p_T (115.75 GeV/c) event is out of range. From Table .9, we see that the corresponding mass is 115.86 GeV/c^2 and the rapidity is 0.41. Due to the nature of the event, a careful examination of the event was carried out. No jet was found opposite to the Z^0 candidate in azimuth.

6.3.4 Z^0 yield vs $N_{\rm part}$ distribution

The differential yield divided by the overlap function is shown in Fig. 6.11 in three centrality bins. The HI data are compared to the same model calculations described in Sec. 6.3.1. The corresponding T_{AA} values are shown in table 6.6 [63]. The HI data are

shown by the red dots with systematic uncertainties in orange and statistical uncertainties in black. One minimum-bias point is also shown by the open blue square. The points are placed at the average N_{part} value of the centrality bin. A slight, ~3% [50] energy loss effect, from peripheral to central collisions is expected. Within experimental uncertainties, the data is compatible with all the models scaled by the nuclear geometry (A^2/σ_{PbPb}).

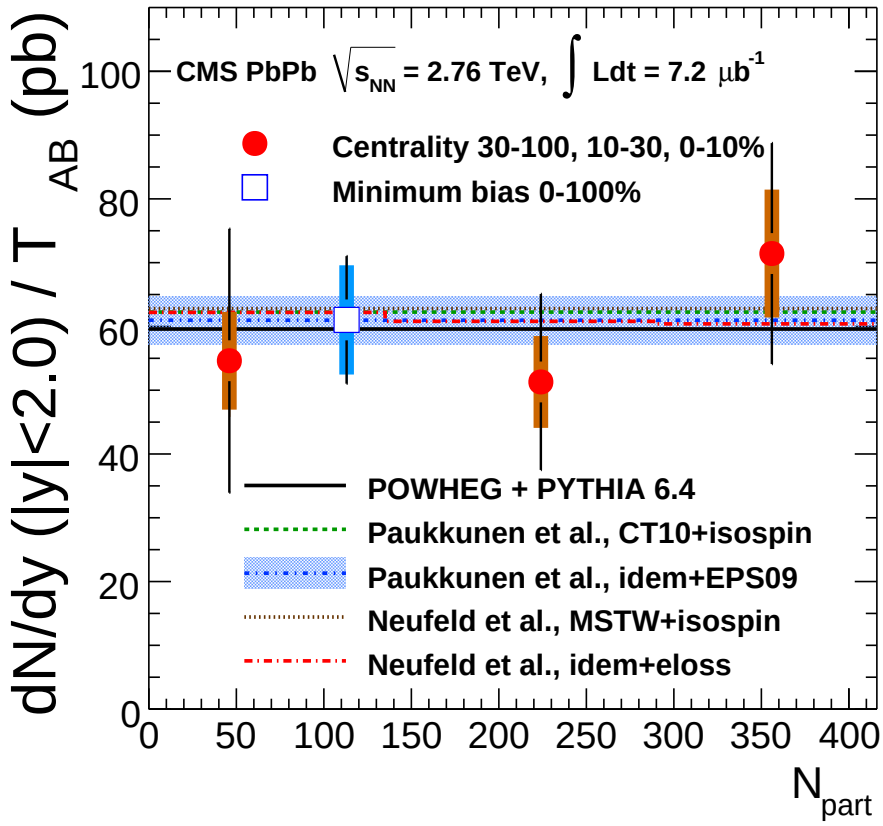

Figure 6.11: Number of participants distribution of Z^0 candidates in $PbPb$ collisions at $\sqrt{s_{NN}}$ = 2.76 TeV

The differential yields as a function of rapidity and p_T are summarized in Table 6.7. The results are divided into p_T, rapidity and centrality bins.

Table 6.6: Nuclear overlap function.

centrality	0-100 %	0-10 %	10-30%	30-100%
T_{AA} $(1/\mu\text{b}^{-1})$	5.67± 0.30	23.2± 1.9	11.6± 0.6	1.45± 0.13

Table 6.7: Number of Z^0 candidates (N_Z) in each $|y|$, p_{T} and centrality interval (second column) The associated yields are shown in the third column. The last column gives the pp differential cross section using POWHEG. Quoted uncertainties are statistical then systematic.

$\lvert y\rvert$	N_Z	dN/dy $(\times 10^{-8})$	$d\sigma_{pp}/dy$ (pb)
$[0, 2.0]$	39	$33.8 \pm 5.5 \pm 4.4$	59.6
$[0, 0.5]$	13	$38.1 \pm 10.7 \pm 5.0$	65.1
$[0.5, 1.0]$	12	$35.6 \pm 10.4 \pm 4.6$	64.0
$[1.0, 2.0]$	14	$30.0 \pm 8.1 \pm 3.9$	55.0
p_{T} (GeV/c)	N_Z	$d^2N/dydp_{\mathrm{T}}$ $(\times 10^{-8})$ [1/(GeV/c)]	$d\sigma^2_{pp}/dydp_{\mathrm{T}}$ [pb/(GeV/c)]
$[0, 6]$	11	$1.65 \pm 0.50 \pm 0.22$	3.48
$[6, 12]$	15	$2.05 \pm 0.54 \pm 0.27$	2.76
$[12, 36]$	12	$0.44 \pm 0.13 \pm 0.06$	0.73
Centrality	N_Z	dN/dy $(\times 10^{-8})$	$d\sigma_{pp}/dy$ (pb)
$[30, 100]\%$	7	$7.92 \pm 3.00 \pm 1.03$	59.6
$[10, 30]\%$	14	$59.5 \pm 16.0 \pm 7.7$	59.6
$[0, 10]\%$	18	$165 \pm 40 \pm 22$	59.6

6.3.5 Z^0 R_{AA} with POWHEG

The nuclear modification factor, R_{AA}, was first calculated employing POWHEG in the same kinematic range as the HI data. The differential cross section obtained from POWHEG in the range $|y| \leq 2.0$ is $d\sigma_{pp}/dy = 59.6$ pb. The nuclear modification factor is

$$R_{AA} = \frac{dN_{AA}/dy}{T_{AA} \times d\sigma_{pp}/dy} \tag{6.7}$$

The minimum-bias R_{AA} is 1.00± 0.16(stat.) ± 0.14(sys.) in the $|y| \leq 2.0$ range.

6.4 The *pp* reference sample

During March 2011, a *pp* run at $\sqrt{s}$= 2.76 TeV was taken for use as a reference sample for *PbPb* measurements at the same energy. The total integrated luminosity collected during this run by CMS was 231 nb^{-1} with an associated uncertainty of 6% based on the analysis of data collected during a Van der Meer scan [82]. A total of 29 Z^0 candidate events were found. A complete list of the Z^0 candidates can be found in the appendix (Table .10). The Level-1 triggers required slightly higher quality muons to cope with the higher *pp* collision rate. A comparison of the trigger efficiency in MC and data using the `tag-and-probe` method, results in a 2% systematic uncertainty [82]. The same offline event selection described in Sec. 5.2.3 was applied with the exception of a more relaxed HF coincidence requirement of one 3 GeV tower as opposed to three towers required in the *PbPb* case.

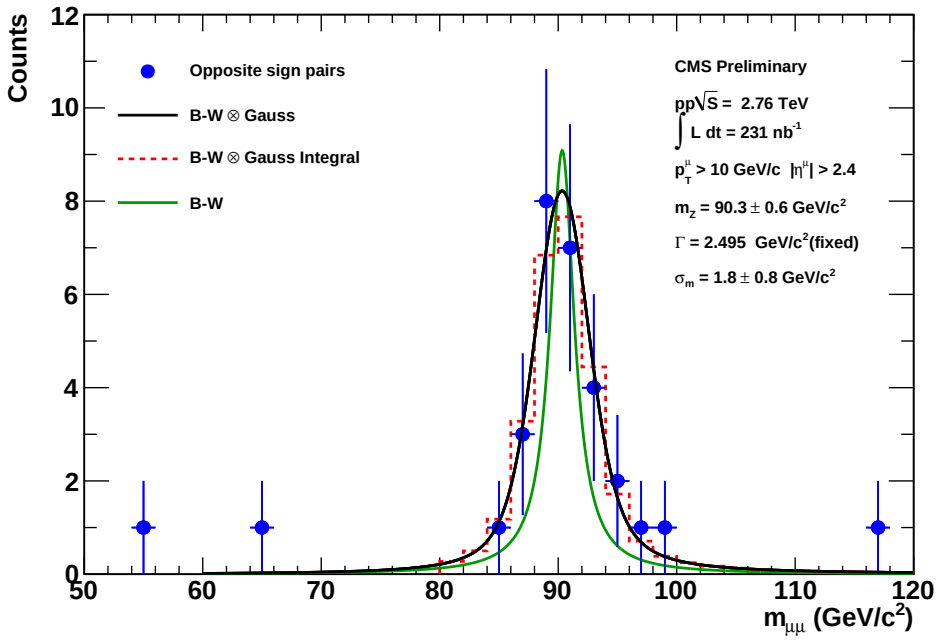

Figure 6.12: Z^0 candidates as a function of invariant mass in *pp* collisions at $\sqrt{s}$ = 2.76 TeV. The fit parameters are listed for the BW convolved with a Gaussian.

The *pp* data set was processed with the heavy-ion reconstruction software, in-

stead of the reconstruction software commonly used in *pp* collisions. The same `Acceptance` × `Efficiency` corrections used in *PbPb* collisions were considered, except that the most peripheral centrality bin is used for *pp* .

Figure 6.12 shows the invariant mass reconstructed from the *pp* run at $\sqrt{s} = 2.76$ TeV. The data points (blue dots) are shown with statistical error bars. Fits to the data are also overlaid, as described in Sec. 6.1.1. A Breit-Weigner fit (green line), with fixed width, to $\Gamma_Z = 2.495$ GeV/c^2, does not properly reproduce the mass resolution obtained from the HI reconstruction. A better approach is to use the BW convoluted with a Gaussian to account for the detector resolutions. There is no background in the range $50 \leq M_Z \leq 120$ GeV/c^2. A total of 29 candidates are found in the mass range $60 \leq M_Z \leq 120$ GeV/c^2.

6.4.1 Z^0 R_{AA} with *pp* data at $\sqrt{s_{NN}} = 2.76$ TeV

To calculate the nuclear modification factor from the data obtained in *pp* and *PbPb* it is necessary to obtain the *PbPb* yields,

$$\frac{1}{T_{AA}} \cdot \frac{d^2N}{dp_T dy} = \frac{1}{T_{AA}} \cdot \frac{1}{\Delta y \Delta p_T} \cdot \frac{N_Z}{\alpha \epsilon N_{\mathrm{MB}}} \tag{6.8}$$

While in the *pp* yield,

$$\frac{d^2\sigma}{dp_T dy} = \frac{1}{\mathcal{L}_{pp}} \cdot \frac{1}{\Delta y \Delta p_T} \cdot \frac{N_Z}{\alpha \epsilon} \tag{6.9}$$

Thus R_{AA} is:

$$R_{AA} = \frac{\mathcal{L}_{pp}}{T_{AA} N_{\mathrm{MB}}} \cdot \frac{N^Z_{PbPb}}{N^Z_{pp}} \cdot \frac{\alpha \epsilon_{pp}}{\alpha \epsilon_{PbPb}} \tag{6.10}$$

To calculate the nuclear modification factor, comparing the yield in *PbPb* with *pp*, Some of the systematic uncertainties cancel out due to the use of the same reconstruction algorithm. The ones that do not cancel are the following:

- The luminosity uncertainty in *pp* collisions, resulting in a global luminosity uncertainty of ± 6%
- Minbias event counting in *PbPb* collisions gives a global uncertainty of ± 3%

- The uncertainty in the *PbPb* background under the Z^0 peak, is a one-sided -3%. The uncertainty in the *pp* case is negligible due to the minimal background.
- Isospin, shadowing and energy loss, a ± 3.2%
- The systematic uncertainty due to dimuon trigger efficiencies of ± 2% uncertainty is assigned for dimuons [82].
- The inner tracking uncertainty is ±1%. Given that the same reconstruction algorithm was used, only the centrality dependent uncertainty is not canceled.

The total global systematic uncertainty is 6.7%. The overall systematic uncertainty on the measurement is calculated to be $^{+3.9\%}_{-4.9\%}$. The statistical uncertainty is found by adding the uncertainties in *pp* (±19%) and *PbPb* (±16%) in quadrature. The overall statistical uncertainty is ± 25%.

6.4.2 Results

The nuclear modification factor for $Z^0 \rightarrow \mu^+\mu^-$ ($|y| \leq 2.0$) at $\sqrt{s} = 2.76$ TeV is shown in Fig. 6.13. The points are shown with the statistical uncertainty in black bars. The systematic uncertainties are shown by red thick bars for the centrality bins, and blue thick bars for the minimum-bias point. The global systematic uncertainty is show as a green band around $R_{AA} = 1$. The value of R_{AA} does not have a dependence as a function of $N_{\rm part}$, within uncertainties. In each of the centrality bins, the measurement is compatible with unity within measurement uncertainties. The data points are placed at the average $N_{\rm part}$ value within the assigned centrality bin. The minimum-bias value shows no modification of the $Z^0 \rightarrow \mu^+\mu^-$ decay due to the nuclear medium, as expected. Given that there is no observed modification as a function of centrality, the $Z^0 \rightarrow \mu^+\mu^-$ channel can be established as a standard candle for hot nuclear effects.

Figure 6.14 shows R_{AA} as a function of the transverse mass, m_T, for the 10% most central collisions. Table 6.8 shows the R_{AA} values in the different centrality classes, as well as the overall value with statistical and systematic uncertainties. The plot shows the nuclear modification factor for isolated photons in CMS as black dots with statistical

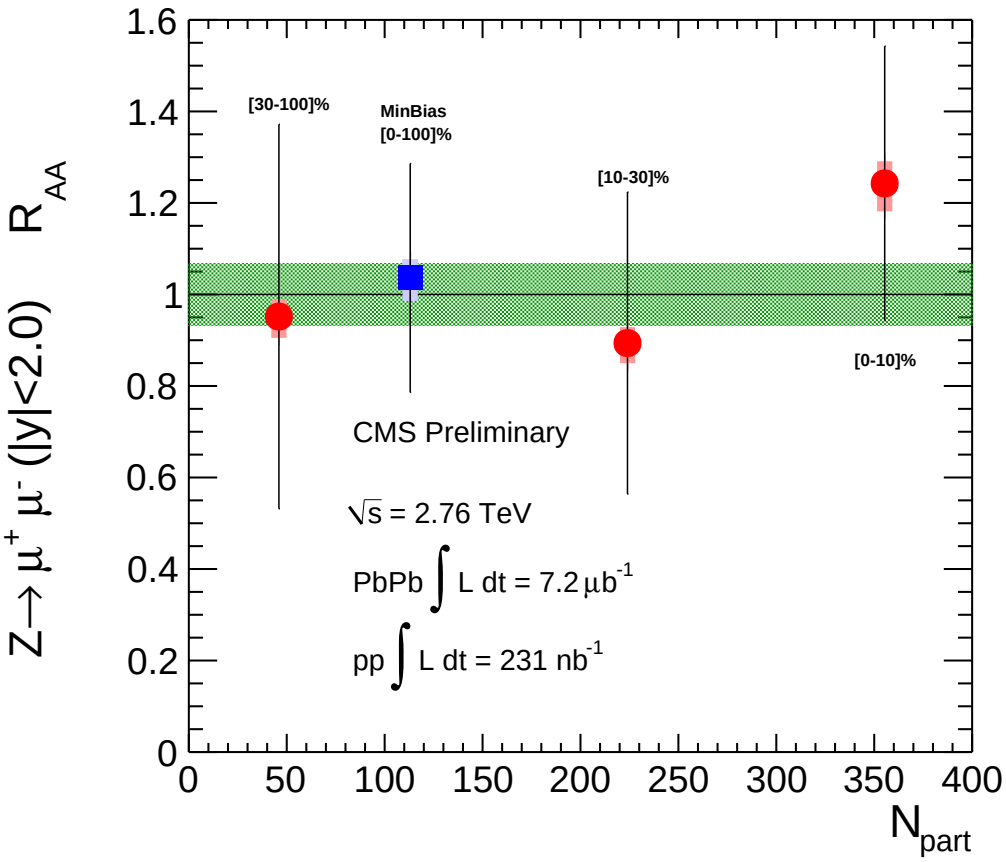

Figure 6.13: The nuclear modification factor as a function of N_{part} for $Z^0 \rightarrow \mu^+\mu^-$ at $\sqrt{s_{NN}}$ = 2.76 TeV

uncertainties and yellow bands as systematic uncertainties. The R_{AA} for the $Z^0 \rightarrow \mu^+\mu^-$ channel (blue square) with red systematic uncertainty bands is also shown. The R_{AA} for charged particles is also shown (hollow points) over a large range of m_T, with systematics uncertainties in blue. A clear charged particle suppression is observed in $PbPb$ collisions, while the electroweak probes remain unmodified, within measurement uncertainties, in the most central collisions.

6.5 Discussion

The first measurement by CMS of the Z^0 boson in heavy-ion collisions is presented. The Z^0 boson differential yields as a function of y, $p_T$and N_{part} were calculated in $PbPb$

Table 6.8: Nuclear modification factor.

centrality	0-100 %	0-10 %	10-30%	30-100%
R_{AA}	1.03	1.24	0.89	0.95
Statistical Uncertainty	25%	30%	33 %	42%
Systematical Uncertainty	[+4.0 ; -5.0]%	[4.8 ; -6.0]%	[+3.5 ; -4.4]%	[+3.7 ; -4.7]%

collisions. The nuclear modification factor was obtained using the *pp* reference run at $\sqrt{s_{NN}}$ = 2.76 TeV. The yields with respect to rapidity and p_T^Z were found match the POWHEG *pp* calculations, scaled by the nuclear geometry. In other words, the high-precision tune developed for *pp* collisions is able to reproduce the yields in *PbPb* collisions after scaling with the appropriate nuclear geometry, A^2/σ_{pp}. The yield as a function of N_{part} shows no dependence on the number of participants. Thus the $Z^0 \to \mu^+\mu^-$ yields measured per binary collision remain constant from peripheral to central collisions. The observed yields were compared to models that take into account subtler nuclear effects, e.g. modifications due to shadowing (10-20%) [49], isospin ($\sim$ 3%) [48] and energy loss ($\sim$ 2%) [50]. The statistical uncertainties are larger than the expected size of these modifications. Thus no further conclusions regarding their magnitude are possible.

The nuclear modification factor, R_{AA}, was also calculated using the *pp* reference run at the same energy of the *PbPb* run. Its value was found consistent with unity in three different centrality classes, demonstrating that there is no modification of the $Z^0 \to \mu^+\mu^-$ decay due to hot nuclear effects.

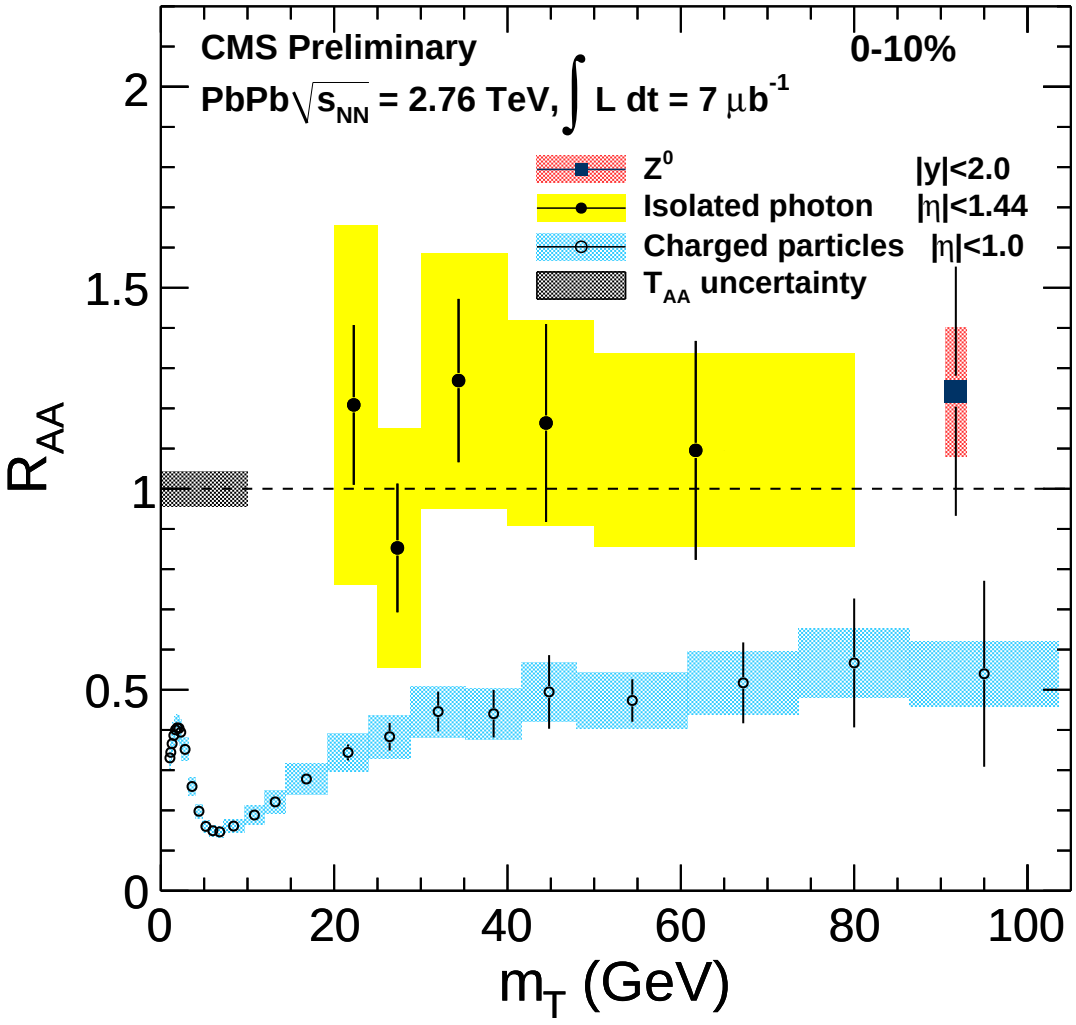

Figure 6.14: Nuclear modification factor of electromagnetic probe as a function of m_T in 0-10% most central events in CMS

Bibliography

[1] The science of matter, space and time, http://www.fnal.gov, 2004.

[2] Particle Data Group, K. N. et. al, J. Phys. G **37** (2010).

[3] D. d'Enterria and the CMS Collaboration, Journal of Physics G: Nuclear and Particle Physics **35**, 104039 (2008).

[4] Manuel Calderòn de la Barca Sànchez, *Charged Hadron Spectra in Au+Au collisions at* $\sqrt{s_{NN}}$ *= 130 GeV*, PhD thesis, Yale, 2001.

[5] CMS Collaboration, CMS collaboration, Phys. Rev. Lett. **106**, 212301 (2011).

[6] Gargamelle: neutral current event, 1973.

[7] G. Arnison *et al.*, Physics Letters B **126**, 398 (1983).

[8] UA2 Collaboration, P. Bagnaia *et al.*, Phys.Lett. **B129**, 130 (1983).

[9] P. G. Langacker, (2000).

[10] J. Bagger, Physics Reports **427**, 257 (2006).

[11] M. Gell-Mann, Physics Letters **8**, 214 (1964).

[12] D. J. Gross and F. Wilczek, Phys. Rev. Lett. **30**, 1343 (1973).

[13] C.-Y. Wong, *Introduction to High-Energy Heavy-Ion Collisions* (World Scientific Pub Co Inc, 1994).

[14] Physics Letters B **86**, 243 (1979).

[15] CDF Collaboration, F. Abe, H. Akimoto and Akopian, Phys. Rev. Lett. **74**, 2626 (1995).

[16] D0 Collaboration, S. Abachi *et al.*, Phys. Rev. Lett. **74**, 2422 (1995).

[17] I. M. Dremin and A. V. Leonidov, Physics-Uspekhi **53**, 1123 (2010).

[18] D. d'Enterria, J.PHYS.G **34**, S53 (2007).

[19] E. V. Shuriak, Zhurnal Eksperimental noi i Teoreticheskoi Fiziki **74**, 408 (1978).

[20] D. Schwarz, Annalen der Physik **12**, 220 (2003).

[21] E. Iancu and R. Venugopalan, hep-ph/0303204.

[22] J. M. Maldacena, Adv. Theor. Math. Phys. **2**, 231 (1998), [hep-th/9711200].

[23] K. Kovtun, P. D. T. Son and A. O. Starinets, Phys. Rev. Lett. **94**, 111601 (2005).

[24] H. Liu, K. Rajagopal and U. A. Wiedemann, Phys. Rev. Lett. **97**, 182301 (2006).

[25] S. S. Gubser, Phys. Rev. D **74**, 126005 (2006).

[26] M. G. Alford, K. Rajagopal and F. Wilczek, Phys. Lett. **B422**, 247 (1998), [hep-ph/9711395].

[27] Z. Fodor and S. D. Katz, 0908.3341.

[28] J. D. Bjorken, Phys. Rev. D **27**, 140 (1983).

[29] T. Altherr and P. Ruuskanen, Nuclear Physics B **380**, 377 (1992).

[30] R. Averbeck, Journal of Physics G: Nuclear and Particle Physics **30**, S943 (2004).

[31] J. Seixas *et al.*, Journal of Physics G: Nuclear and Particle Physics **34**, S1023 (2007).

[32] S. Campbell and the PHENIX Collaboration, Journal of Physics G: Nuclear and Particle Physics **34**, S1055 (2007).

[33] T. Matsui and H. Satz, Physics Letters B **178**, 416 (1986).

[34] A. Mócsy and P. Petreczky, Phys. Rev. Lett. **99**, 211602 (2007).

[35] R. Vogt, Phys. Rev. C **81**, 044903 (2010).

[36] X. Zhao and R. Rapp, Nuclear Physics A **859**, 114 (2011).

[37] X. Zhao and R. Rapp, Phys. Rev. C **82**, 064905 (2010).

[38] A. Andronic, P. Braun-Munzinger, K. Redlich and J. Stachel, Nuclear Physics A **789**, 334 (2007).

[39] L. Yan, P. Zhuang and N. Xu, Phys. Rev. Lett. **97**, 232301 (2006).

[40] S. C. J. Adams, NUCL.PHYS.A **757**, 102 (2005).

[41] R. Vogt, *Ultrarelativistic heavy-ion collisions* (Elsevier, 2007).

[42] E. Iancu and R. Venugopalan, hep-ph/0303204.

[43] J.-Y. Ollitrault, Phys. Rev. D **46**, 229 (1992).

[44] D. d'Enterria *et al.*, *CMS Physics: Technical Design Report v.2: Addendum on High Density QCD with Heavy Ions*, Technical Design Report CMS Vol. 34 (CERN, Geneva, 2007), revised version submitted on 2007-03-15 12:08:08.

[45] PHENIX Collaboration, S. S. Adler *et al.*, Phys. Rev. C **69**, 034909 (2004).

[46] PHENIX Collaboration, S. S. Adler *et al.*, Phys. Rev. Lett. **94**, 232301 (2005).

[47] R. Neufeld, I. Vitev and B.-W. Zhang, 1010.3708.

[48] H. Paukkunen and C. Salgado, Journal of High Energy Physics **2011**, 1 (2011), 10.1007/JHEP03(2011)071.

[49] R. Vogt, Phys. Rev. C **64**, 044901 (2001).

[50] R. B. Neufeld, I. Vitev and B.-W. Zhang, Phys. Rev. C **83**, 034902 (2011).

[51] L. Evans and P. Bryant, Journal of Instrumentation **3**, S08001 (2008).

[52] L. Evans and P. Bryant, Journal of Instrumentation **3**, S08001 (2008).

[53] D. Acosta, editor, *CMS Physics Technical Design Report Volume I: Detector Performance and Software*Technical Design Report CMS (CERN, Geneva, 2006).

[54] R. Brauer and K. Klein, CERN Report No. CMS-NOTE-2005-025. CERN-CMS-NOTE-2005-025, 2005 (unpublished).

[55] CMS collaboration, *The CMS muon project: Technical Design Report*Technical Design Report CMS (CERN, Geneva, 1997).

[56] J. Hauser, Nuc. Instrum. Meth. A: Accelerators, Spectrometers, Detectors and Associated Equipment **384**, 207 (1996), BEAUTY '96.

[57] R. Santonico and R. Cardarelli, Nuclear Instruments and Methods in Physics Research **187**, 377 (1981).

[58] Y.-J. L. L. Bagby, A. J Bell and G. Veres, CERN Report No. 018, 2010 (unpublished).

[59] I. Lokhtin and A. Snigirev, The European Physical Journal C - Particles and Fields **45**, 211 (2006), 10.1140/epjc/s2005-02426-3.

[60] M. Hildreth, Instructions for using the datamixingmodule, https://twiki.cern.ch/twiki/bin/view/CMS/DataMixer, 2011.

[61] G. Cerati, Track reconstruction sequences, https://twiki.cern.ch, 2011.

[62] CMS collaboration, CMS Internal Note (2007).

[63] CMS collaboration, Internal Note (2010).

[64] R. Wilkinson and P. T. Cox, CERN Report No. CMS-NOTE-2001-013, 2001 (unpublished).

[65] G. Bruno *et al.*, CERN Report No. CMS-NOTE-2002-043, 2002 (unpublished).

[66] R. Brun, Root reference guide, http://root.cern.ch/root/html/TMath.html#TMath:Prob, 2011.

[67] CMS collaboration, CMS Analysis Note 2009/111 (2009).

[68] CMS collaboration, *CMS TriDAS project: Technical Design Report; 1, the trigger systems*Technical Design Report CMS (Technical Design Report CMS ; 6, 2000).

[69] CMS collaboration, CMS Analysis Note 2010/399 (2010).

[70] M. R. P. Billoir, R. Frhwirth, Nucl. Instr. and Meth **A241**, 115 (1985).

[71] C. Campagnari and D. Kovalsky, Software guide tracker muons, https://twiki.cern.ch/twiki/bin/view/CMSPublic/SWGuideTrackerMuons, 2011.

[72] G. Abbiendi, N. Adam, J. Alcaraz et al., CMS Analysis Note 2008/097. (2008).

[73] M. Mulders, I. Bloch, E. James et al., CMS Analysis Note 2008/098 (2008).

[74] T. VBTF, CMS Analysis Note 2010/116 (2010).

[75] T. Sjöstrand, S. Mrenna and P. Skands, JHEP **026** (2006), [hep-ph/0603175].

[76] J. Pumplin *et al.*, JHEP **07**, 012 (2002), [hep-ph/0201195].

[77] CMS collaboration, Journal of High Energy Physics **2011**, 1 (2011), 10.1007/JHEP01(2011)080.

[78] G. Breit and E. Wigner, Phys. Rev. **49**, 519 (1936).

[79] CMS collaboration, Internal Note (2011).

[80] S. Frixione and B. R. Webber, Journal of High Energy Physics **2002**, 029 (2002).

[81] K. Eskola, H. Paukkunen and C. Salgado, Journal of High Energy Physics **2009**, 065 (2009).

[82] CMS collaboration, Internal Note (2011).

Appendices

Table .9: List of all Z candidates from $PbPb$ collsions at $\sqrt{s_{NN}} = 2.76$ TeV. Cent corresponds to the centrality bin, 0 is the most central

runN	LS	eventN	Z mass	Z p_T	Z y	cent	η^{μ_1}	η^{μ_2}	$p_T^{\mu_1}$	$p_T^{\mu_1}$	$\delta(\phi)$
150590	183	776435	93.07	14.61	-1.28	5	-2.28	-0.38	29.67	33.77	2.70
151020	212	998915	87.83	16.75	-1.08	6	-2.29	-0.31	21.46	38.17	3.18
151027	663	2714491	88.69	6.95	-0.24	12	-0.66	0.16	39.52	42.52	2.99
151058	230	1189276	91.77	1.47	-1.42	11	-1.93	-0.91	40.80	40.13	3.17
151058	437	2407858	89.27	7.47	-0.19	10	-0.60	0.20	39.87	42.97	2.98
151059	19	100429	82.47	11.99	-0.88	1	-0.77	-1.02	46.30	36.41	3.31
151088	57	350321	87.23	4.78	-1.59	3	-2.00	-1.22	38.43	42.64	3.20
151211	126	676548	88.23	5.09	1.69	11	1.96	1.45	40.82	44.74	3.07
151240	16	85452	91.76	6.08	1.03	0	1.58	0.43	41.33	37.38	3.26
151240	213	1123319	92.80	6.38	-0.26	17	0.35	-0.95	41.21	35.29	3.20
151353	127	715443	85.08	18.30	-0.78	0	-1.28	-0.24	39.83	36.56	2.67
151968	78	450797	90.05	13.82	0.12	10	0.84	-0.54	35.03	38.01	3.51
152112	170	804963	87.34	6.63	-0.14	6	0.61	-0.82	32.57	36.62	3.29
152112	527	2734474	94.77	7.74	1.68	0	1.64	1.72	46.05	48.96	2.99
152112	596	3092518	87.36	5.54	-0.62	3	-0.40	-0.83	40.50	45.03	3.07
152113	533	2789077	98.50	21.36	-1.43	7	-2.12	-0.29	46.26	25.05	3.07
152349	107	385577	90.44	27.95	0.64	3	1.10	-0.18	52.02	27.32	2.79
152431	353	1883516	89.01	7.94	-1.48	0	-1.44	-1.52	47.25	42.04	3.01
152474	127	608700	89.07	11.00	-0.87	1	-0.78	-0.98	46.49	42.82	2.91
152561	355	1965024	91.98	5.24	1.13	0	2.28	-0.02	26.55	26.60	3.34
152592	131	788491	90.85	4.12	-0.75	0	-1.84	0.34	27.42	27.61	3.29
152592	308	1820803	99.71	5.78	1.01	0	1.08	0.93	50.52	49.08	3.03
152601	122	528278	115.86	115.75	0.41	1	1.10	0.13	41.84	107.27	1.55
152602	92	568075	91.59	11.01	0.87	7	1.26	0.56	38.11	48.83	3.08
152602	328	1969397	76.82	23.70	-0.26	5	-0.44	-0.00	45.59	32.93	2.62
152602	647	3744192	93.69	13.33	0.78	2	1.47	0.27	33.64	46.49	3.05
152625	273	1587545	93.54	8.91	-0.09	6	-1.04	0.68	29.48	38.24	3.09
152625	530	2989029	91.45	10.39	0.48	14	1.45	-0.79	32.69	22.30	3.14
152641	173	1020942	91.33	2.71	1.36	3	2.11	0.60	35.71	34.65	3.21
152642	477	2861862	90.02	6.21	0.35	15	1.27	-0.71	32.27	26.81	3.04
152652	90	347872	82.39	12.53	-1.40	9	-1.67	-1.07	43.66	36.05	2.89
152705	55	211752	76.46	14.78	0.25	1	2.11	-0.87	10.85	24.97	2.88
152722	115	722609	84.19	7.59	-0.74	16	-1.12	-0.42	36.09	43.47	3.10
152745	628	3636927	92.22	5.99	-0.86	1	-2.22	0.35	21.87	25.78	3.33
152751	230	1213764	91.23	5.30	1.82	16	2.11	1.52	45.40	42.10	3.05
152785	282	1586972	91.05	8.82	-0.28	2	0.01	-0.60	45.29	42.07	2.95
152785	265	1485142	93.76	17.85	-0.96	7	-1.31	-0.72	36.85	54.66	3.17
152957	134	829320	91.57	5.81	-0.36	12	-0.11	-0.62	45.22	43.66	3.02
152957	575	3532156	90.55	31.18	-0.71	4	-1.59	0.86	38.20	16.66	2.22

Table .10: List of all Z candidates in pp collisions at $\sqrt{s} = 2.76$ TeV

runN	LS	eventN	Z mass	Z p_T	Z y	η^{μ_1}	η^{μ_2}	$p_T^{\mu_1}$	$p_T^{\mu_1}$	$\delta(\phi)$
891	17639301	161366	89.62	5.11	0.23	1.24	-0.91	29.34	25.32	3.02
1175	108516259	161439	89.88	6.94	0.11	0.76	-0.66	39.08	32.36	3.09
1490	112886783	161439	99.74	13.43	1.28	1.94	0.40	45.26	31.91	3.18
4363	1472661	161454	89.79	2.20	1.97	2.21	1.713	44.46	42.55	3.11
4653	2054342	161473	91.37	10.54	0.96	0.50	1.48	43.75	38.16	2.92
5030	4937589	161473	89.49	6.16	-0.19	0.69	-1.17	32.37	28.72	2.97
5137	5758592	161473	84.69	7.66	-0.62	0.16	-1.56	33.98	27.08	3.03
5753	10561994	161473	65.01	20.20	0.26	-0.49	1.43	29.47	16.82	2.41
8536	20253173	161474	91.30	4.10	-1.26	-0.36	-2.19	32.32	30.73	3.02
9870	5142488	161396	86.68	7.89	-0.84	-0.69	-1.02	46.86	39.00	3.15
9930	5754687	161396	86.21	7.34	-1.60	-2.21	-0.91	38.00	33.13	2.98
11688	46355453	161474	117.07	6.89	-0.70	-1.33	0.01	50.90	44.11	3.16
12584	54920550	161474	88.42	46.33	0.34	0.05	1.06	66.03	24.41	2.62
12811	8617541	161366	88.96	1.91	0.53	-1.02	2.18	18.11	16.34	3.10
13422	1643178	161439	89.71	6.01	0.98	-0.06	2.11	28.55	25.78	2.94
14284	8882716	161439	92.02	17.60	-0.22	0.40	-1.11	43.83	28.70	2.88
15311	17168095	161439	91.12	16.48	-0.06	-1.02	1.07	32.29	25.59	2.61
15426	18235512	161439	91.09	4.51	-0.63	0.62	-2.02	24.56	20.76	3.03
17114	32323618	161439	95.43	2.62	-0.07	-1.70	1.57	17.89	17.86	2.99
17444	35437261	161439	87.93	6.37	-0.10	0.59	-0.88	36.73	31.83	3.26
18774	47271486	161439	97.46	73.67	0.74	0.57	1.25	88.50	28.55	4.02
19565	53826449	161439	91.11	29.88	-0.50	-0.71	-0.10	59.55	32.30	3.42
20815	66003581	161439	92.23	47.68	1.12	1.22	0.82	74.80	27.39	3.25
21120	68948418	161439	89.34	23.13	-0.05	-0.86	1.37	38.91	18.10	2.75
21202	69949862	161439	92.90	30.64	1.69	2.33	0.30	48.71	18.20	3.04
21878	76402031	161439	90.25	13.93	1.20	1.74	0.43	44.47	30.56	3.16
21928	77020280	161439	91.31	7.44	1.85	2.23	1.42	45.06	39.59	3.02
22153	79513631	161439	93.15	10.71	1.75	1.95	1.51	48.88	42.71	3.33
23620	94269250	161439	95.64	32.65	1.67	1.56	1.78	52.39	48.05	3.79